

Study of strongly interacting matter using dimuons produced in Pb+Pb collisions at $\sqrt{s_{NN}} = 2.76$ TeV

Vineet Kumar
of Nuclear Physics Division

A dissertation submitted to the HBNI
for the degree of Doctor of Philosophy



Figure 1.

Abstract

Quarkonia suppression, caused by the Debye screening of the Quantum Chromo Dynamic (QCD) potential between the two heavy quarks, was originally claimed to be an unambiguous signal of the formation of a Quark-Gluon Plasma (QGP) [1]. J/ψ suppression has been observed in heavy ion collisions at both SPS and RHIC, however, the magnitude of the suppression in both systems was similar despite the differing energy densities [47]. This indicates that Quarkonia suppression isn't as unambiguous a signal as previously supposed because there are many competing processes that affect the yield of quarkonia in heavy ion collisions. Some of these effects enhance the quarkonia yield, such as the statistical recombination of the $Q\bar{Q}$ pairs, while others reduce it, such as co-mover absorption [3]. These processes affect the Υ family less than the J/ψ family at 2.76 TeV, and it is believed that color screening should be the dominant process that contributes to any observed suppression of the Υ family.

Declaration

This dissertation is the result of my own work, except where explicit reference is made to the work of others, and has not been submitted for another qualification to this or any other university. This dissertation does not exceed the word limit for the respective Degree Committee.

Vineet Kumar

Acknowledgements

Of the many people who deserve thanks, some are particularly prominent, such as my supervisor

Preface

This thesis describes my research on various aspects of the CMS Heavy Ion physics program, centred around the CMS detector and LHC accelerator at CERN in Geneva.

Contents

1. Standard Model and Quark Gluon Plasma	2
1.1. Standard model and Quantum Chromodynamics	2
1.1.1. Standard model	2
1.1.2. Quantum Chromodynamics	5
1.1.3. High Temperature QCD Matter	7
2. Quarkonia production and properties in Hot and dense matter	13
2.1. Quarkonia	13
2.1.1. The discovery of quarkonia	13
2.1.2. Quarkonium production	14
2.1.3. Qualitative formation and decay times	16
2.1.4. Quarkonium binding potential	18
2.2. Experimental Status of Quarkonia Suppression	20
2.2.1. J/ψ anomalous suppression at SPS	20
2.2.2. J/ψ and $\Upsilon(nS)$ suppression at RHIC	21
3. The Compact Muon Solenoid Experiment at The CERN Large Hadron Collider	29
3.1. The LHC	29
3.1.1. The Accelerator Chain	31
3.2. Luminosity	32
3.3. Compact Muon Solenoid	33
3.3.1. Magnet	36
3.3.2. Tracker	36
3.3.3. Calorimetry	38
3.3.4. CMS Muon System	39
3.3.5. Trigger and Data Acquisition	41
3.3.6. CMS data flow	43

4. Υ production in Pb+Pb collisions	44
4.1. $\Upsilon(nS)$ in Pb+Pb collisions	44
4.2. Data Selection	45
4.2.1. Event Selection	45
4.2.2. Muon Selection	48
4.3. Signal Extraction	50
4.3.1. $\Upsilon(1S)$ Analysis	50
4.4. Acceptance and Efficiency	52
4.4.1. Acceptance	52
4.4.2. Efficiency	53
4.5. The pp Baseline Measurement	54
4.6. Results	57
4.6.1. $\Upsilon(1S)$	59
4.7. Indication of suppression of excited Υ states in PbPb collisions at $\sqrt{s_{\text{NN}}} = 2.76 \text{ TeV}$	62
4.8. Discussion	68
5. Detail study of Υ suppression in Pb+Pb collisions using $150 \mu\text{b}^{-1}$ data with CMS detector at LHC.	70
5.1. Introduction	70
5.2. Data Selection	71
5.2.1. Optimization procedure	72
5.2.2. Track and dimuon quality	73
5.2.3. Kinematic threshold	77
5.2.4. Summary of offline selection	81
6. Component of dimuon continuum	84
6.1. Introduction	84
6.2. Dilepton production by hard processes	85
6.3. Thermal dilepton production	91
6.4. Results and discussion	93
6.5. CONCLUSIONS	99
A. appendices	100
A.1. Extra Studies	100
A.2. rr	100

Bibliography	101
List of Figures	112
List of Tables	117

*“Writing in English is the most ingenious torture
ever devised for sins committed in previous lives.”*

— James Joyce

Chapter 1.

Standard Model and Quark Gluon Plasma

1.1. Standard model and Quantun Chromodynamics

1.1.1. Standard model

The Standard Model (SM) of particle physics is a theory of particle properties and particle interactions[4]. It describes the strong, weak, and electromagnetic forces between the fundamental particles of matter. Special relativity and quantum mechanics form the basis for quantum field theory and the Standard Model. The SM includes 12 elementary particles of spin $\frac{1}{2}$ known as fermions. The fermions of the SM are classified according to how they interact (or equivalently, by what charges they carry). There are six quarks (up, down, charm, strange, top, bottom), and six leptons (electron, electron neutrino, muon, muon neutrino, tau, tau neutrino) their properties are summarized in Table 1.1. The quarks and leptons are grouped in three generations. The first generation contains the most stable particles which make most of the observed matter in the universe, while the second and the third generations contain particles which decay to the lower generation of particles. The interactions among quarks and leptons occur via exchange of another type of particles named bosons, see Table 1.2. The quarks and leptons have spin-1/2 while bosons are spin-1 particles. There are four fundamental interactions: strong, weak, electromagnetic and gravitational. Each of the interactions has different strength and range of influence. Leptons participate in gravitational, electromagnetic and weak interactions. Quarks on the other hand can participate in all four interactions. A graphical repersentation of all standard model particles can be seen in Figure 1.1. The

theory which describes the strong interaction between quarks and gluons is Quantum Chromodynamics (QCD) and it will be described in the following sections

Table 1.1.: Quarks and leptons properties. Every particle in the table has a corresponding antiparticle with opposite charge. According to the Standard Model, the neutrino masses are equal to zero. Observed neutrino oscillation suggests that the neutrinos have mass and their experimental values are reported in the table

Generation	Name	Symbol	Electric charge	Mass[MeV/c ²]
I	Electron	e ⁻	-1	0.511
	Electron neutrino	ν_e	0	≤ 0.000225
II	Muon	μ^-	-1	105.658
	Muon neutrino	ν_μ	0	≤ 0.19
III	Tau	τ^-	-1	1776.82
	Tau neutrino	ν_τ	0	≤ 18.2
Quarks				
I	Up	u	$+\frac{2}{3}$	1.8–3.0
	Down	d	$-\frac{1}{3}$	4.5–5.5
II	Charm	c	$+\frac{2}{3}$	1250–1300
	Strange	s	$-\frac{1}{3}$	90–100
III	Top	t	$+\frac{2}{3}$	172100–174900
	Bottom	b	$-\frac{1}{3}$	4150–4210

Table 1.2.: Boson properties

Name	Force	Electric Charge	Mass [GeV/c ²]
Symbol	Range(m)	Color charge	Strength
Photon	Electromagnetic	0	0
γ	∞	0	$\alpha = \frac{1}{137}$
Gluon	Strong	0	0
g	10^{-15}	8 colored gluons	α_s , 1, at high energy $\alpha_s \rightarrow 0$
Z Boson	Weak	0	91.187
Z^0	10^{-18}	0	$\alpha_z = 10^{-6}$
W Boson	Weak	± 1	80.399
W^\pm	10^{-18}	0	$\alpha_W = 10^{-6}$

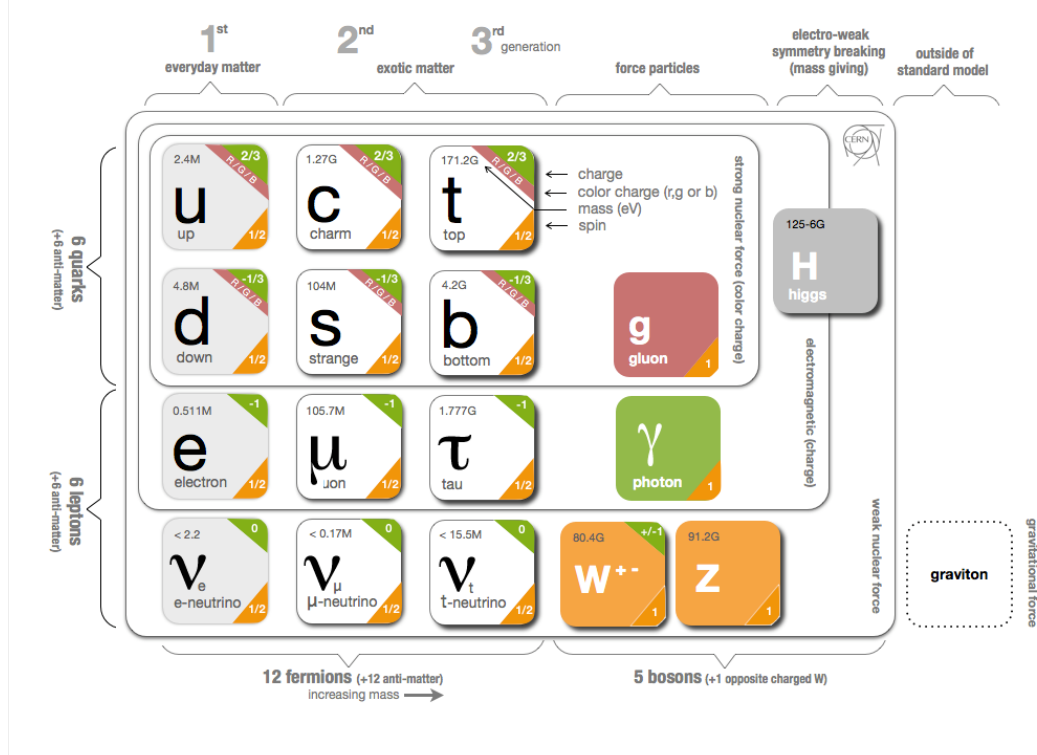


Figure 1.1.: Standard Model leptons and bosons.

1.1.2. Quantum Chromodynamics

Quantum chromodynamics (QCD) [5–8] is the field theory describing the strong interactions of colored quarks and gluons. Color charge comes in three versions (red, green and blue) that form a fundamental representation of the SU(3) group, and is carried by both the quarks and gluons. Analogous to electric charge in quantum electrodynamics (QED) [9, 10], color charge is conserved in QCD, but since the gluons carry color charge, they can interact with other gluons. This is not possible in QED, as photons do not carry electric charge. The existence of self-coupling in QCD has important implications for the scale dependence of the strong coupling. In quantum field theory, the coupling constant describing the interaction between two particles is an effective constant, which is dependent on the energy-scale Q^2 of the interaction. In QED this dependence is only a weak one; in QCD, however, it is very strong. The reason is the self-coupling of the gluons. The dependence of the strong coupling constant $\alpha_s(Q^2)$ on Q^2 is known as a running coupling constant. In perturbative QCD (pQCD), a first-order approximation yields:

$$\alpha_s(Q^2) = \frac{1}{\beta_0 \ln(\frac{Q^2}{\Lambda_{QCD}^2})}, \text{ where } \beta_0 = \frac{33 - n_f}{12\pi} \quad (1.1)$$

Here, n_f denotes the number of quark types with mass below Q^2 , and Λ_{QCD} represents the characteristic scale of confinement. Λ_{QCD} is determined by comparing predictions with experimental data and is found to be on the order of 250 MeV [11].

The Q^2 – dependence of the coupling strength corresponds to a dependence on quark separation. For very small distances and corresponding high values of Q^2 , the strong coupling decreases, vanishing asymptotically as $Q^2 \rightarrow \infty$ 1.2. In the limit $Q^2 \rightarrow \infty$, quarks can be considered to be “free”; this phenomenon is called asymptotic freedom. In contrast, at large distances, the strong coupling increases substantially so that it is not possible to detach individual quarks from hadrons. This phenomenon is called confinement. In this regime, perturbation theory breaks down. Quarks and gluons are not seen in experiments. Instead, they turn into hadrons, which are observed in the detectors. This process is called hadronization. Hadronization of quarks happens at a later time ($t \sim \frac{1}{\Lambda_{QCD}}$) than the production process ($t \sim \frac{1}{Q}$). This is why the calculations of hadronic cross sections can be factorized into perturbative and non-perturbative parts.

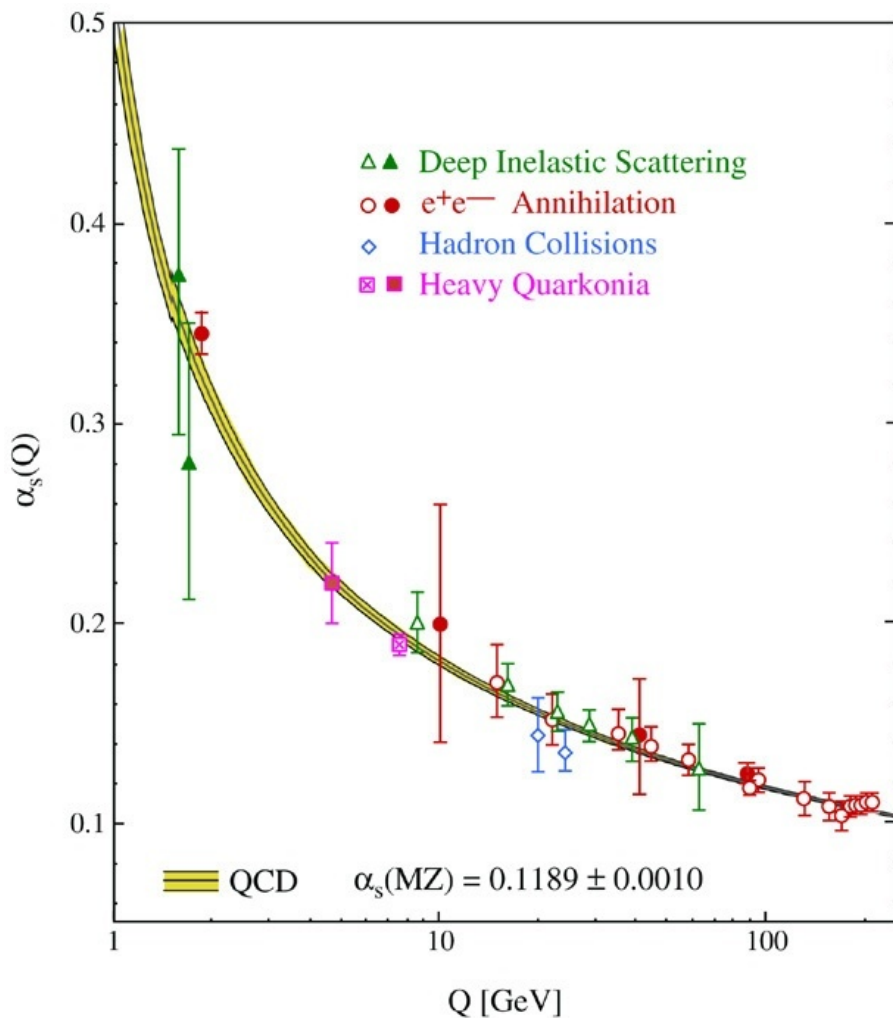


Figure 1.2.: Figure shows a compilation of the values for α_s , derived from many different experiments, and for different momenta Q of the exchanged gluons. Gluon momentum is measured in GeV/c , and a logarithmic scale has been used to allow to show a bigger range of values.

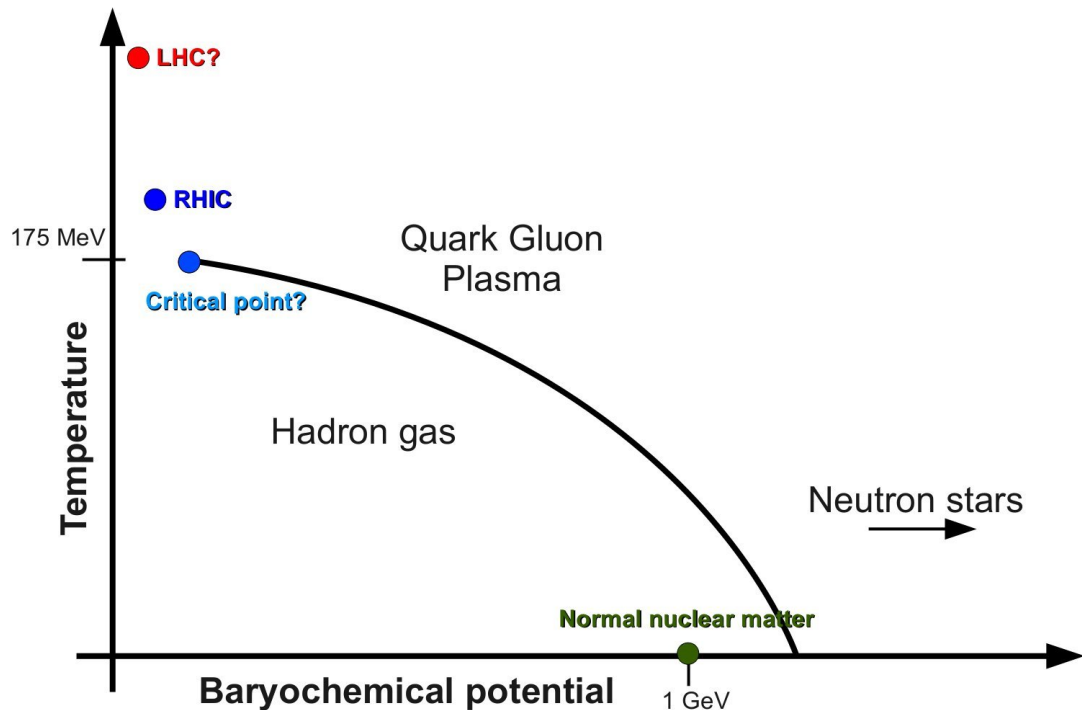


Figure 1.3.: QCD phase diagram

1.1.3. High Temperature QCD Matter

The behavior of QCD at high temperatures or densities has long been of interest. In the first few microseconds after the Big Bang, the universe would have had an enormous energy density, and hence a very high temperature. It is expected that at such temperatures the component quarks and gluons of normal hadronic matter have enough energy that they are no longer confined to their usual bound states. This results in a phase transition between normal matter and a new state, known as the Quark-Gluon Plasma (QGP) in analogy to electromagnetic plasmas in which the electrons and ions are freed of their atomic bound states. A corresponding phase diagram can be constructed, as shown in Figure 1.3, which includes normal nuclear and hadronic matter, as well as the QGP phase. In addition, other phases are expected to exist at higher net baryon chemical potential, such as in neutron stars.

Unfortunately, the QGP near the transition temperature is an inherently non-perturbative regime, and other methods must be used to perform calculations. One way around this difficulty is to perform numerical calculations using lattice QCD, which makes use of a Euclidean spacetime grid to calculate the path integral of the QCD partition

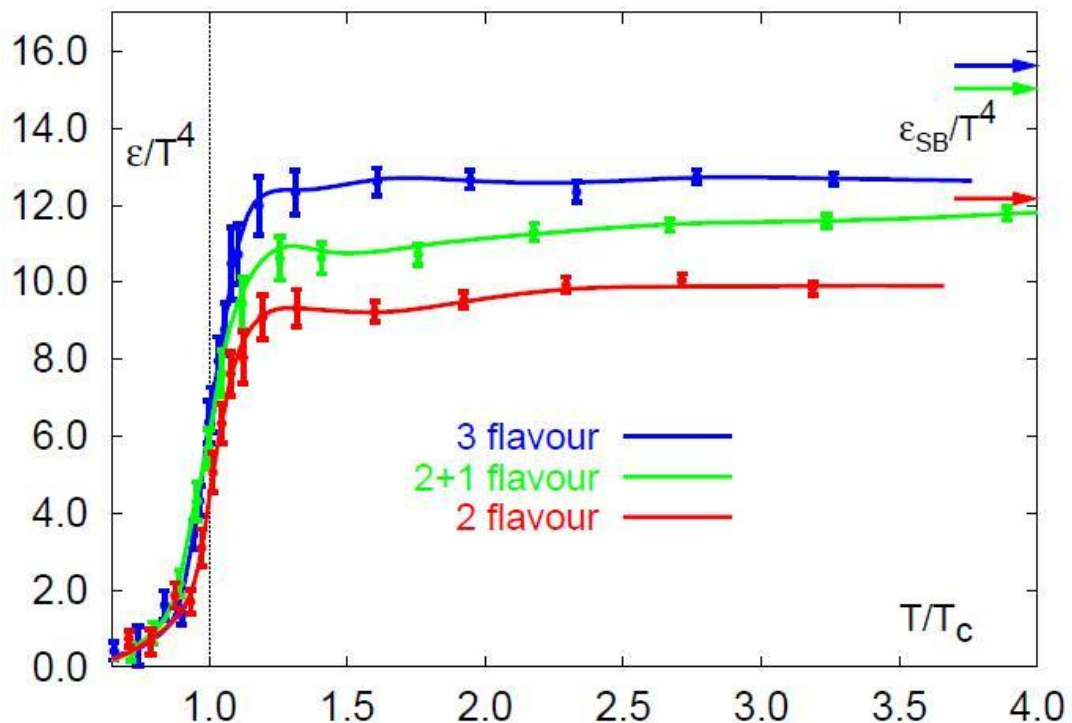


Figure 1.4.: Energy density in units of T^4 as calculated in lattice QCD as calculated in [15]. The sharp rise at $T \sim T_c$ corresponds to the phase transition to the QGP. On the right side the energy density of a simple Stefan-Boltzmann gas of partons (as calculated in the text) is labeled.

function. From there statistical and thermodynamic properties such as temperature and free energy can be calculated.

Recently lattice QCD has been used to examine the phase transition to a QGP. It was found that the transition temperature is $T_c \sim 170$ MeV. This happens to lie very close to the Hagedorn temperature $T_H \sim 160$ MeV, the limiting temperature in high-energy hadronic collisions, above which only the entropy of the thermodynamic system is increased (i.e. the number of hadronic states produced) [12].

In order to create such a state of matter in the laboratory, heavy nuclei are collided at relativistic velocities such that a portion of the large kinetic energy is converted to thermal energy. The temperature dependence of the energy density can be naively calculated by assuming the QGP is a Stefan-Boltzmann gas of massless, non-interacting particles [13, 14]. The partition function for fermions (−) and bosons (+) is:

$$\ln Z(T, \mu, V) = \frac{gV}{2\pi^2 T} \int_0^\infty \frac{dk k^4}{3E} \left[\frac{1}{e^{(E-\mu)/T} \pm 1} + \frac{1}{e^{(E+\mu)/T} \pm 1} \right] \quad (1.2)$$

If we assume that the number of quarks and anti-quarks are equal, then it can be shown that $\mu=0$. For gluons (or other bosons), this becomes

$$\begin{aligned} \ln Z &= g \frac{\pi^2}{90} V T^3 \text{ (boson)} \\ &= g \frac{7\pi^2}{720} V T^3 \text{ (fermions)} \end{aligned} \quad (1.3)$$

Now, since energy density is

$$\epsilon = \left(\frac{T^2}{V}\right) \left(\frac{\delta \ln Z}{\delta T}\right)$$

We can calculate

$$\epsilon = (g_b + \frac{7}{8}g_f)\frac{\pi^2}{30}T^4 \quad (1.4)$$

(1.5)

where $g_{b,f}$ are the degeneracy numbers of the bosons, fermions as calculated below for gluons and quarks+antiquarks:

$$\begin{aligned} g_b &= g_{gluon} = ((8 \text{ color states})(2 \text{ spin}) \\ g_f &= g_q + g_{\bar{q}} = 2(3 \text{ color})(2 \text{ spin})(n \text{ flavor}) \end{aligned} \quad (1.6)$$

This gives us

$$\begin{aligned} \epsilon &= 37\frac{\pi^2}{30}T^4(2 \text{ quark flavour}) \\ &= 47.5\frac{\pi^2}{30}T^4(3 \text{ quark flavour}) \end{aligned} \quad (1.7)$$

for the energy density of a gas of massless partons.

Using lattice QCD it is possible to perform a more realistic calculation of the energy density. Figure 1.4 shows such a calculation of the energy density [15]. At sufficient temperature, this result shows the same T^4 -scaling of the plasma energy density as calculated above. It should be noted that the calculation plateaus at $\sim 80\%$ of the Stefan-Boltzmann gas of non-interacting partons. This has sometimes been taken as evidence that the plasma weakly-interacting, but other calculations have shown that even a strongly-interacting plasma could approach this limit [16].

As the medium expands and cools, it passes through several phases, as shown in Figure 1.5. First hadronization will occur once the temperature becomes low enough that partons are confined again. Next, kinetic freeze-out occurs when the expanding hadrons are too sparse to interact with one another. At this point they will continue

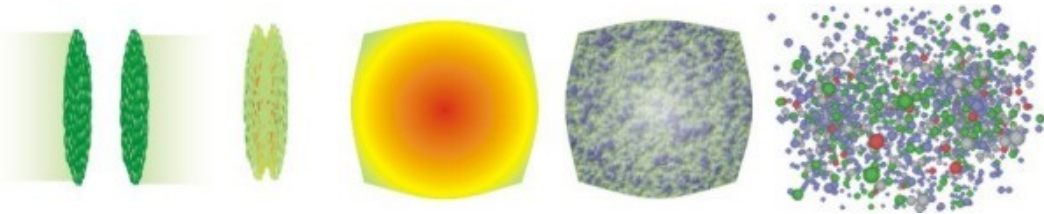


Figure 1.5.: HI Collisions

along their trajectories to be experimentally observed. In order to extract any properties of the QGP medium, the evolution through other phases must be accounted for as well. Hadronization in particular is not understood very well.

Topics of interest for the produced medium include the amount of thermalization of the medium, how strongly-interacting the medium is, the nature of the phase transition itself, among others.

Unfortunately, we are limited in our capabilities to experimentally study the properties of the medium, due to its exceedingly short lifetime. Because of this we are constrained to probes that are produced in the same collision as the medium, such as jets or heavy quarks from a hard scattering.

To understand the experimental measurements of these probes, however, we must understand their initial production cross sections as well.

Our available probes and observables for studying the QGP medium include:

- Elliptic flow of particles to study on the shear viscosity/entropy of the medium.
- Jet modification due to in-medium scattering and energy loss.
- Heavy quark flow as a measure of the medium thermalization.
- Hanbury-Brown-Twiss (HBT) interferometry to evaluate the distribution of matter.
- J/ψ suppression above the QGP transition temperature as a signature of deconfinement.

For a detailed review of experimental and theoretical status, see [17, 18].

To expand upon the last bullet item in the list, the QGP is expected to exhibit screening of the interactions between color charges, similar to Debye screening of electric charges in electromagnetic plasmas. Calculations of the screening length near the transition temperature have led to the conclusion that the J/ψ meson (a charm-anticharm bound

state) is the right size to have its constituent quarks Debye-screened from one another just above T_c . On the other hand J/ψ suppression is also affected by other effects like Cold Nuclear Matter effect and recombination of uncorrelated charm-anticharm quark pair. It is observed that relative suppression Υ family (bound state of $b\bar{b}$) can more robustly signature of Quark Gluon Plasma.

Chapter 2.

Quarkonia production and properties in Hot and dense matter

2.1. Quarkonia

2.1.1. The discovery of quarkonia

In November 1974 a narrow resonance at $3.1 \text{ GeV}/c^2$ in the $\mu^+ \mu^-$ invariant mass spectrum was observed [19, 20] in proton-beryllium and electron positron collisions. The particle was named J/ψ . At that time the world was expected to consist of up, down and strange quarks plus electrons and muons. In addition a fourth quark was predicted by the Glashow-Iliopoulos-Maiani (GIM) mechanism [21]. Soon after the first observation it became clear that the newly discovered particle consisted of the predicted quark species, the so called charm quarks. This discovery added a new particle to the fundamental building blocks of nature. In addition the description of the small width of the observed peak, $93.4 \pm 1.2 \text{ keV}$ [22], was one of the first big successes of QCD, a theory still relatively new at that time. Three years later another sharp resonance in the dimuon spectrum was discovered in proton-nucleus collisions [23], the Υ . This time the surprise in the physics community was not as large since the third lepton, the τ , was discovered in the mean-time and for symmetry reasons one expected a third quark family. The heaviest quark, the top quark, was discovered in 1995 [24]. This discovery completed the three quark families. Up, down and strange quarks are commonly called light quarks, while the charm, bottom and top are referred to as heavy quarks. The bound state of these heavy quarks with their corresponding anti-particle is called quarkonia. The top quark cannot form a bound state, due to its short lifetime of less than 10^{-24}s . A heavy quark-anti-quark pair is able

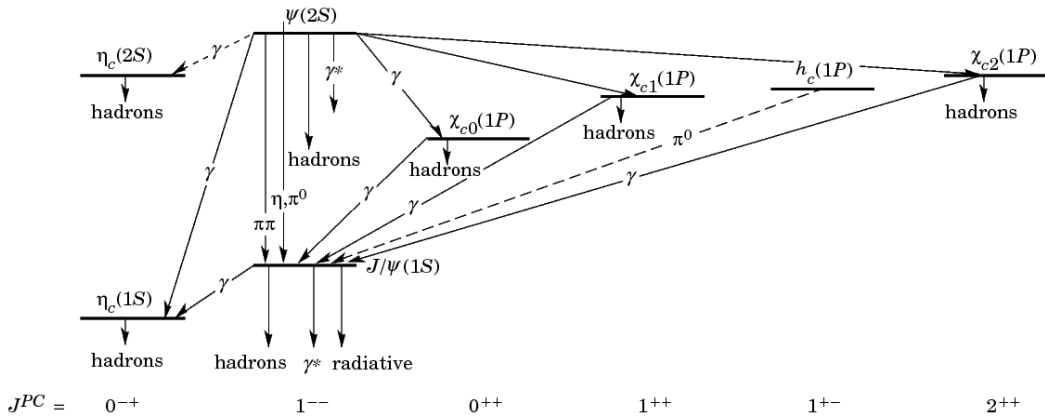


Figure 2.1.: Different bound states of charm and anti-charm quark.

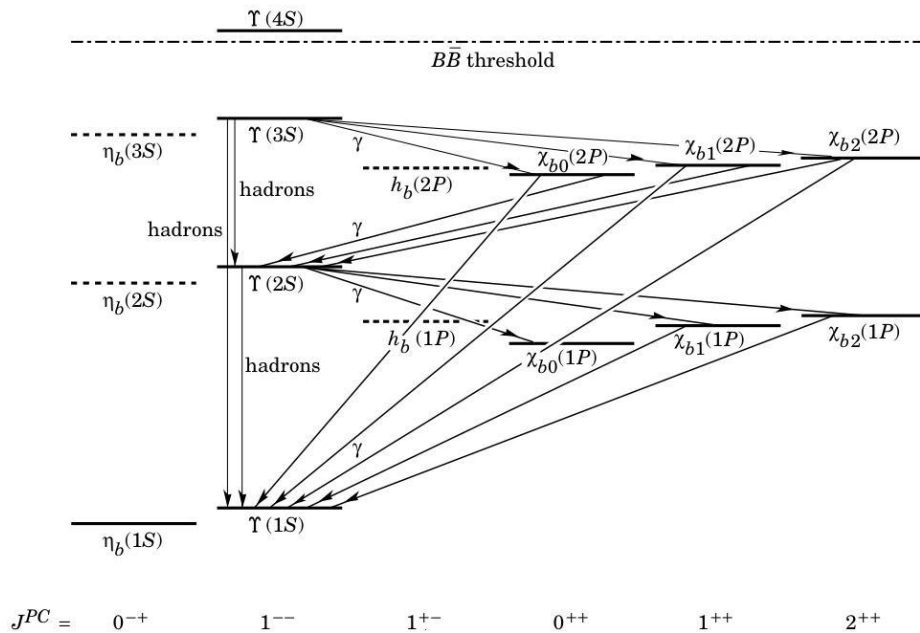


Figure 2.2.: Different bound states of beauty and anti-beauty quark.

to form more than one bound state. Apart from the J/ψ and the Υ more higher excited states exist, forming the so-called $J\psi$ and the Υ families as shown at Figure 2.1 and 2.2 [22].

2.1.2. Quarkonium production

In general one can subdivide the production process into two major parts

- Production of a heavy quark pair in hard collisions.
- Formation of quarkonia out of the two heavy quarks.

Production of a heavy quark pair in hard collisions

Due to the high mass of the heavy quarks ($m_{charm} \sim 1.3 \text{ GeV}/c^2$, $m_{bottom} \sim 4.7 \text{ GeV}/c^2$) the first process can happen only during the first phase of a collision. Only at that time the elementary collisions with sufficiently high momentum transfers to create such high masses take place. For this reason the heavy quark production is a hard process that can be treated perturbatively. In next-to-leading order (NLO) calculations the available experimental data at different energies and collision system [25, 26] were described. The obtained parameters were then used to predict the total production cross section in proton-proton collisions at LHC energies. The charm production cross section is predicted to be 6.3 mb. and the bottom production cross section 0.19 mb [27]. To obtain upper and lower limits for this cross sections the parameters have been varied leading to a relatively large range for the charm production cross section of 4–15 mb and 0.08–0.34 mb for the bottom production cross section.

Formation of quarkonia out of the two heavy quarks

The second part, namely the formation of quarkonia out of the quark-anti-quark pair can a priori not be treated perturbative. Due to the high quark masses and the small relative velocities in the quarkonium system, the formation can be described using non-relativistic QCD (NRQCD). This allows the factorization into a perturbative small-range and high-momentum part and a long-ranged and low-momentum part. In the past years especially three models were developed, namely the Color Singlet Model (CSM) [28, 29], the Color Octet Model [30–32] and the Color Evaporation Model (CEM) [33–35]

- Color Singlet Model (CSM): The quarkonia formed out of the two quarks has to be color neutral. Since in principle the two heavy quarks are not necessarily carriers of one color and the corresponding anti-color, the combination might be colored ¹. The Color Singlet Model rejects all color octet states, in the NRQCD factorization the produced quarkonium has the same quantum numbers as the quark–anti-quark pair. Predictions by the CSM for the

¹The symmetry group of QCD is the SU(3). The colors are triplet, R, G, B and their anti-color \bar{R} , \bar{G} and \bar{B} triplets one can form $3 \otimes 3 = 8 \oplus 1$ combinations, one octet and one singlet. The color octet states are $R\bar{G}$, $R\bar{B}$, $G\bar{R}$, $G\bar{B}$, $B\bar{R}$, $B\bar{G}$, $\sqrt{\frac{1}{2}}(R\bar{R} - G\bar{g})$, $\sqrt{\frac{1}{6}}(R\bar{R} + G\bar{G} - 2B\bar{B})$, . The color singlet is $\sqrt{\frac{1}{6}}(R\bar{R} + G\bar{G} + B\bar{B})$.

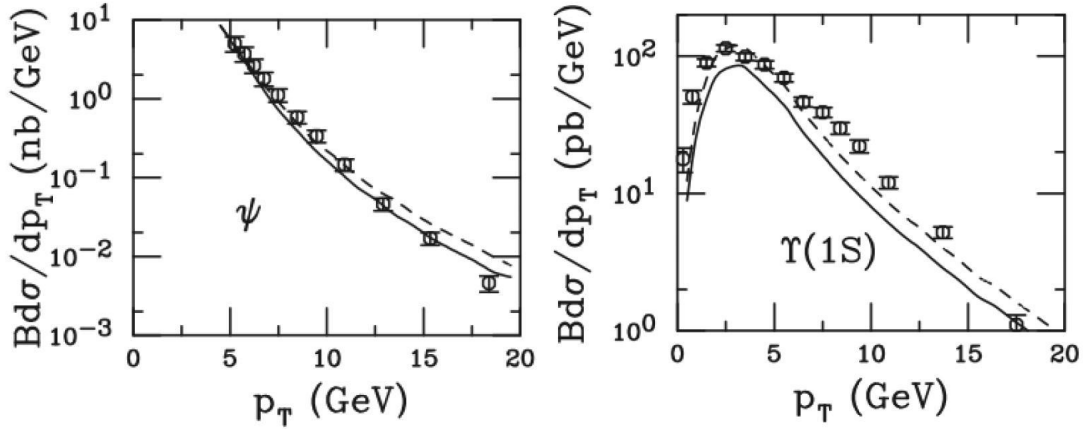


Figure 2.3.: p_T -dependent production of J/ψ s and Υ s as measured by the CDF experiment [36–38] (circles) and compared to predictions by the Color Evaporation Model with two different parameter sets (solid+dotted).

production of quarkonium in pp at Tevatron underestimated the data by an order of magnitude, thus it was clear that the color octet states cannot be neglected.

- Color Octet Model (COM): The Color Octet model considers the octet states, within the model quarkonium is only produced in an octet and thus colored state. The pre-resonant colored state neutralizes its color by the emission of a soft gluon. The Color Octet Model was able to reproduce the production cross section but failed in the description of the observed J/ψ polarization [39].
- Color Evaporation Model (CEM): As an expansion the Color Evaporation Model was developed from the Color Octet Model. The evaporation of the surplus color happens via many different processes, not only by the emission of a soft gluon. This large number of processes results in a relatively large number of parameters, that have to be determined by the comparison to existing data. Although the tuning of the model to the data works well, the large number of free parameters limit the predictive power of the CEM. Nevertheless it is the best available approach for describing the available measurements and it is used for the predictions of the cross sections for LHC energies (see Figure 2.3).

2.1.3. Qualitative formation and decay times

It is commonly accepted that at LHC energies the main production mechanism of heavy quark and quarkonia is gluon fusion $gg \rightarrow Q\bar{Q}$. Gluons from the nucleus wave function

will form a $Q\bar{Q}$ pre-resonance in a characteristic (hard) production time t_p

$$t_p(p_t \gg m_Q) \approx \frac{E}{p_T^2} \approx \frac{1}{p_T}, \quad t_p(p_t \leq m_Q) \sim \frac{1}{m_Q} \quad (2.1)$$

E being the pair energy. Thus, for $p_T \sim m_Q$ the production time of charm and beauty pre-resonance pairs would be about

$$t_p(p_t \gg m_c) \sim 0.15 \text{ fm/c}, \quad t_p(p_t \gg m_b) \sim 0.05 \text{ fm/c}. \quad (2.2)$$

The production time is then much smaller than 1 fm/c, and they are formed at a relative distance $1/m_Q \gg 1 \text{ fm}$. Then the $Q\bar{Q}$ pairs travel extremely close and to form a $Q\bar{Q}$ resonance they need to expand till the characteristic size of the resonance. It can be interpreted as the time the pair takes to decide which of the possible $Q\bar{Q}$ bound-states it will couple to (one with mass m_1 or one with m_2). This formation time can be calculated by means of [40, 41]

$$t_f \simeq \frac{2E}{m_2^2 - m_1^2} \quad (2.3)$$

Thus the time a $c\bar{c}$ ($b\bar{b}$) pair takes to decide to form a J/ψ (Υ) rather than a excited state

$$\begin{aligned} t_f(J/\psi, E) &\simeq \frac{2E}{m_{J/\psi}^2 - m_{\psi'}^2} \\ t_f(J/\psi, 10 \text{ GeV}) &\simeq 1.0 \text{ fm/c.} \\ t_f(J/\psi, 30 \text{ GeV}) &\simeq 3.0 \text{ fm/c.} \end{aligned} \quad (2.4)$$

similarly for Υ family

$$\begin{aligned}
t_f(\Upsilon, E) &\simeq \frac{2E}{m_\Upsilon^2 - m_{\Upsilon'}^2} \\
t_f(\Upsilon, 10\text{GeV}) &\simeq 0.36\text{fm}/c. \\
t_f(\Upsilon, 30\text{GeV}) &\simeq 1.1\text{fm}/c.
\end{aligned} \tag{2.5}$$

The resonances formation times are thus much larger than the preresonances production times. They increase with the particle momentum, ranging from a fraction of fm/c to about 3 fm/c. Later, the $Q\bar{Q}$ resonance being not a stable particle, it will decay with a characteristic proper time inversely proportional to its width

$$t_d \simeq \frac{1}{\Gamma} \tag{2.6}$$

The J/ψ and Υ decay time would then be of about

$$t_d(J/\psi) \simeq \frac{1}{93\text{keV}} = 2.1 \times 10^3 \text{fm}/c, \quad t_d(\Upsilon) \simeq \frac{1}{54\text{keV}} = 3.7 \times 10^3 \text{fm}/c. \tag{2.7}$$

Theoretical calculations estimate that at LHC energies the QGP might be formed in about 0.1 fm/c and might last ≥ 10 fm/c. The previous calculations suggest that: the $Q\bar{Q}$ pre-resonances are produced while the QGP is formed, but the $Q\bar{Q}$ resonances are formed in coexistence with the QGP, and may decay out of it.

2.1.4. Quarkonium binding potential

Since heavy quarks are massive, quarkonium spectroscopy can be studied in non-relativistic quantum mechanics. The confining potential for a $Q\bar{Q}$ pair at a separation distance r can be modeled by [1, 42]

$$V_{Q\bar{Q}} = \sigma(T) - \frac{\alpha_{eff}}{r} \tag{2.8}$$

$$(2.9)$$

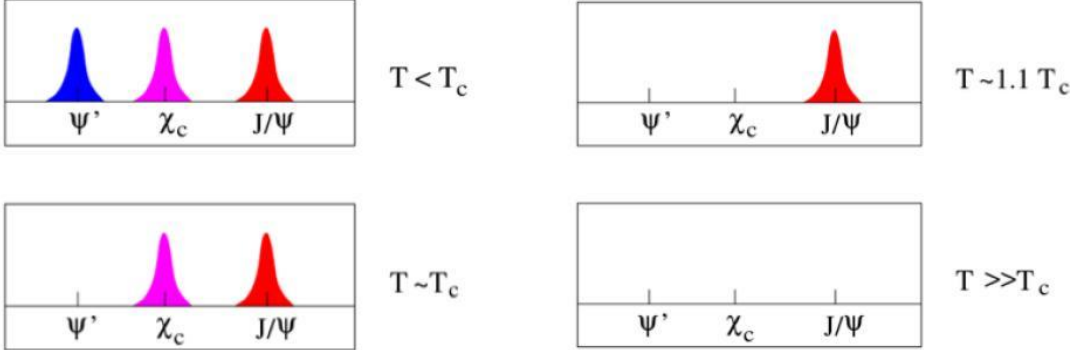


Figure 2.4.: Charmonium spectra at different temperatures [42].

where $\sigma \simeq 0.216 \text{ GeV}^2$ is the string tension (for $T \sim 0$), and $\alpha_{eff} \simeq \frac{\pi}{12}$ accounts for the Coulombian-like interaction. At small distances (r small), the Coulombian-like interaction is predominant, whereas at large distances the attractive force of the confinement described by the string tension prevails. The latter increasing linearly with the distance, a big amount of energy would be needed to separate the heavy quarks, they are tightly bound. Above T_C quarks and gluons are no longer confined and the large color charge present in the medium screens the inter-quark potential, the so called color screening. The potential is then expected to be described by a Debye-screening form

$$V_{Q\bar{Q}}^{QGP}(r, T) = -\frac{\alpha_{eff}}{r} e^{-\frac{r}{\lambda_D(T)}} \quad (2.10)$$

$\lambda_D(T)$ being the Debye screening length. $\lambda_D(T)$ diminishing with the system temperature, the inter-quark potential is reduced accordingly, and when $\lambda_D(T) \leq r_{hadron}$ the inter-quark force can not hold the quarks together, and they dissociate.

LQCD can give accurate estimates of the quarkonium binding potential as a function of the system temperature and the inter-quark separation r in the relativistic limit. Such calculations allow them to predict the dissociation temperatures T_d of the quarkonium states. Table 2.1 summarizes the results obtained by using the full internal energy (including the entropy term) [1, 43]. An illustration of the situation for the charmonium dissociation temperatures is displayed in Figure 2.4. A “sequential melting” pattern of the various charmonium states with their binding energy is observed, the ground state disappearing the last. Recent LQCD calculations support the late dissociation of $J/\psi(\Upsilon)$ at about $T_d/T_c = 1.5(3.2)$ [44] in agreement with LQCD spectral analysis of the hadron correlation functions [45].

Table 2.1.: Dissociation temperatures of the quarkonium resonances from LQCD. Where E_b stands for the binding energy [1, 22, 43].

	J/ ψ (1S)	χ_c (1P)	ψ^1 (2S)	Υ (1S)	χ_b (1P)	Υ (2S)	χ_b (2P)	Υ (3S)
M[GeV]	3.10	3.41	3.69	9.46	9.86	10.02	10.23	10.36
E_b [GeV]	0.64	0.20	0.05	1.10	0.67	0.54	0.31	0.20
$\frac{T_d}{T_c}$	2.1	1.16	1.12	≥ 4.0	1.76	1.60	1.19	1.17

2.2. Experimental Status of Quarkonia Suppression

2.2.1. J/ ψ anomalous suppression at SPS

A first J/ ψ suppression was observed and reported by the NA38 experiment [46], which was performed with oxygen-uranium collisions of incident energy 200 GeV per nucleon. Figure 2.6 shows the measured J/ ψ yield normalized to the number of dimuons in mass range 2.7–3.5 GeV/c² as a function of transverse energy (E_T) corresponded to centrality. A similar pattern was observed later in sulphur-uranium collisions [47]. Increasing centrality, the nuclear matter is more and more compressed, at some point a volume of deconfined matter forms with free color charges. Charmonium binding potential is screened and the bound state is dissolved and then the measured J/ ψ production decreases with respect to the reference. Because the ratio would be expected to remain constant with respect to the centrality if charmonium is not suppressed. However, another trial of explanation is possible without deconfinement for the charmonium dissociation. It can be happened in the interactions with nucleons. As pointed out in [50] the observed suppression is able to be presented by the breakup of charmonium caused by scattering off nucleons, where the matter is confined. The experiment of smaller system such as proton–nucleus or deuterium–nucleus collisions was designed to examine this effect, namely nuclear absorption. Indeed the effect of nuclear absorption was measured, absorption cross section as $\sigma_{\text{abs}} = 7.3 \pm 0.6$ mb [50]. The NA50 experiment compared the charmonium production to the Drell-Yan ($q\bar{q} \rightarrow l^+l^-$) process, since the compete dimuon continuum in the J/ ψ mass range can not be predicted from theory [48]. Figure 2.5 illustrates the ratio of J/ ψ and Drell–Yan process as a function of L, the length of traversed nuclear matter, which can be obtained from Glauber model calculation [49, 50]. Thus the line shows the amount of suppression due to nuclear absorption, that can not be related to the dissociation from deconfinement. A clear deviation from this line can be observed for $L > 7.5$ fm. This suppression is called the anomalous suppression.

To determine the energy density necessary to melt charmonium, measurements on smaller systems have been performed. Although the maximum achievable energy density is smaller than in collisions of larger nuclei, smaller systems enable a higher resolution centrality scan. The results are shown in Figure 2.7 (left) [51]. The J/ψ /Drell-Yan production is plotted as a function of the number of participants in the collision, where the data is normalized to cold matter effects. A suppression exceeding the nuclear suppression is seen starting from 80 participants on. In Figure 2.7 (right) the data is compared to the results of the NA50 experiments from lead-lead collisions of the same energy of 158 GeV per nucleon. For peripheral collisions the ratio of measured/expected J/ψ yield is as expected, close to one, any observed dissociation is attributed to cold nuclear effects. For more central collisions a clear deviation from the expected behavior is observed, with good agreement between the In–In and the Pb–Pb data. The measurement of ψ' has been performed as shown in Figure 2.8. All the measurements suffer from the significantly lower statistics accumulated for the ψ' , because it is not only due to the lower production cross section, but dominantly due to the lower branching into dileptons ($\sigma_{\psi'} \rightarrow l^+l^- = 0.73\%$ compared to $\sigma_{J/\psi} \rightarrow l^+l^- = 5.9\%$). Figure 2.8 presents the similar suppression of ψ' is observed compared to the J/ψ only the onset of the anomalous suppression is already at $L = 4\text{fm}$ and thus happens at a lower energy density.

2.2.2. J/ψ and $\Upsilon(nS)$ suppression at RHIC

At RHIC J/ψ yield in AA collisions is compared with scaled yield in p+p collisions. It gives a new variable known as Nuclear Modification Factor or R_{AA} .

$$R_{AA} = \frac{1}{N_{Coll}} \frac{\frac{d^2 N_{AA}^{J/\Psi}}{dy dp_T}}{\frac{d^2 N_{pp}^{J/\Psi}}{dy dp_T}} \quad (2.11)$$

$$(2.12)$$

J/ψ suppression at PHENIX

Figure 2.9 shows the suppression pattern observed by PHENIX in Au–Au and Cu–Cu collisions. The suppression of J/ψ is observed in the more central collisions. Since cold nuclear matter effects are not subtracted here the observed suppression can not be attributed to the dissociation of quarkonia in the deconfined medium alone. Figure 2.10 presents the ratio of R_{AA} and cold nuclear matter effects (CNM) [52]. For the

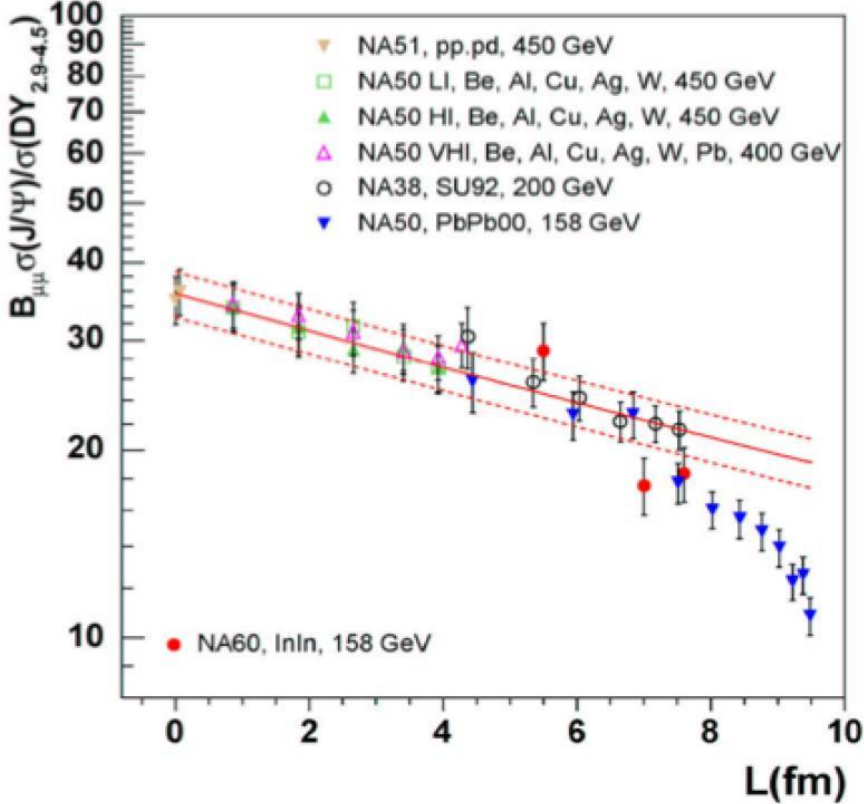


Figure 2.5.: J/ψ over Drell–Yan production cross–section ratio as a function of the length traversed by the charmonium in nuclear matter (L) for various colliding systems [53].

comparison to previous results, the J/ψ data taken by NA50 and NA60 are included. The data agree quite well between SPS and RHIC in the lower energy densities, while the suppression observed at RHIC clearly exceeds the maximal suppression measured at SPS of $R_{AA}/CNM = 60\%$ in the higher energy densities

In particular, PHENIX measured R_{AA} at different rapidity region. Figure 2.10 illustrates $J/\psi R_{AA}$ in four different centrality bins as a function of rapidity. While R_{AA} is almost constant for peripheral collisions (centrality bins 40-60 % and 60-92 %), the central collisions show a clear difference between forward and mid rapidity. The suppression of J/ψ production is significantly lower in forward/backward direction compared to the observed suppression at mid rapidity. This phenomenon could so far not be explained by current quarkonia production and suppression models.

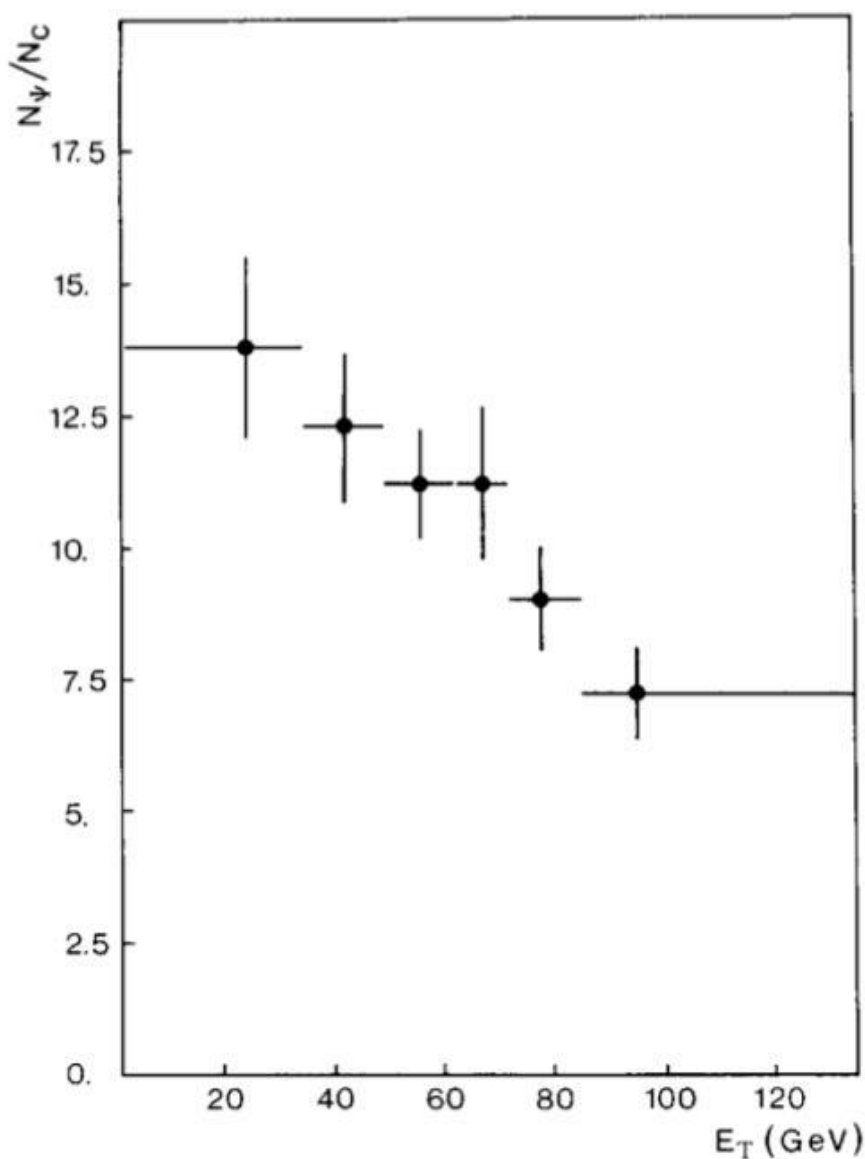


Figure 2.6.: The ratio of produced J/ψ and dimuons as a function of the transverse energy as measured by NA38 [46].

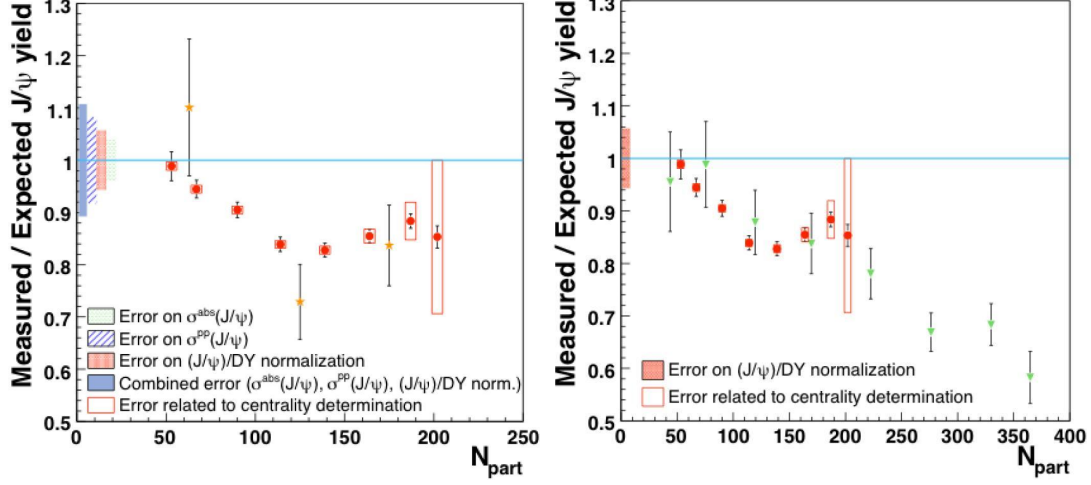


Figure 2.7.: The centrality dependence of the J/ψ suppression for In–In collisions at 158 GeV per nucleon measured by NA60 (left). A comparison between the NA60 In–In and the NA50 Pb–Pb data (right).

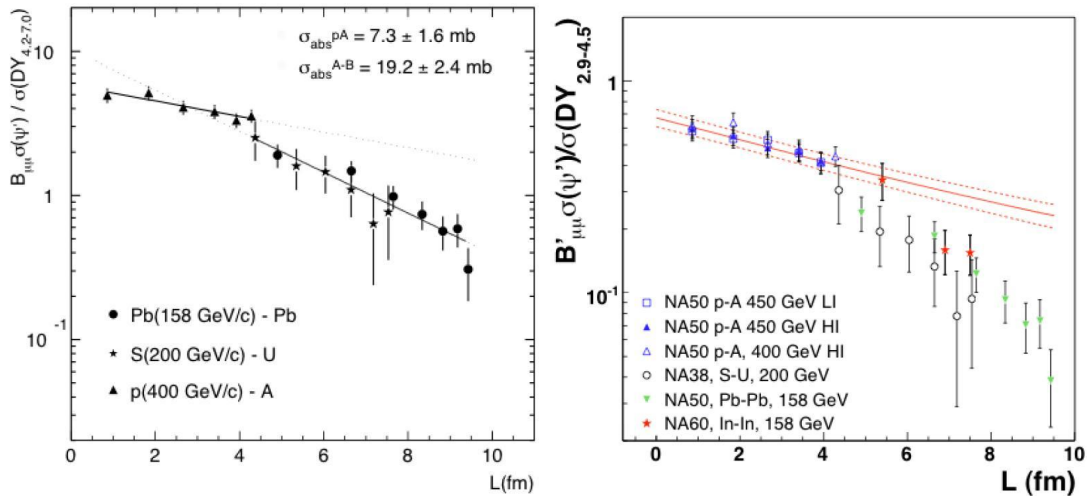


Figure 2.8.: The ratio between cross section of ψ' times the branching into muons ($B_{\mu^+\mu^-}$) and the cross section of Drell–Yan reference process as measured by the NA50 and NA60 at various energies and in different collisional systems

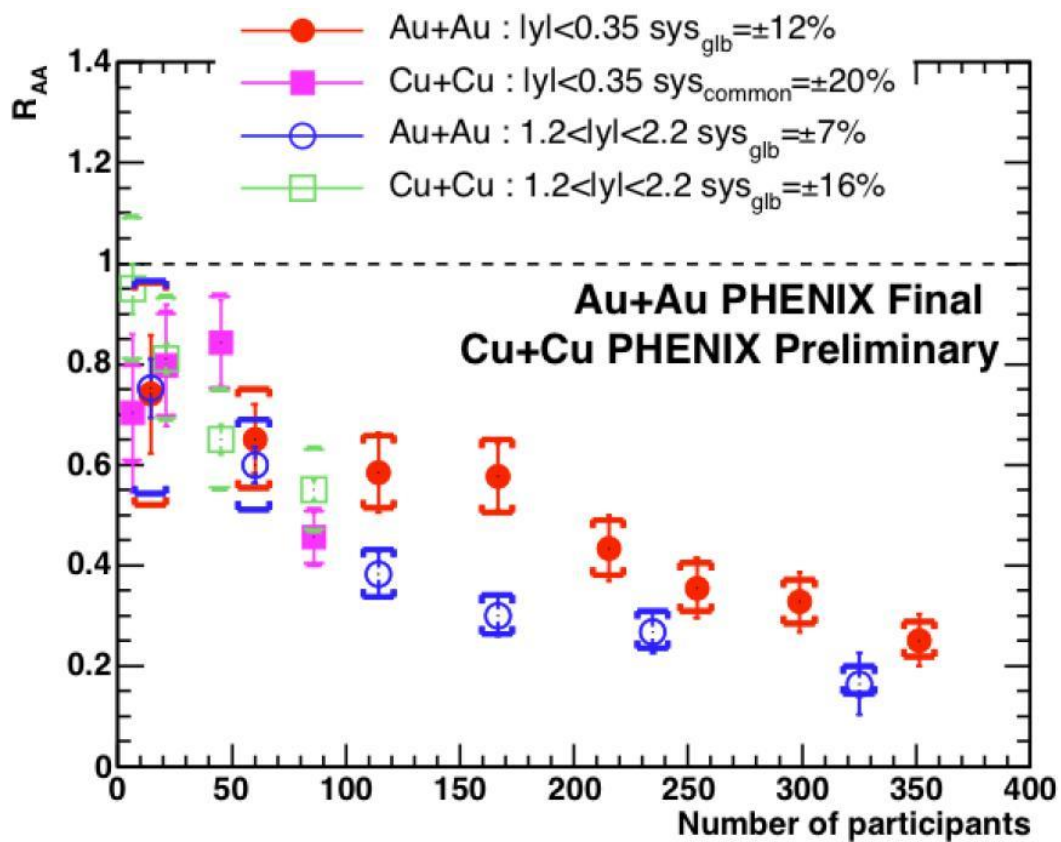


Figure 2.9.: R_{AA} as a function of Npart measured by PHENIX in Au–Au (in circles) and Cu–Cu (in squares) [54].

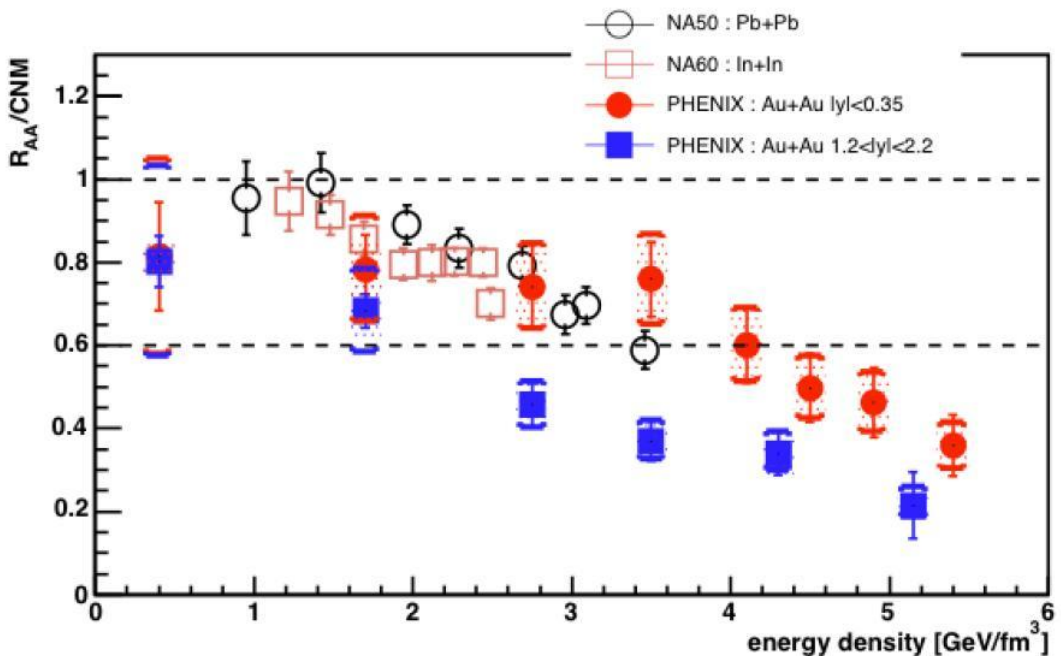


Figure 2.10.: R_{AA}/CNM as a function of the Bjorken estimate of the energy density. The RHIC data ($\sqrt{s_{NN}} = 200$ GeV) is compared to SPS (17.3 GeV) measurements performed by NA50 and NA60 [70]. PHENIX estimates the cold nuclear matter effects from measurements on d–Au, while the NA50 and NA60 rely on theoretical calculations.

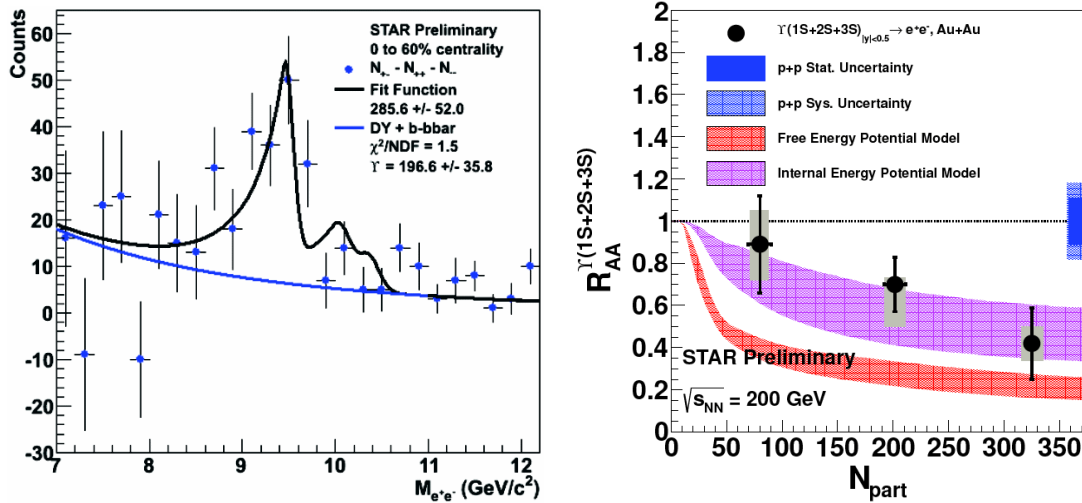


Figure 2.11.: left: e^+e^- pairs as measured in STAR detector at RHIC in 0%-60% centrality class. The blue curve is the combination of Drell–Yan and $b\bar{b}$ background. The black curve includes the Upsilon signal also. right: R_{AA} for 2010 Au+Au compared to 2009 p+p. The magenta and orange curves are theoretical predictions using a combination of lattice-based QCD and hydrodynamical expansion and cooling [56].

$\Upsilon(nS)$ suppression at RHIC

STAR experiment at RHIC measure high p_T J/ψ and Υ states. Due to small production cross-section of b quark at 200 GeV, total yield of Υ is very small. STAR measure e^+e^- pairs at mid rapidity ($|y| \leq 0.5$). The unlike sign invariant mass distribution, after subtracting like sign background is shown in Figure 2.11:left. The measured yield contain Υ signal as well as background from Drell–Yan and semileptonic decay of open beauty mesons. The line-shape of the $\Upsilon(1S+2S+3S)$ was parameterized with three crystal ball functions representing the successive states. Different Υ states can not be separated because of poor mass resolution as shown in Figure 2.11:left. Measured Υ yield is divided in to three centrality bins: 0 % to 10%, 10% to 30%, and 30% to 60%. R_{AA} for the three centrality bins is shown in Figure 2.11:right. The results are compared to a model [55] which incorporates lattice-based QCD calculations with a hydrodynamic model of expansion and cooling.

Figure 2.12 shows ΥR_{AA} compared with high p_T J/ψ measured by STAR. A clear trend versus centrality can be seen in this graph. The red dotted line is the ratio of the total cross-section of $\Upsilon(1S)/\Upsilon(1S+2S+3S)$. The purple dashed line is the ratio of only the direct $\Upsilon(1S)$ cross-section over the total $\Upsilon(1S+2S+3S)$ cross-section. ΥR_{AA} is comparable to J/ψ in most central collisions.

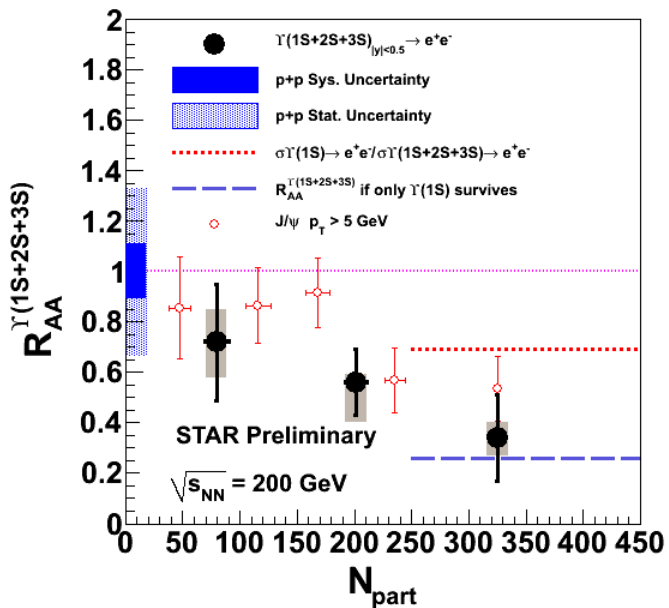


Figure 2.12.: R_{AA} for $\Upsilon(1S + 2S + 3S)$ versus centrality measured by STAR experiment at RHIC. The solid black points are the Υ R_{AA} . The red open points are the high p_T J/ψ results from STAR. Υ R_{AA} is comparable to J/ψ in most central collisions.[57]

Chapter 3.

The Compact Muon Solenoid Experiment at The CERN Large Hadron Collider

3.1. The LHC

The Large Hadron Collider (LHC) at CERN near Geneva is the world's newest and most powerful tool for Particle Physics research. It is designed to collide proton beams with a centre-of-mass energy of 14 TeV and an unprecedented luminosity of $10^{34} \text{ cm}^{-2}\text{s}^{-1}$. It can also collide heavy (Pb) ions with an energy of 2.8 TeV per nucleon and a peak luminosity of $10^{27} \text{ cm}^{-2} \text{ s}^{-1}$

It has circumference of 27 kms and is placed in a tunnel, 175 meters under the ground near Geneva. The tunnel was originally built for the Large Electron-Positron collider [58]. For the LHC operation, they have been upgraded to provide beams of protons for collisions at unprecedented energies. Technical limitations in the production and storage of antiprotons led to the decision to build a proton-proton collider. Accelerated electrons and positrons suffer large energy loss due to the synchrotron radiation, which is proportional to $\frac{E^4}{(Rm^4)}$, where E is the electron energy, m is the particle's mass and R the accelerator radius. Therefore, only massive charged particles could have been used, e.g. protons and heavy nuclei, in order to obtain energies of the order of TeV at the fixed accelerator radius.

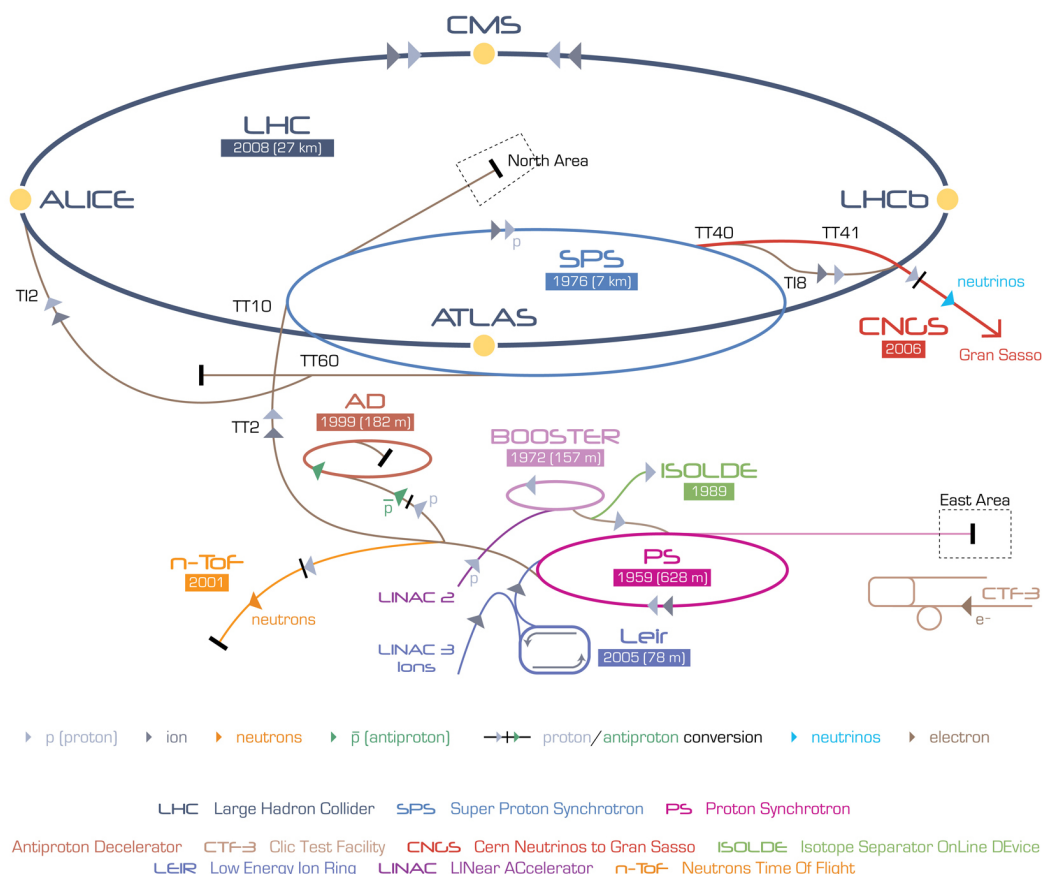


Figure 3.1.: LHC accelerator complex

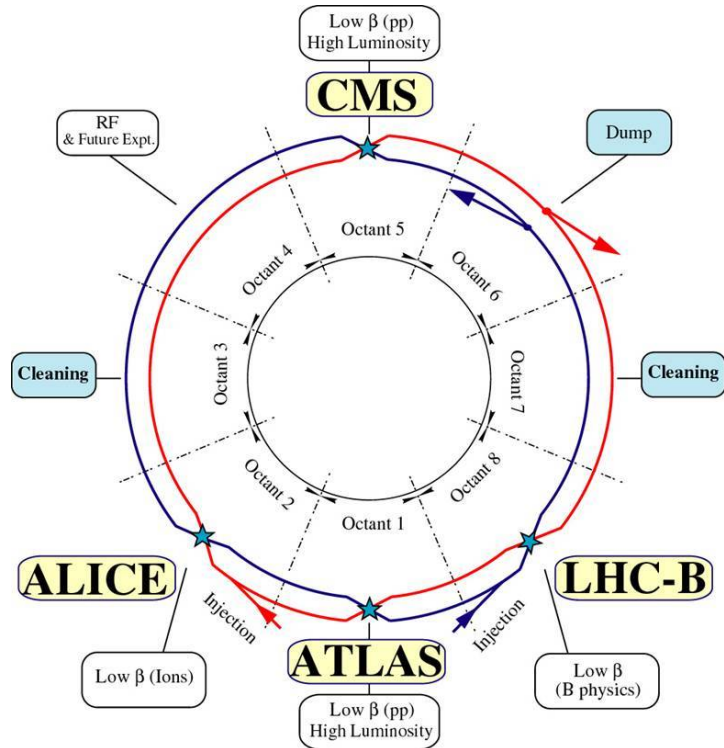


Figure 3.2.: LHC ring

3.1.1. The Accelerator Chain

The LHC is constituted by 1232 super-conducting dipole magnets each 15 m long, delivering a 8.3 T magnetic field to let the beams circulate inside their trajectories along the 27 km circumference. Two vacuum pipes are utilized to let beams circulate in opposite directions. More than 8000 other magnets are utilized for the beam injection, their collimation, trajectory correction, crossing. All the magnets are kept cool by superfluid helium at 1.9 K temperature. The beams are accelerated from 450 GeV (the injection energy from the SPS) to 7 TeV with 16 Radio Frequency cavities (8 per beam) which raise the beam energy by 16 MeV each round with an electric field of 5 MV/m oscillating at 400 MHz frequency. Before the injection into the LHC, the beams are produced and accelerated by different 26 components of the CERN accelerator complex. Being produced from ionized hydrogen atoms, protons are accelerated by the linear accelerator LINAC, Booster and the Proton Synchrotron (PS) up to 26 GeV energy, the bunches being separated by 25 ns each. The beams are then injected into the Super Proton Synchrotron (SPS) where they are accelerated up to 450 GeV. They are then finally transferred to the LHC and accelerated up to 7 TeV energy per beam.

Figure 3.1 shows the full CERN accelerator complex.

In addition to $p + p$ operation, the LHC had heavy nuclei ($Pb + Pb$) collisions in 2009 and 2011 with an energy of 2.76 TeV per nucleon. The availability of high energy heavy-ion beams at energies over 30 times higher than at the present other accelerators will allow us to further extend the range of the heavy-ion physics program to include studies of hot nuclear matter.

The two LHC symmetrical rings are divided into eight octants and arcs and eight straight sections approximately 528 m 3.2. The two high luminosity experimental insertions are located at diametrically opposite straight sections: the A Toroidal LHC ApparatuS (ATLAS) experiment is located at Point 1 and the Compact Muon Solenoid (CMS) experiment at Point 5. The other two large experiments, A Large Ion Collider Experiment (ALICE) and Large Hadron Collider beauty (LHCb), are located at Point 2 and at Point 8, respectively, where the machine reaches a lower luminosity of $L = 5 \times 10^{32} cm^{-2}s^{-1}$. The remaining four straight sections do not have beam crossings. The two beams are injected into the LHC in two different octants, octant 2 and octant 8 respectively for clockwise and anticlockwise beam. The octants 3 and 7, instead, contain two collimation systems for the beam cleaning.

3.2. Luminosity

The number of events per second generated in the LHC collisions is given by : $N = L\sigma$ where σ is the cross section for the collisions process under study and L the machine luminosity. The machine luminosity depends only on the beam parameters and can be written, for a Gaussian beam distribution, as:

$$L = \frac{n \cdot f_{rev} \cdot N_1 \cdot N_2}{A_T^{eff}} \quad (3.1)$$

where A_T^{eff} is the effective transverse area of the proton beam, n is the number of packets the beam is splitted to and f_{rev} is the frequency of revolution around the ring. N_1 and N_2 are the number of protons in each packet. With respect to other high energy colliders, the design luminosity of LHC is several magnitudes larger. This is needed because LHC is designed to discover new particles at TeV scale. At these scales the

interaction rates with momentum transfers more than 1 TeV are very low. Therefore more data needs to be collected which can only be achieved by having large luminosity.

The LHC luminosity is not constant over physics a run, but decays due to the degradation of intensities and emittance of circulating beams. The main cause of the luminosity decay during normal LHC operation is the beam loss from collisions.

3.3. Compact Muon Solenoid

The CMS experiment is a general purpose proton-proton detector designed to run at the highest luminosity of LHC. Figure 3.3 gives a 3D structure view of the CMS detector. The design of the CMS detector is based on a compact superconducting solenoid coupled with a muon detector system for optimized muon detection. Superconducting solenoid provides a strong magnetic field of 3.8 T. Inside it, the inner tracking comprises a Pixel detector surrounded by the Silicon Strip detector. Its high granularity (70 millions pixels, 10 millions strip) and precision ensures good track reconstruction efficiency. It is surrounded by Electromagnetic calorimeter (ECAL) made of 76000 lead tungstate crystals grouped in 36 barrel and 4 endcap supermodules. The brass-scintillator sampling hadron calorimeter (HCAL) completes the in-coil detectors. To ensure hermeticity the in-coil calorimetric system is extended, away from the central dector, by the hadron outer detector (HO) and a quartz fiber very forward calorimeter (HF) to cover $\eta \leq 5$. Outside the solenoid a muon system is built in the magnet steel return yoke. It's formed by 4 stations of muon chambers: Drift Tube (DT) in the barrel region, Cathode Strip Chambers (CSC) in the endcap, Resistive Plate Chamber (RPC) in both parts, providing muon detection redundancy.

Two trigger levels are employed in CMS. The Level-1 Trigger (L1) is implemented using custom hardware processors and is designed to reduce the event rate to 100 kHz during LHC operation using information from the calorimeters and the muon detectors. It operates nearly dead time-free and synchronously with the LHC bunch crossing frequency of 40 MHz. The High Level Trigger (HLT) is implemented across a large cluster of commodity computers referred to as the event filter farm, and provides further rate reduction to $\mathcal{O}(100)$ Hz using filtering software applied to data from all detectors at full granularity. The overall dimension of CMS are a length of 21.6 m, a diameter of 14.6 m and a total weight of 12500 tons.

CMS Detector

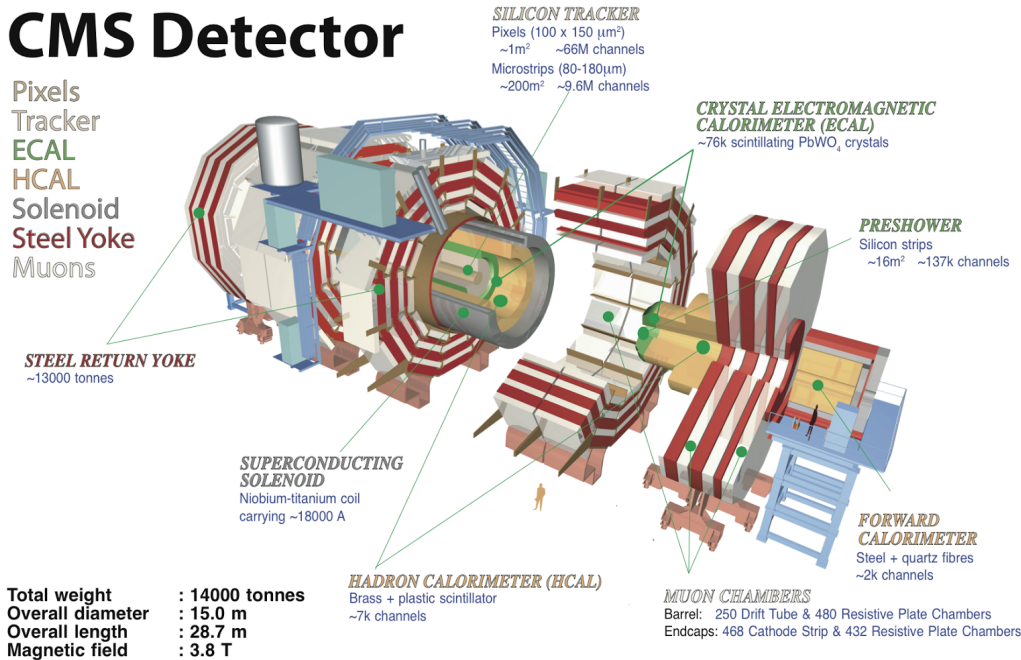


Figure 3.3.: CMS detector figure

A slice of the transverse view of the CMS detector is shown in Figure 3.4. The principle of detection of charged and neutral particles in the various sub-detectors is shown. All charged particles leave signals in the inner tracking system. Electrons and photons deposit their energy in the electromagnetic calorimeter. Charged Hadrons (K^\pm , π^\pm ...) and neutrons deposit their energy in the hadronic calorimeter. Muon is a particle which passes through calorimeters without interacting much, but which leaves a track of its passage in the muon chambers. Neutrinos, barely interacting, will escape from all direct detections. While adding the transverse momenta of all the particles detected by the detector, one can determine the imbalance of energy in the transverse plane, so called the missing transverse energy.

The coordinate system of CMS has its origin inside the detector at the primary interaction point. The x-axis points radially towards the center of the LHC, whereas the y-axis points vertically upward. Thus, the z-axis shares the same direction with the beam line. The azimuthal angle ϕ is measured from the x-axis in the x-y plane whereas the polar angle θ is measured from the z-axis.

Particle physicists often use a quantity called rapidity y instead of θ . It is defined as:

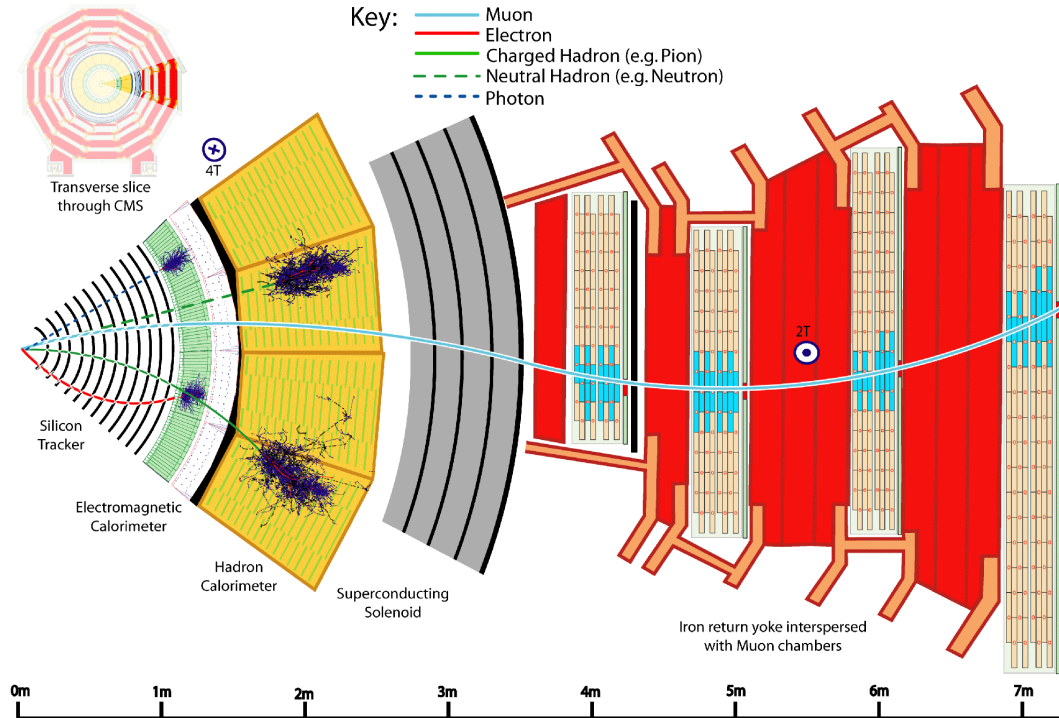


Figure 3.4.: CMS detector figure slice

$$y = \frac{1}{2} \ln \frac{E + p_z}{E - p_z} = \tanh^{-1} \frac{p_z}{E} \quad (3.2)$$

and equals, in case of massless particles, the pseudorapidity η given by

$$\eta = -\ln[\tan(\theta/2)] \quad (3.3)$$

The use of rapidity instead of the polar angle is motivated by the fact that the difference in rapidity between two particles is invariant under Lorentz boosts along the beam axis

The angular distance between two particles observed from the origin of the coordinate system is

$$\Delta R = \sqrt{\Delta\phi^2 + \Delta\eta^2} \quad (3.4)$$

Measurable quantities like momentum and energy transverse to the beam line are denoted by p_T and E_T , respectively, and can be derived from its x and y components. The CMS detector is located north of the LHC center. The origin of the CMS coordinate system is the CMS collision point. Neglecting the small tilt of the LEP/LHC plane.

3.3.1. Magnet

The superconducting solenoid magnet reaches a maximum magnetic field of 3.8 T in the positive z direction in the inner detectors. A high magnetic field provides a large bending power in the transverse plane for charged particles, which makes possible to reach precise measurement of muon momenta. The magnet is 12.5 m long and with an inner radius of 6 m and is made of four-layers of NbTi. It is the largest superconducting magnet ever built, with the capacity to store an energy of 2.6 GJ at full current. The magnetic flux is returned via a 1.5 m thick iron yoke instrumented with four stations of muon chambers. In this part of the detector the magnetic field is saturated at 2 T. More detailed information can be found in reference [59] Figure 3.5 shows artistic view of CMS magnet, a huminoid is also present on figure to highlight the huge size of magnet.

3.3.2. Tracker

The Tracker is the subdetector system which is closest to the interaction point, a general layout is presented in Figure 3.6 It is designed to provide an efficient measurement of the trajectories of charged particles emerging from the LHC collisions, as well as a precise reconstruction of secondary vertices. The CMS Tracking System is composed of q silicon pixel detector close to the interaction region and a strip detector covering radii from 0.2 m to 1.1 m. The Pixel Detector consists of 1440 pixel modules arranged in three barrel layers and two disks in each end-cap. The barrel layers are located at radii of 4.4, 7.3 and 10.2 cm around the interaction point with a length of 53 cm. On each side of the barrel, two discs are placed at $|z| = 32.5$ cm and 46.5 cm.

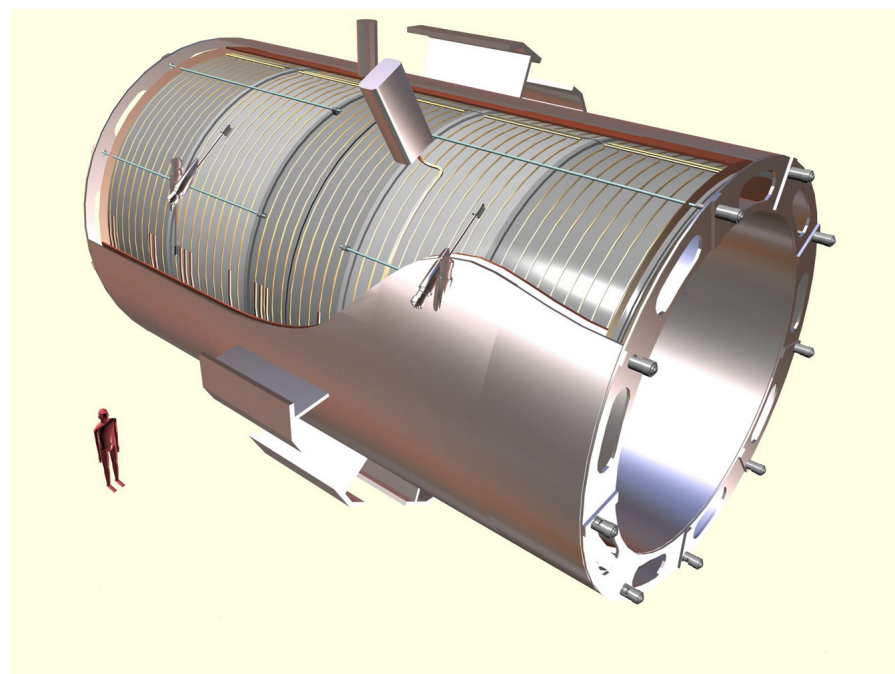


Figure 3.5.: CMS Magnet

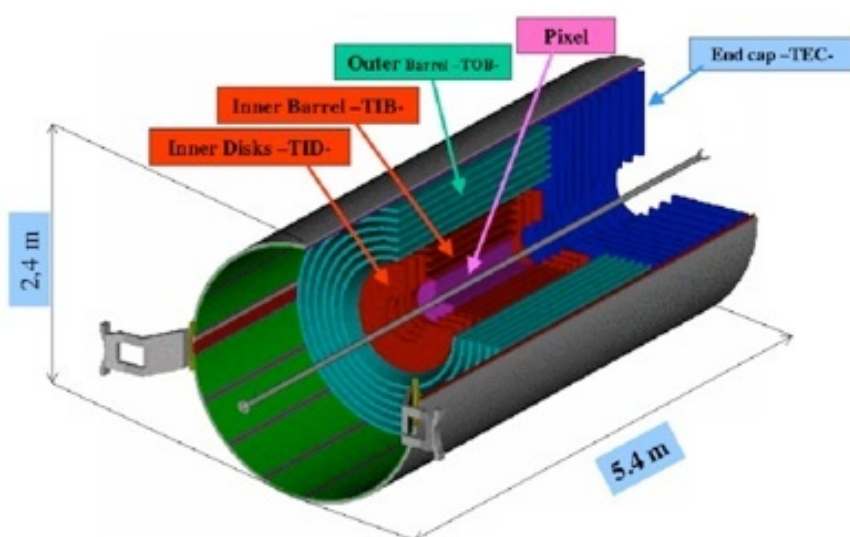


Figure 3.6.: CMS Tracker drawing

3.3.3. Calorimetry

ECAL

The electromagnetic calorimeter (ECAL) is used to measure the energy of photons and electrons. The ECAL is a high precision scintillating crystal calorimeter. The structure of the ECAL can be seen in Figure 3.7. It is composed of 61,200 lead tungstate (PbWO_4) crystals in the barrel region and 7,324 crystals in the endcaps. The choice of that material is motivated by its fast response and high radiation resistance and its very good resolution. In front of each ECAL Endcap is a preshower detector (ES), from $1.65 \leq |\eta| \leq 2.6$ made from silicon strip detectors in order to identify neutral pions (π^0). The nominal energy resolution, measured with electron beams having momenta between 20 and 250 GeV, is:

$$\frac{\sigma_E}{E} = \left(\frac{S}{\sqrt{E}}\right)^2 + \left(\frac{N}{E}\right)^2 + C^2. \quad (3.5)$$

where S is the stochastic term, which includes fluctuations in the shower containment as well as a contribution from photostatistics, N is the noise term, which accounts for the electronic, digitization, and pileup noise, and C is the constant term, which comes from the light collection non-uniformity, errors on the inter-calibration among the modules, and the energy leakage from the back of the crystal.

HCAL

The hadronic calorimeter (HCAL) is designed to measure the energy of hadrons. The HCAL is comprised of four subsystems: the HCAL Barrel (HB), the outer calorimeter (HO), the HCAL Endcap (HE), and the forward calorimeter (HF). Figure 3.8 gives a schematic overview on the HCAL sub-detector. The HB is a sampling calorimeter that covers the range $|\eta| < 1.3$. It consists of 36 identical azimuthal wedges aligned parallel to the beamline. It is located between the ECAL and the solenoid coil and is supplemented by the HO located between the solenoid and the muon chambers. The HO is designed to absorb the remnant of the hadronic shower which has not been fully absorbed in the HB. The HE covers a large portion of the solid angle, $1.3 < |\eta| < 3$. Beyond that region,

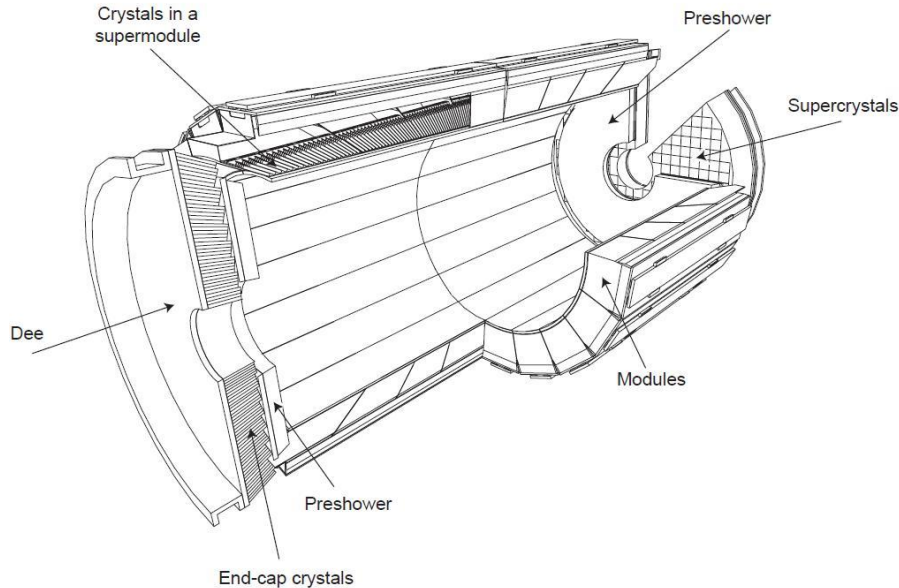


Figure 3.7.: CMS ECAL detector

the HF placed at 11.2 m from the interaction point extends the pseudorapidity coverage up to $|\eta| \leq 5.2$. The HE must have high radiation tolerance, with 10 Mrad expected after 10 years of operation. The reason for the absorber material to be non-magnetic is that it must not affect the magnetic field. The HF experiences the harshest radiation environment and therefore requires an extremely radiation tolerant material. The active material chosen is quartz fibers. The fibers are mounted in grooves in the steel absorber plates. The inner part of the HF will be exposed to close to 100 Mrad/year. As the absorber will become radioactive the entire HF can be moved into a garage to limit exposure of personnel during maintenance periods.

3.3.4. CMS Muon System

One of the main design objectives of the CMS detector was to obtain a high precision muon momentum measurement, for its key role both in new physics searches and in Standard Model measurements. The CMS muon system [60] uses three different types of gaseous detectors to detect muons. In the barrel region, Drift Tubes (DTs) and Resistive Plate Chambers (RPCs) are used, while in the endcap there are Cathode Strip Chambers (CSCs) and also RPCs. The layout of the CMS muon system is shown in Figure 3.9.

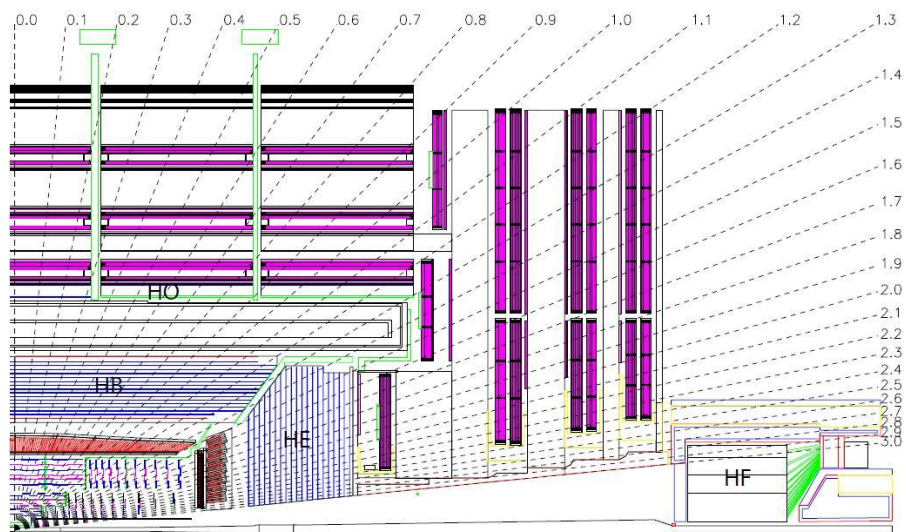


Figure 3.8.: CMS HCAL detector

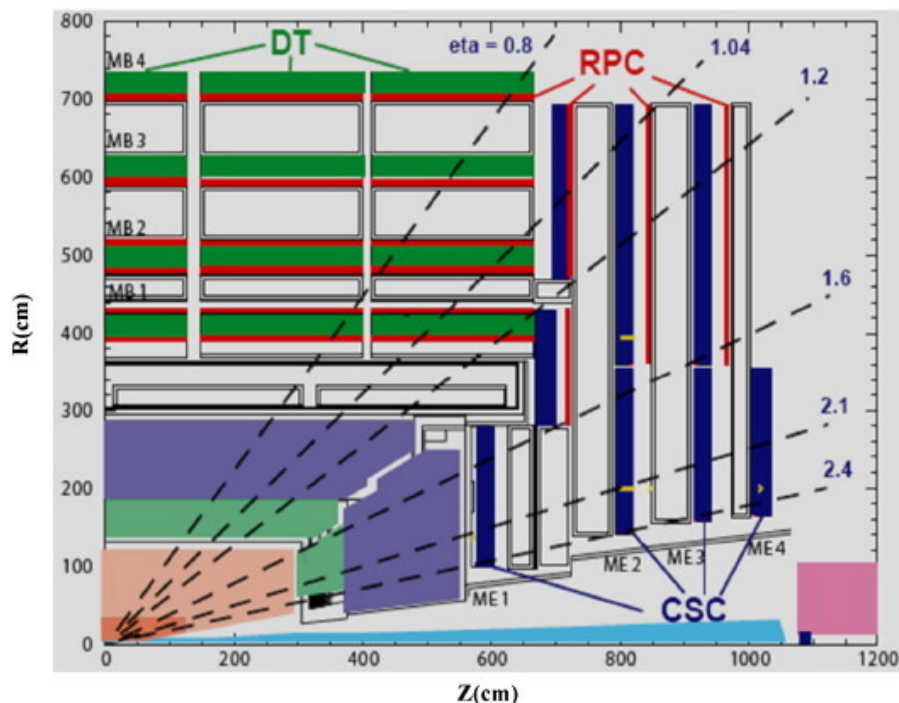


Figure 3.9.: CMS Muon system

Drift Tubes

In the central region of CMS, $|\eta| < 1.2$, the muon system consists of four concentric cylinders containing 250 gas drift chambers. Each Drift Tube is filled will a mix of 85% Argon and 15% CO₂ with active wires for charge collection. As muons pass through the gas they leave an ionization trail. The charge drifts to the wires, which detect the charge. The size of the drift cell was chosen so the maximum drift time is 380 ns. There are 172000 active wires in the entire system. The use of DTs is only possible in this region due its low magnetic field.

Cathode Strip Chambers

In the endcap, the muon system is comprised of Cathode Strip Chambers (CSC). The CSC's cover the $0.9 < |\eta| < 2.4$ pseudorapidity range. Each CSC is trapezoidal in shape and consists of 6 gas gaps, each gap having a plane of radial cathode strips and a plane of anode wires running almost perpendicularly to the strips. The CSC is a fast detector (response time of 4.5 ns), but with rather coarse position resolution; a precise position measurement is made by determining the centre-of-gravity of the charge distribution induced on the cathode strips (spatial resolution 200 μm , angular resolution 10 mrad).

Resistive Plate Chambers

In order to improve muon trigger system and for a good measurement of the bunch crossing time, resistive plate chambers (RPC) are mounted in the barrel and endcap region ($|\eta| < 1.6$). The RPCs are able to provide independent and fast trigger with high segmentation and sharp pT threshold over a large portion of the pseudorapidity range. However, the RPCs have coarser position resolution making them more useful for the trigger

3.3.5. Trigger and Data Acquisition

The CMS trigger system is designed to cope with an unprecedeted high luminosity and interactions rates. The LHC will collide proton bunches at a rate of 40 MHz which leads

to 10^9 interactions per second at design luminosity. Since it is not possible to record events at this rate, a two-part trigger system, consisting of a hardware-based trigger (Level 1) and a software-based trigger (High Level Trigger) is used [61, 62]. The rate is then reduced by a factor of 10^6 .

Level 1 Trigger

The Level 1 (L1) trigger is designed to achieve a maximum output rate of 100 kHz and consists of custom-designed, programmable electronics. The front-end (FE) electronics can store information from up to 128 consecutive events, which equates to $3 \mu\text{s}$. To cope with the time limitation, the L1 trigger system uses only coarsely segmented data from the muon system and the calorimeters while the full granularity data are stored in the FE electronics waiting for the L1 decision. The L1 muon trigger is organized into subsystems representing the three different muon detectors: the DT trigger in the barrel, the CSC trigger in the endcap and the RPC trigger covering both barrel and endcap. The Level-1 muon trigger also has the Global Muon Trigger (GMT) that combines the trigger information from the DT, CSC, and RPC muon subsystems, as well as from the calorimeter subsystem, and sends it to the Level-1 Global Trigger.

High Level Trigger

The High Level Trigger (HLT) exploits the full amount of collected data for each bunch crossing accepted by Level 1 Trigger and is capable of complex calculations such as the offline ones. It is structured in two levels, Level 2 (L2) and Level 3 (L3) implemented in software. The L2 uses information from the muon spectrometer (parameters from the L1 muon candidates converted into seeds) to perform a standalone reconstruction, providing a muon pT measurement with a precision of about 15 %. The L2 reconstruction follows closely the offline standalone reconstruction using Kalman-filter techniques. The L3 takes L2 candidates as seeds and adds information from the inner tracker by performing track reconstruction in the silicon tracker. This reconstruction is regional, it performs pattern recognition and track fitting only in a small $\eta - \phi$ slice of the tracker, to keep execution time low. Trajectories are then reconstructed using Kalman-filter techniques. Level 3 provides a much more precise p_T measurement (1% - 2% in the barrel region) than Level 2, as well as the ability to select on the basis of the track impact parameter with respect to the beam spot. After the HLT decisions, the event rate decreases down to 100Hz for mass storage which corresponds to a data rate of 150 Mbyte/s.

3.3.6. CMS data flow

Raw data that passed HLT and CMS Online Data Acquisition system (system which collects data from different detectors and builds events) is stored at a storage facility at CERN, known as Tier-0. The raw data contains information for every single proton-proton collision which passed HLT and it is called an event. There are about 10^9 events per year stored at Tier-0. Standard CMS algorithms perform calibration and alignment of the detector using raw data and do prompt (first) reconstruction of physics objects like muons, electrons, jets etc. Later, their momenta, energies and trajectories are measured and this is done by using all detectors of CMS experiment. The output data from prompt reconstruction is saved in different primary datasets based on trigger information. The data from Tier-0 is transferred to Tier-1 storage facilities worldwide where further calibration and re-reconstruction is performed centrally to be used by all CMS analyzes. The Tier-2 centers are more numerous and they are based at different universities in the world. They have limited disk space and are used for running individual analysis and Monte Carlo simulations. Data is stored in three types of root files which contain information about raw, reconstructed and analysis object data, respectively RAW, RECO and AOD root files. The RAW root files contain information about the recorded event in raw format as hits, energy deposits in the detector etc. The RECO root files contain detailed information of reconstructed physics objects and the AOD root files are simplified version of the RECO files which are mostly used in the analyses. Tier-0, Tier-1 and Tier-2 centers form a GRID [63] based computer infrastructure in 35 countries.

Chapter 4.

Υ production in Pb+Pb collisions

4.1. $\Upsilon(nS)$ in Pb+Pb collisions

At large energy densities and high temperatures, strongly interacting matter consists of a deconfined and chirally-symmetric system of quarks and gluons [64]. This state, often referred to as “quark-gluon plasma” (QGP) [65], constitutes the main object of the studies performed with relativistic heavy-ion collisions [66–69].

The formation of a QGP in high-energy nuclear collisions can be evidenced in a variety of ways. One of its most striking expected signatures is the suppression of quarkonium states [1], both of the charmonium (J/ψ , ψ' , χ_c , etc.) and the bottomonium ($\Upsilon(1S, 2S, 3S)$, χ_b , etc.) families. This is thought to be a direct effect of deconfinement, when the binding potential between the constituents of a quarkonium state, a heavy quark and its antiquark, is screened by the colour charges of the surrounding light quarks and gluons. The suppression is predicted to occur above the critical temperature of the medium (T_c) and depends on the $Q\bar{Q}$ binding energy. Since the $\Upsilon(1S)$ is the most tightly bound state among all quarkonia, it is expected to be the one with the highest dissociation temperature. Examples of dissociation temperatures are given in Ref. [70]: $T_{\text{dissoc}} \sim 1 T_c$, $1.2 T_c$, and $2 T_c$ for the $\Upsilon(3S)$, $\Upsilon(2S)$, and $\Upsilon(1S)$, respectively. Similarly, in the charmonium family the dissociation temperatures are $\leq 1 T_c$ and $1.2 T_c$ for the ψ' and J/ψ , respectively. However, there are further possible changes to the quarkonium production in heavy-ion collisions. On the one hand, modifications to the parton distribution functions inside the nucleus (shadowing) and other cold-nuclear-matter effects can reduce the production of quarkonia without the presence of a QGP [71, 72]. On the other hand, the large number of heavy quarks produced in heavy-ion collisions,

in particular at the energies accessible by the Large Hadron Collider (LHC), could lead to an increased production of quarkonia via statistical recombination [73–78].

Charmonium studies in heavy-ion collisions have been carried out for 25 years, first at the Super Proton Synchrotron (SPS) by the NA38 [79], NA50 [80, 81], and NA60 [82] fixed-target experiments at 17.3–19.3 GeV centre-of-mass energy per nucleon pair ($\sqrt{s_{NN}}$), and then at the Relativistic Heavy Ion Collider (RHIC) by the PHENIX experiment at $\sqrt{s_{NN}} = 200$ GeV [83]. In all cases, J/ψ suppression was observed in the most central collisions. At the SPS, the suppression of the ψ' meson was also measured [81]. Experimentally, the suppression is quantified by the ratio of the yield measured in heavy-ion collisions and a reference. At RHIC, the reference was provided by the properly scaled yield measured in pp collisions. Such a ratio is called the nuclear modification factor, R_{AA} . In the absence of modifications, one would expect $R_{AA} = 1$ for hard processes, which scale with the number of inelastic nucleon-nucleon collisions. For bottomonia, the production cross section is too small at RHIC to make definitive statements [84]. With the higher energy and luminosity available at the LHC, new studies for charmonia and bottomonia have become possible.

4.2. Data Selection

4.2.1. Event Selection

Inelastic hadronic PbPb collisions are selected using information from the BSC and HF calorimeters, in coincidence with a bunch crossing identified by the beam pick-up (one on each side of the interaction point) [85]. Events are further filtered offline by requiring a reconstructed primary vertex based on at least two tracks, and at least 3 towers on each HF with an energy deposit of more than 3 GeV per tower. These criteria reduce contributions from single-beam interactions with the environment (e.g. beam-gas collisions and collisions of the beam halo with the beam pipe), ultra-peripheral electromagnetic interactions, and cosmic-ray muons. A small fraction of the most peripheral PbPb collisions are not selected by these *minimum-bias* requirements, which accept $(97 \pm 3)\%$ of the inelastic hadronic cross section [86]. A sample corresponding to 55.7 M minimum-bias events passes all these filters. Assuming an inelastic PbPb cross section of $\sigma_{\text{PbPb}} = 7.65$ b [86], this sample corresponds to an integrated luminosity of

$\int L = 7.28 \mu\text{b}^{-1}$. This value is only mentioned for illustration purposes; the final results are normalized to the number of minimum-bias events.

The measurements reported here are based on dimuon events triggered by the L1 trigger, a hardware-based trigger that uses information from the muon detectors. The CMS detector is also equipped with a software-based high-level trigger (HLT). However, no further requirements at the HLT level have been applied to the L1 muon objects used for this analysis.

The event centrality distribution of minimum-bias events is compared to events selected by the double-muon trigger in Fig. 4.1. The centrality variable is defined as the fraction of the total cross section, starting at 0% for the most central collisions. This fraction is determined from the distribution of total energy measured in both HF calorimeters [87]. Using a Glauber-model calculation as described in Ref. [86], one can estimate variables related to the centrality, such as the number of nucleons participating in the collisions (N_{part}) and the nuclear overlap function (T_{AA}), which is equal to the number of elementary nucleon-nucleon (NN) binary collisions divided by the elementary NN cross section and can be interpreted as the NN equivalent integrated luminosity per heavy ion collision, at a given centrality [88]. The values of these variables are presented in Tab. 4.1 for the centrality bins used in this analysis. The double-muon-triggered events are more frequent in central collisions since the main physics processes that generate high- p_T muon pairs scale with the number of inelastic nucleon-nucleon collisions. In the following, N_{part} will be the variable used to show the centrality dependence of the measurements.

$\Upsilon(1S)$ Simulated MC events are used to tune the muon selection criteria, to compute the acceptance and efficiency corrections, and to obtain templates of the decay length distribution of J/ψ from b-hadron decays. For the acceptance corrections described in Section 4.4.1, three separate MC samples, generated over full phase space, are used: prompt J/ψ , J/ψ from b-hadron decays, and $\Upsilon(1S)$. Prompt J/ψ and $\Upsilon(1S)$ are produced using PYTHIA 6.424 [89] at $\sqrt{s} = 2.76\text{TeV}$, which generates events based on the leading-order colour-singlet and colour-octet mechanisms, with non-relativistic quantum chromodynamics (QCD) matrix elements tuned [90] by comparison with CDF data [91]. The colour-octet states undergo a shower evolution. For the non-prompt J/ψ studies, the b-hadron events are produced with PYTHIA in generic QCD 2→2 processes. In all three samples, the J/ψ or $\Upsilon(1S)$ decay is simulated using the EVTGEN [92] package. Prompt J/ψ and $\Upsilon(1S)$ are simulated assuming unpolarized production, while the non-prompt

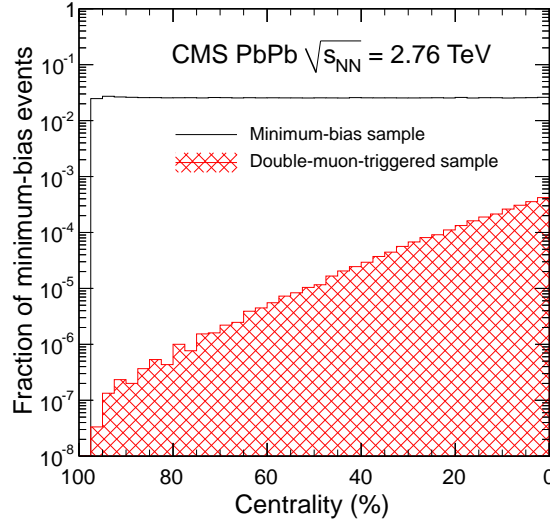


Figure 4.1.: Centrality distribution of the minimum-bias sample (solid black line) overlaid with the double-muon triggered sample (hashed red) in bins of 2.5%.

Table 4.1.: Average and root-mean-square (RMS) values of the number of participating nucleons (N_{part}) and of the nuclear overlap function (T_{AA}) for the centrality bins used in this analysis [86].

Centrality (%)	N_{part}		$T_{AA} (\text{mb}^{-1})$	
	Mean	RMS	Mean	RMS
0–10	355.4	33.3	23.19	3.77
10–20	261.4	30.4	14.48	2.86
20–30	187.2	23.4	8.78	1.94
30–40	130.0	17.9	5.09	1.27
40–50	86.3	13.6	2.75	0.80
50–100	22.1	19.3	0.47	0.54
0–20	308.4	56.8	18.83	5.49
20–100	64.2	63.0	2.37	3.05
0–100	113.1	115.6	5.66	7.54

J/ψ polarization is determined by the sum of the exclusive states generated by EVTGEN. Final-state bremsstrahlung is implemented using PHOTOS [93].

For some MC simulation studies, in particular the efficiency corrections described in Section 4.4.2, the detector response to each PYTHIA signal event is simulated with GEANT-4 [94] and then embedded in a realistic heavy-ion background event. The background events are produced with the HYDJET event generator [95] and then simulated with GEANT-4 as well. The HYDJET parameters were tuned to reproduce the particle multiplicities at all centralities seen in data. The embedding is done at the level of detector hits and requires that the signal and background production vertices match. The embedded event is then processed through the trigger emulation and the full event reconstruction chain. Collision data are used to validate the efficiencies evaluated using MC simulations, as discussed in Section 4.4.2.

4.2.2. Muon Selection

The muon offline reconstruction algorithm starts by reconstructing tracks in the muon detectors, called *standalone muons*. These tracks are then matched to tracks reconstructed in the silicon tracker by means of an algorithm optimized for the heavy-ion environment [96, 97]. The final muon objects, called *global muons*, result from a global fit of the standalone muon and tracker tracks. These are used to obtain the results presented in this paper.

In Fig. 4.2, the single-muon reconstruction efficiency from MC simulations is presented as a function of the muon p_T^μ and η^μ . The reconstruction efficiency is defined as the number of all reconstructed global muons divided by the number of generated muons in a given (η^μ, p_T^μ) bin. It takes into account detector resolution effects, i.e. reconstructed p_T and η values are used in the numerator and generated p_T and η values in the denominator. To obtain a clear separation between acceptance and efficiency corrections, a *detectable* single-muon acceptance is defined in the (η^μ, p_T^μ) space. For the J/ψ analysis this separation is defined by the contour that roughly matches a global muon reconstruction efficiency of 10%, indicated by the white lines superimposed in Fig. 4.2, which are described by the conditions

$$\begin{aligned}
 p_T^\mu &> 3.4 \text{GeV}/c & \text{for } |\eta^\mu| < 1.0, \\
 p_T^\mu &> (5.8 - 2.4 \times |\eta^\mu|) \text{GeV}/c & \text{for } 1.0 < |\eta^\mu| < 1.5, \\
 p_T^\mu &> (3.4 - 0.78 \times |\eta^\mu|) \text{GeV}/c & \text{for } 1.5 < |\eta^\mu| < 2.4.
 \end{aligned} \tag{4.1}$$

Muons failing these conditions are accounted for in the acceptance corrections discussed in Section 4.4.1. Muons that pass this acceptance requirement can still fail to pass the trigger, track reconstruction, or muon selection requirements. These losses are accounted for by the efficiency corrections discussed in Section 4.4.2.

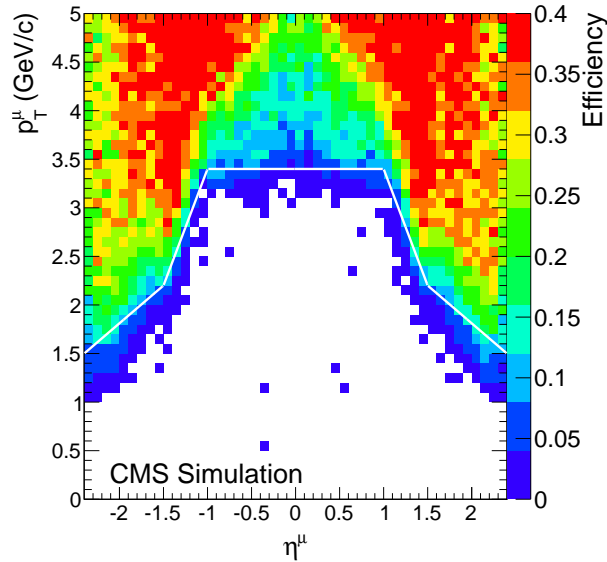


Figure 4.2.: Reconstruction efficiency of global muons in the (η^μ, p_T^μ) space, illustrating the lower limits (white lines) of what is considered a detectable single muon for the analysis.

For the $\Upsilon(1S)$ analysis, where the signal-to-background ratio is less favourable than in the J/ψ mass range, a higher p_T^μ is required than for the J/ψ analysis,

$$p_T^\mu > 4 \text{GeV}/c, \tag{4.2}$$

independent of η^μ .

Various additional global muon selection criteria are studied in MC simulations. The MC distributions of the J/ψ decay muons are in agreement with those from data to better than 2%, which is within the systematic uncertainty of the data/MC efficiency

ratio (Section 4.4.2). The transverse (longitudinal) distance of closest approach to the measured vertex is required to be less than 3 (15) cm. Tracks are only kept if they have 11 or more hits in the silicon tracker, and the χ^2 per degree of freedom of the global (inner) track fit is less than 20 (4). The χ^2 probability of the two tracks originating from a common vertex is required to be larger than 1%. From MC simulations we find that these criteria result in a 3.9% loss of $\Upsilon(1S)$ events, respectively, given two reconstructed tracks associated with the double muon trigger.

4.3. Signal Extraction

4.3.1. $\Upsilon(1S)$ Analysis

To extract the $\Upsilon(1S)$ yield, an extended unbinned maximum-likelihood fit to the $\mu^+\mu^-$ invariant mass spectrum between 7 and 14 GeV/c^2 is performed, integrated over p_T , rapidity, and centrality, as shown in the left panel of Fig. 4.3. The measured mass line shape of each Υ state is parametrised by a Crystal Ball function. Since the three Υ resonances partially overlap in the measured dimuon mass spectrum, they are fitted simultaneously. Therefore, the probability distribution function describing the signal consists of three Crystal Ball functions. In addition to the three $\Upsilon(nS)$ yields, the $\Upsilon(1S)$ mass is the only parameter left free, to accommodate a possible bias in the momentum scale calibration. The mass ratios between the states are fixed to their world average values [98], and the mass resolution is forced to scale linearly with the resonance mass. The $\Upsilon(1S)$ resolution is fixed to the value found in the simulation, 92 MeV/c^2 . This value is consistent with what is measured when leaving this parameter free in a fit to the data, $(122 \pm 30)\text{MeV}/c^2$. The low-side tail parameters in the Crystal Ball function are also fixed to the values obtained from simulation. Finally, a second-order polynomial is chosen to describe the background in the mass range 7–14 GeV/c^2 . From this fit, before accounting for acceptance and efficiencies, the measured $\Upsilon(1S)$ raw yield is 86 ± 12 . The observed suppression of the excited states was discussed in [99]. The fitted mean value is $m_0 = (9.441 \pm 0.016)\text{GeV}/c^2$, which is, slightly below the PDG value $m_{\Upsilon(1S)} = 9.460\text{GeV}/c^2$ [98] because of slight momentum scale biases in the data reconstruction.

The data are binned in p_T and rapidity of the $\mu^+\mu^-$ pairs, as well as in bins of the event centrality (0–10%, 10–20%, and 20–100%). The bins in rapidity are $|y| < 1.2$

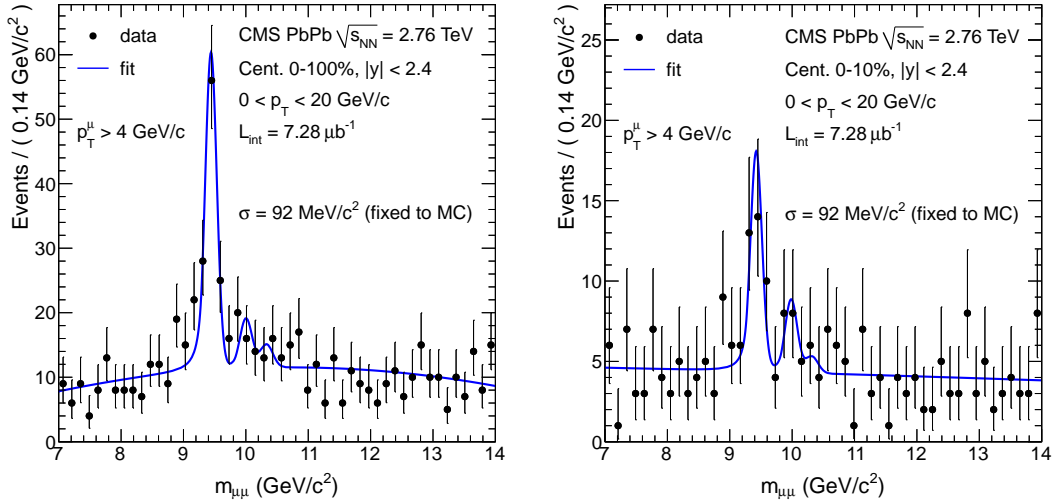


Figure 4.3.: Invariant-mass spectrum of $\mu^+\mu^-$ pairs (black circles) with $p_T < 20\text{GeV}/c$ and $|y| < 2.4$, for muons above $4\text{GeV}/c$, integrated over centrality (left) and for the 0–10% centrality bin (right).

and $1.2 < |y| < 2.4$. In contrast to the J/ψ case, CMS has acceptance for Υ down to $p_T = 0\text{GeV}/c$ over the full rapidity range. The p_T bins in this analysis are $0 < p_T < 6.5\text{GeV}/c$, $6.5 < p_T < 10\text{GeV}/c$, and $10 < p_T < 20\text{GeV}/c$. There are only two events with a $\mu^+\mu^-$ pair in the Υ mass region and $p_T > 20\text{GeV}/c$. The invariant-mass distribution for the centrality bin 0–10% is illustrated in the right panel of Fig. 4.3. The raw yields of $\Upsilon(1S)$ are tabulated in Tab. ?? of Appendix ??.

The systematic uncertainties are computed by varying the line shape in the following ways: (i) the Crystal Ball function tail parameters are varied randomly according to their covariance matrix and within conservative values covering imperfect knowledge of the amount of detector material and final-state radiation in the underlying process; (ii) the width is varied by $\pm 5\text{MeV}/c^2$, a value motivated by the current understanding of the detector performance (eg., the dimuon mass resolution, accurately measured at the J/ψ mass, is identical in pp and PbPb collisions); (iii) the background shape is changed from quadratic to linear, and the mass range of the fit is varied from 6–15 to 8–12 GeV/c^2 ; the observed RMS of the results in each category is taken as the systematic uncertainty. The quadratic sum of these three systematic uncertainties is dominated by the variation of the resolution of the mass fit, and is of the order of 10%, reaching 13% for the 0–10% centrality bin. As was the case for the J/ψ selection, a simple counting of the yield in the signal region after the subtraction of the same-sign spectrum leads to consistent results.

4.4. Acceptance and Efficiency

4.4.1. Acceptance

The dimuon acceptance, A , is defined as the fraction of $\mu^+\mu^-$ pairs for which both muons are declared detectable in the CMS detector with respect to all muon pairs produced in $|y| < 2.4$,

$$A(p_T, y; \lambda_\theta) = \frac{N_{\text{detectable}}^{\mu\mu}(p_T, y; \lambda_\theta)}{N_{\text{generated}}^{\mu\mu}(p_T, y; \lambda_\theta)}, \quad (4.3)$$

where:

- $N_{\text{detectable}}^{\mu\mu}$ is the number of generated events in a given quarkonium (p_T, y) bin in the MC simulation, for which both muons are detectable according to the selections defined in Eqs. (4.1) and (4.2);
- $N_{\text{generated}}^{\mu\mu}$ is the number of all $\mu^+\mu^-$ pairs generated within the considered (p_T, y) bin.

The acceptance depends on the p_T and y of the $\mu^+\mu^-$ pair, and the polarization parameter λ_θ . Different polarizations of the J/ψ and $\Upsilon(1S)$ will cause different single-muon angular distributions in the laboratory frame and, hence, different probabilities for the muons to fall inside the CMS detector acceptance. Since the quarkonium polarization has not been measured in heavy-ion or pp collisions at $\sqrt{s_{NN}} = 2.76\text{TeV}$, the prompt J/ψ and $\Upsilon(1S)$ results are quoted for the unpolarized scenario only. For non-prompt J/ψ the results are reported for the polarization predicted by EVTGEN. The impact of the polarization on the acceptance is studied for the most extreme polarization scenarios in the Collins–Soper and helicity frames. For fully longitudinal (transverse) polarized J/ψ in the Collins–Soper frame, the effect is found to be at most -20% (6%). In the helicity frame, the effects are at most 40% and -20% for the two scenarios. For $\Upsilon(1S)$ the polarization effects range between -20% for longitudinal polarization in the Collins–Soper frame to 40% for transverse polarization in the helicity frame. The acceptance is calculated using the MC sample described in Section 4.2.1. The p_T and rapidity dependencies of the J/ψ and $\Upsilon(1S)$ acceptances are shown in Fig. 4.4.

Since the acceptance is a function of both p_T and y , uncertainties in the predicted distributions for these variables can lead to a systematic uncertainty in the average acceptance over a p_T or y bin. To estimate these uncertainties, the shapes of the

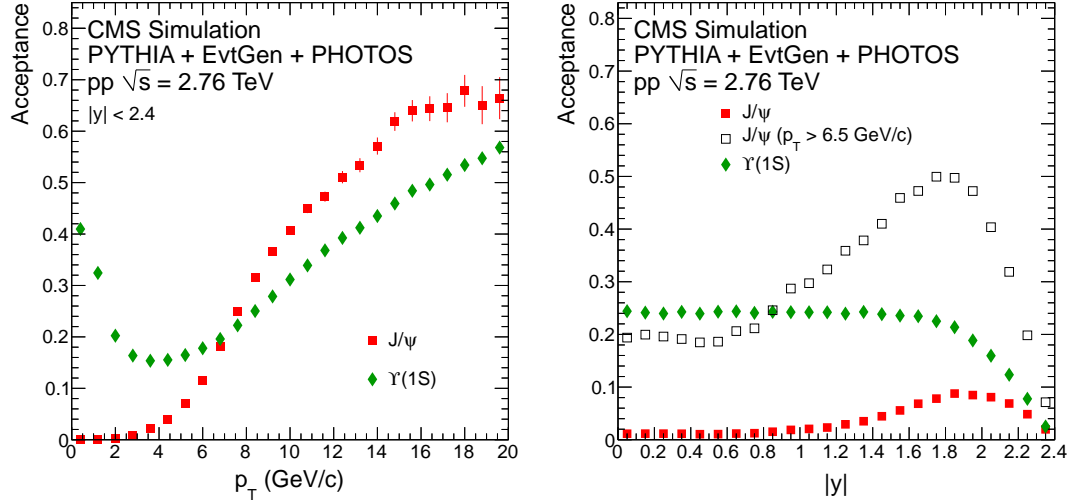


Figure 4.4.: Dimuon acceptance as a function of p_T (left) and $|y|$ (right) for J/ψ (red squares) and $\Upsilon(1S)$ (green diamonds). Also shown in the right panel is the acceptance for J/ψ with $p_T > 6.5\text{GeV}/c$ (open black squares). The error bars represent the statistical uncertainties only.

generated MC p_T and $|y|$ distributions are varied by applying a weight that increases linearly from 0.7 to 1.3 over the range $0 < |y| < 2.4$ and $0 < p_T < 30\text{GeV}/c$ ($20\text{GeV}/c$) for J/ψ ($\Upsilon(1S)$). The RMS of the resulting changes in the acceptance for each p_T and y bin are summed in quadrature to compute the overall systematic uncertainty from this source. The largest relative systematic uncertainties obtained are 4.2%, 3.2%, and 2.8% for the prompt J/ψ , non-prompt J/ψ , and $\Upsilon(1S)$ acceptances, respectively.

4.4.2. Efficiency

The trigger, reconstruction, and selection efficiencies of $\mu^+\mu^-$ pairs are evaluated using simulated MC signal events embedded in simulated PbPb events, as described in Section 4.2.1. The overall efficiency is calculated, in each analysis bin, as the fraction of generated events (passing the single muon phase space cuts) where both muons are reconstructed, fulfil the quality selection criteria and pass the trigger requirements. In the embedded sample, the signal over background ratio is by construction higher than in data, so the background contribution underneath the resonance peak is negligible and the signal is extracted by simply counting the $\mu^+\mu^-$ pairs in the quarkonium mass region. The counting method is crosschecked by using exactly the same fitting procedure as if the MC events were collision data. Only muons in the kinematic region defined by Eqs. (4.1) and (4.2) are considered. In Fig. 4.5, the efficiencies are shown as a function

of the $\mu^+\mu^-$ pair p_T , y , and the event centrality, for each signal: red squares for prompt J/ψ , orange stars for non-prompt J/ψ , and green diamonds for $\Upsilon(1S)$. The efficiency of non-prompt J/ψ is lower than that of prompt J/ψ , reaching about 35% for $p_T > 12\text{GeV}/c$. The prompt J/ψ efficiency increases with p_T until reaching a plateau slightly above 50% at p_T of about $12\text{GeV}/c$, while the $\Upsilon(1S)$ efficiency is $\sim 55\%$, independent of p_T . The efficiencies decrease slowly as a function of centrality because of the increasing occupancy in the silicon tracker; the relative difference between peripheral and central collisions is 17% for J/ψ and 10% for $\Upsilon(1S)$. The integrated efficiency values are 38.3%, 29.2%, and 54.5% for the prompt J/ψ , non-prompt J/ψ (both with $6.5 < p_T < 30\text{GeV}/c$, $|y| < 2.4$, and 0–100% centrality), and $\Upsilon(1S)$ (with $0 < p_T < 20\text{GeV}/c$, $|y| < 2.4$, and 0–100% centrality), respectively.

The systematic uncertainty on the final corrections due to the kinematic distributions is estimated by a $\pm 30\%$ variation of the slopes of the generated p_T and rapidity shapes, similar to the acceptance variation described in the previous section. The systematic uncertainties are in the ranges 1.8–3.4%, 2.2–4.2%, and 1.4–2.7% for prompt J/ψ , non-prompt J/ψ , and $\Upsilon(1S)$, respectively, including the statistical precision of the MC samples. The individual components of the MC efficiency are crosschecked using muons from J/ψ decays in simulated and collision data with a technique called *tag-and-probe*, similar to the one used for the corresponding pp measurement [100].

4.5. The pp Baseline Measurement

A pp run at $\sqrt{s} = 2.76\text{TeV}$ was taken in March 2011. The integrated luminosity was 231 nb^{-1} , with an associated uncertainty of 6%. For hard-scattering processes, the integrated luminosity of the pp sample is comparable to that of the PbPb sample ($7.28\mu b^{-1} \cdot 208^2 \approx 315nb^{-1}$).

Given the higher instantaneous luminosity, the trigger required slightly higher quality muons in the pp run than in the PbPb run. The offline event selection is the same as in the PbPb analysis, only slightly relaxed for the HF coincidence requirement: instead of three towers, only one tower with at least 3 GeV deposited is required in the pp case. The same reconstruction algorithm, i.e. the one optimized for the heavy-ion environment, is used for both pp and PbPb data. The products of the trigger, reconstruction, and selection efficiencies determined in pp MC simulations are 42.5%, 34.5%, and 55.1% for the prompt J/ψ , non-prompt J/ψ (both with $6.5 < p_T < 30\text{GeV}/c$, $|y| < 2.4$), and $\Upsilon(1S)$

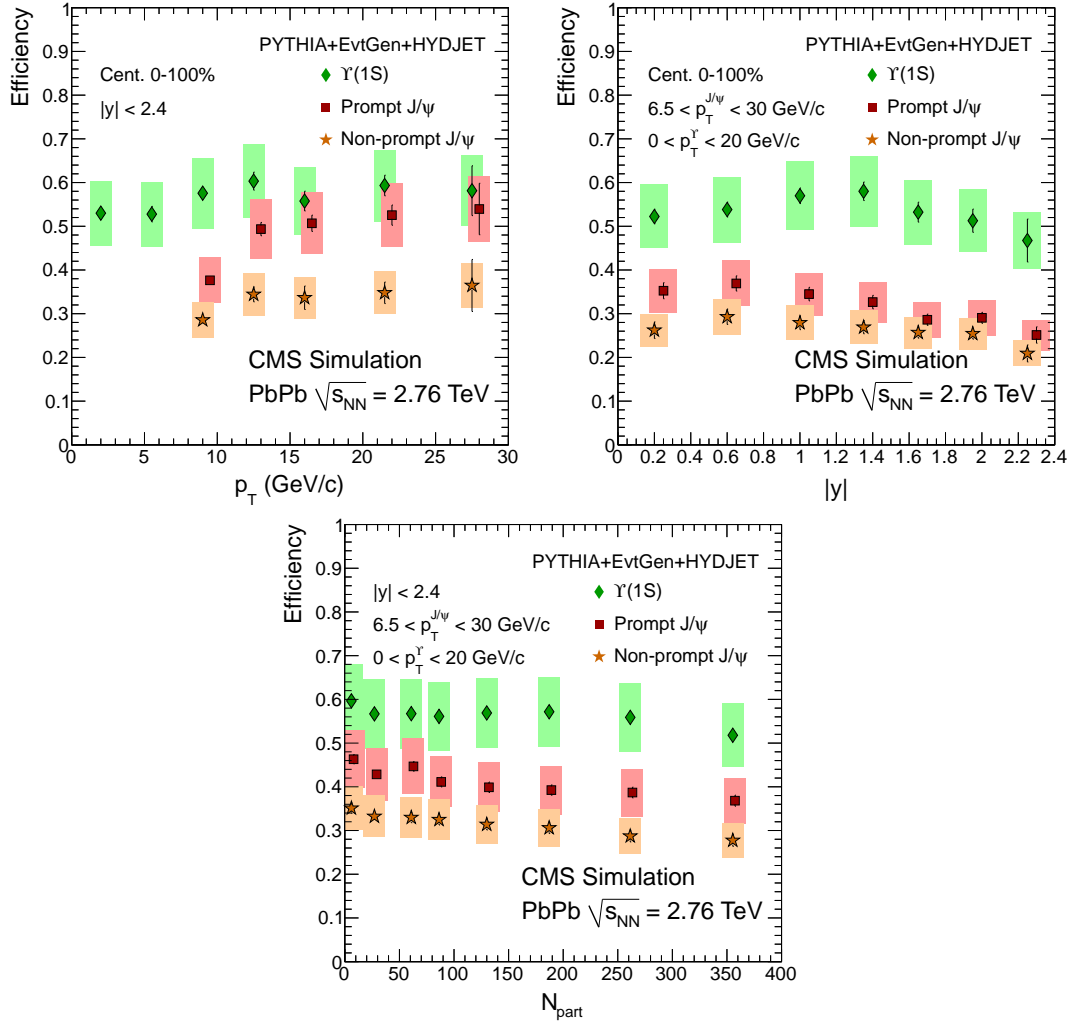


Figure 4.5.: Combined trigger, reconstruction, and selection efficiencies as a function of quarkonium p_T and $|y|$, and event centrality, for each signal: red squares and orange stars for prompt and non-prompt J/ψ , respectively, and green diamonds for $\Upsilon(1S)$. For better visibility, the prompt J/ψ points are shifted by $\Delta p_T = 0.5 \text{ GeV}/c$, $\Delta y = 0.05$, and $\Delta N_{\text{part}} = 2$. Statistical (systematic) uncertainties are shown as bars (boxes). The systematic uncertainties are the quadratic sum of the uncertainty on the kinematic distributions and the MC validation uncertainty.

(with $0 < p_T < 20 \text{ GeV}/c$, $|y| < 2.4$), respectively. The quarkonium signals in pp collisions are extracted following the same methods as in PbPb collisions.

The invariant-mass spectrum of $\mu^+\mu^-$ pairs in the Υ region from pp collisions is shown in Fig. 4.6. The same procedure as the one described for the PbPb analysis is used. The number of $\Upsilon(1S)$ mesons with $|y| < 2.4$ and $0 < p_T < 20 \text{ GeV}/c$ is 101 ± 12 . The fit result of the excited states is discussed in [99].

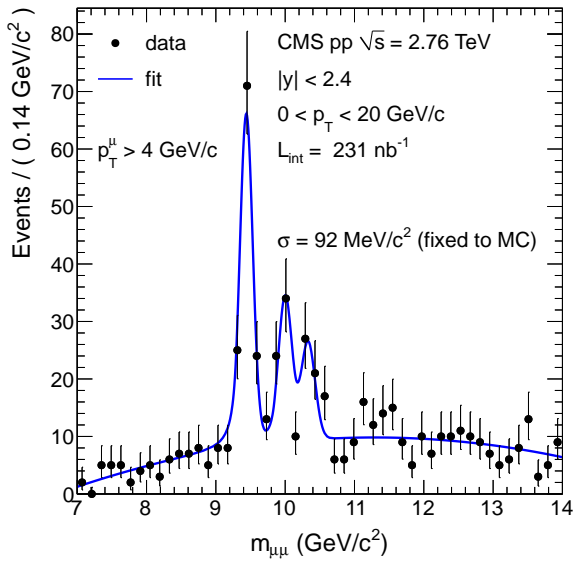


Figure 4.6.: The pp dimuon invariant-mass distribution in the range $p_T < 20 \text{ GeV}/c$ for $|y| < 2.4$ and the result of the fit to the Υ resonances.

For the measurement of the nuclear modification factors, in which the ratio of PbPb to pp results is computed, most of the reconstruction systematic uncertainties cancel out because the same algorithm is used. However, the following factors must be accounted for:

1. The luminosity uncertainty. This is a global systematic uncertainty of 6% that allows all measured nuclear modification factors to change by a common scale-factor. Since the PbPb yield is normalized by the number of minimum-bias events, which has a negligible uncertainty, no systematic uncertainty on the PbPb luminosity has to be considered.
2. The uncertainty on T_{AA} . For results integrated over centrality, this is a global systematic uncertainty of 5.7%, based on the Glauber model employed. For results as a function of centrality, the uncertainty varies between a minimum of 4.3% in the most central bin and a maximum of 15% in the most peripheral bin [86].

3. The systematic uncertainty associated with the trigger efficiency. The ratios between the *tag-and-probe* efficiencies obtained in pp and PbPb are the same in data and MC events, within the statistical accuracy of the data (1% for the single-muon efficiency). Twice this value (2%) is assigned as the uncertainty on the difference of the trigger efficiencies of $\mu^+\mu^-$ pairs in PbPb and pp collisions.
4. The tracking efficiency uncertainty due to different charged particle multiplicities in pp and PbPb collisions. The ratios between the *tag-and-probe* efficiencies obtained in pp and central PbPb events are the same in data and MC events, within the statistical accuracy of the data (6.8% for the single-muon efficiency). This value is propagated as the tracking systematic uncertainty in all the ratios of PbPb to pp data.

4.6. Results

The double-differential quarkonium cross sections in PbPb collisions are reported in the form

$$\frac{1}{T_{AA}} \cdot \frac{d^2N}{dy dp_T} = \frac{1}{T_{AA} N_{MB}} \cdot \frac{1}{\Delta y \Delta p_T} \cdot \frac{N_{Q\bar{Q}}}{A \varepsilon}, \quad (4.4)$$

while in pp collisions they are calculated as

$$\frac{d^2\sigma}{dy dp_T} = \frac{1}{L_{pp}} \cdot \frac{1}{\Delta y \Delta p_T} \cdot \frac{N_{Q\bar{Q}}}{A \varepsilon}, \quad (4.5)$$

where:

- $N_{Q\bar{Q}}$ is the number of measured $\Upsilon(1S)$ in the $\mu^+\mu^-$ decay channel;
- N_{MB} is the number of minimum-bias events sampled by the event selection; when binned in centrality, only the fraction of minimum-bias events in that centrality bin is considered;
- A is the geometric acceptance, which depends on the p_T and y of the quarkonium state;
- ε is the combined trigger and reconstruction efficiency, which depends on the p_T and y of the quarkonium state and on the centrality of the collision;

- Δy and Δp_T are the bin widths in rapidity and p_T , respectively;
- T_{AA} is the nuclear overlap function, which depends on the collision centrality;
- $L_{pp} = (231 \pm 14)\text{nb}^{-1}$ is the integrated luminosity of the pp data set.

Following Eq. (4.4), the uncorrected yields of $\Upsilon(1S)$, measured in PbPb collisions are corrected for acceptance and efficiency (reported in Figs. 4.4 and 4.5), and converted into yields divided by the nuclear overlap function T_{AA} . These quantities can be directly compared to cross sections in pp collisions measured from the raw yields according to Eq. (4.5). The rapidity and centrality-dependent results are presented integrated over p_T . All results are presented for the unpolarized scenario and are tabulated in Tables ??–?? of Appendix ??.

The systematic uncertainties detailed in the previous sections are summarized in Tables 4.2 and 4.3. The relative uncertainties for all terms appearing in Eqs. (4.4) and (4.5) are added in quadrature, leading to a total of 15–21% on the corrected yields. For results plotted as a function of p_T or rapidity, the systematic uncertainty on T_{AA} enters as a global uncertainty on the scale and is not included in the systematic uncertainties of the yields. As a function of centrality, the uncertainty on T_{AA} varies point-to-point and is included in the systematic uncertainties of the yields.

Table 4.2.: Point-to-point systematic uncertainties on the prompt J/ψ , non-prompt J/ψ , and $\Upsilon(1S)$ yields measured in PbPb collisions.

	prompt J/ψ (%)	non-prompt J/ψ (%)	$\Upsilon(1S)$ (%)
Yield extraction	0.5–5.7	1.5–14.0	8.7–13.4
Efficiency	1.8–3.4	2.2–4.2	1.4–2.7
Acceptance	0.9–4.2	2.0–3.2	1.5–2.8
MC Validation	13.7	13.7	13.7
Stand-alone μ reco.	1.0	1.0	1.0
T_{AA}	4.3–15.0	4.6–8.6	4.3–8.6
Total	15–21	15–21	18–20

The nuclear modification factor,

$$R_{AA} = \frac{L_{pp}}{T_{AA} N_{MB}} \frac{N_{\text{PbPb}}(Q\bar{Q})}{N_{pp}(Q\bar{Q})} \cdot \frac{\varepsilon_{pp}}{\varepsilon_{\text{PbPb}}}, \quad (4.6)$$

Table 4.3.: Point-to-point systematic uncertainties on the prompt J/ψ , non-prompt J/ψ , and $\Upsilon(1S)$ yields measured in pp collisions.

	prompt J/ψ (%)	non-prompt J/ψ (%)	$\Upsilon(1S)$ (%)
Yield extraction	0.8–5.3	5.3–16.8	10.0
Efficiency	1.6–3.0	1.4–2.0	0.4–0.9
Acceptance	0.9–4.2	2.0–3.2	1.5–2.8
MC Validation	13.7	13.7	13.7
Stand-alone μ reco.	1.0	1.0	1.0
Total	14–16	15–22	17–18

is calculated from the raw yields $N_{\text{PbPb}}(Q\bar{Q})$ and $N_{pp}(Q\bar{Q})$, correcting only for the multiplicity-dependent fraction of the efficiency ($\frac{\varepsilon_{pp}}{\varepsilon_{\text{PbPb}}} \sim 1.16$ for the most central bin); the p_T and rapidity dependencies of the efficiency cancel in the ratio. These results are also tabulated in Appendix ???. It should be noted that the R_{AA} would be sensitive to changes of the J/ψ polarization between pp and PbPb collisions, an interesting physics effect on its own [101].

In all figures showing results, statistical uncertainties are represented by error bars and systematic uncertainties by boxes. Results as a function of rapidity are averaged over the positive and negative rapidity regions.

4.6.1. $\Upsilon(1S)$

In Fig. 4.7, the $\Upsilon(1S)$ yield divided by T_{AA} in PbPb collisions and its cross section in pp collisions are shown as a function of p_T ; the R_{AA} of $\Upsilon(1S)$ is displayed in the right panel of Fig. 4.7. The p_T dependence shows a significant suppression, by a factor of ~ 2.3 at low p_T , that disappears for $p_T > 6.5\text{GeV}/c$. The rapidity dependence indicates a slightly smaller suppression at forward rapidity, as shown in Fig. 4.8. However, the statistical uncertainties are too large to draw strong conclusions on any p_T or rapidity dependence. The $\Upsilon(1S)$ yield in PbPb collisions divided by T_{AA} and the $\Upsilon(1S)$ R_{AA} are presented as a function of N_{part} in the left and right panels of Fig. 4.9, respectively. Within uncertainties, no centrality dependence of the $\Upsilon(1S)$ suppression is observed.

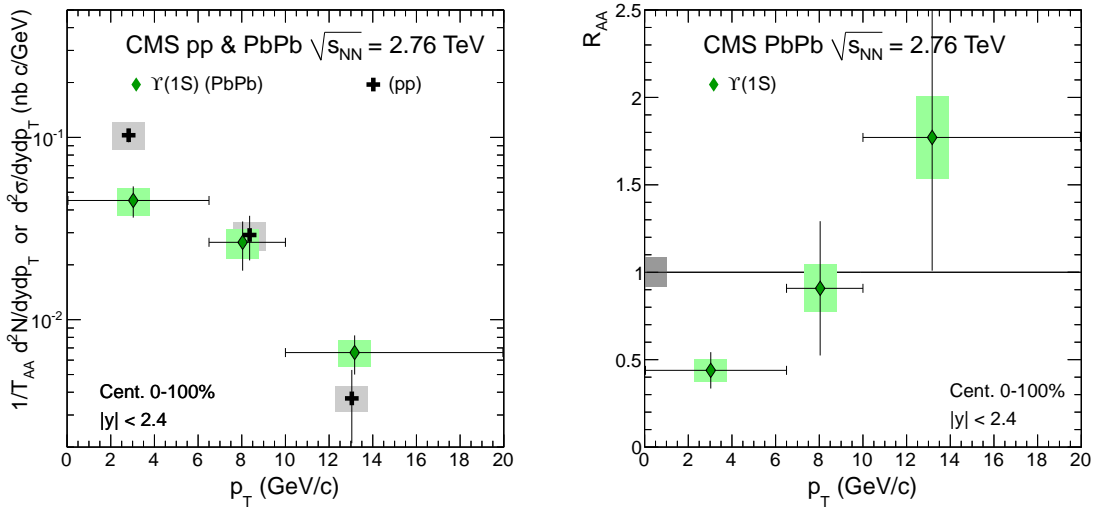


Figure 4.7.: Left: $\Upsilon(1S)$ yield divided by T_{AA} in PbPb collisions (green diamonds) as a function of p_T . The result is compared to the cross section measured in pp collisions (black crosses). The global scale uncertainties on the PbPb data due to T_{AA} (5.7%) and the pp integrated luminosity (6.0%) are not shown. Right: nuclear modification factor R_{AA} of $\Upsilon(1S)$ as a function of p_T . A global uncertainty of 8.3%, from T_{AA} and the integrated luminosity of the pp data sample, is shown as a grey box at $R_{AA} = 1$. Points are plotted at their measured average p_T . Statistical (systematic) uncertainties are shown as bars (boxes). Horizontal bars indicate the bin width.

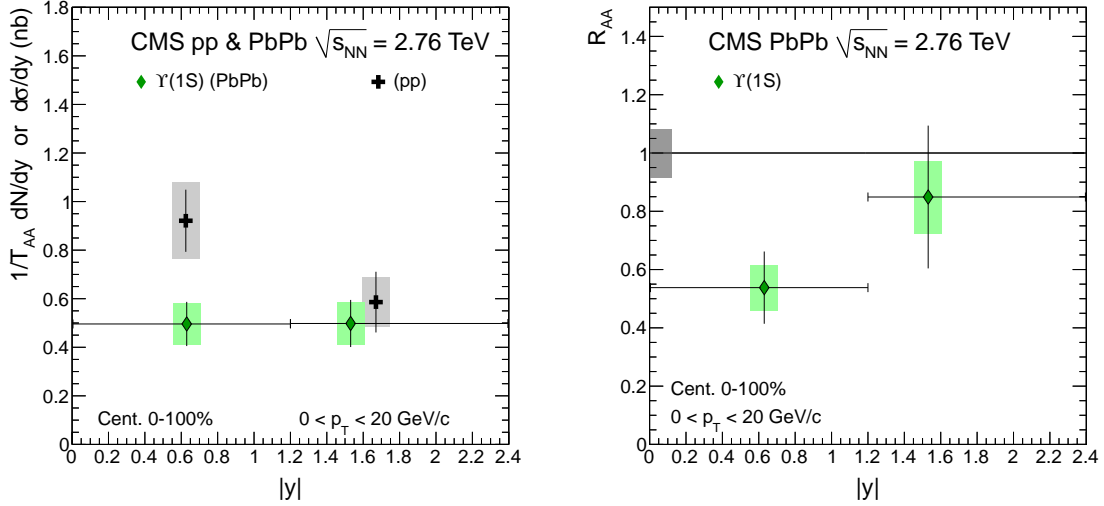


Figure 4.8.: Left: $\Upsilon(1S)$ yield divided by T_{AA} in $PbPb$ collisions (green diamonds) as a function of rapidity. The result is compared to the cross section measured in pp collisions (black crosses). The global scale uncertainties on the $PbPb$ data due to T_{AA} (5.7%) and the pp integrated luminosity (6.0%) are not shown. Right: nuclear modification factor R_{AA} of $\Upsilon(1S)$ as a function of rapidity. A global uncertainty of 8.3%, from T_{AA} and the integrated luminosity of the pp data sample, is shown as a grey box at $R_{AA} = 1$. Points are plotted at their measured average $|y|$. Statistical (systematic) uncertainties are shown as bars (boxes). Horizontal bars indicate the bin width.

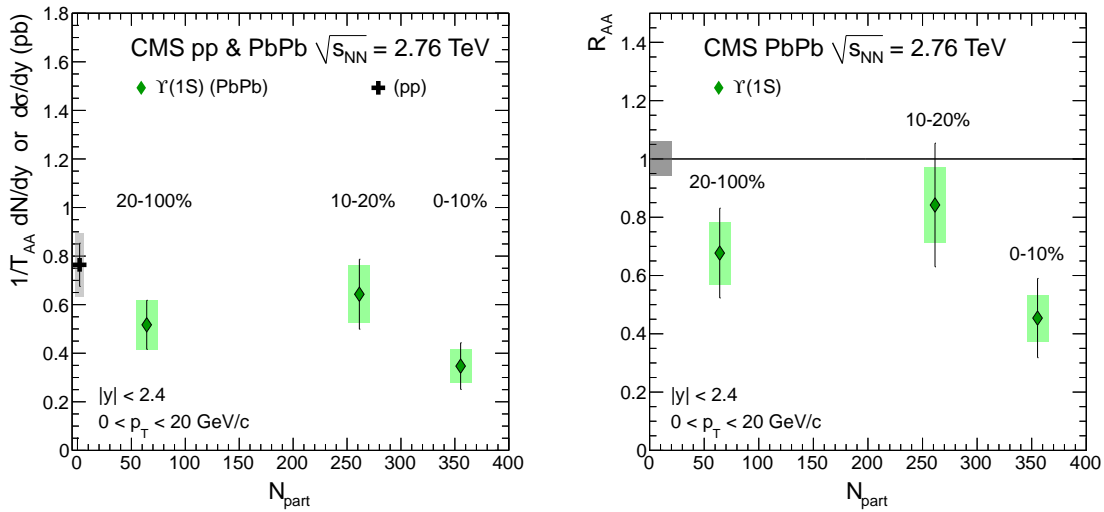


Figure 4.9.: Left: $\Upsilon(1S)$ yield divided by T_{AA} (green diamonds) as a function of N_{part} compared to the $\Upsilon(1S)$ cross section measured in pp (black cross). Right: nuclear modification factor R_{AA} of $\Upsilon(1S)$ as a function of N_{part} . A global uncertainty of 6%, from the integrated luminosity of the pp data sample, is shown as a grey box at $R_{AA} = 1$. Statistical (systematic) uncertainties are shown as bars (boxes).

4.7. Indication of suppression of excited Υ states in PbPb collisions at $\sqrt{s_{\text{NN}}} = 2.76 \text{ TeV}$

A comparison of the relative yields of Υ resonances in the $\mu^+\mu^-$ decay channel in PbPb and pp collisions at a centre-of-mass energy per nucleon pair of 2.76 TeV, is performed with data collected with the CMS detector at the LHC. Using muons of transverse momentum above $4 \text{ GeV}/c$ and pseudorapidity below 2.4, the double ratio of the $\Upsilon(2S)$ and $\Upsilon(3S)$ excited states to the $\Upsilon(1S)$ ground state in PbPb and pp collisions, $[\Upsilon(2S + 3S)/\Upsilon(1S)]_{\text{PbPb}}/[\Upsilon(2S + 3S)/\Upsilon(1S)]_{\text{pp}}$, is found to be $0.31^{+0.19}_{-0.15} \text{ (stat.)} \pm 0.03 \text{ (syst.)}$. The probability to obtain the measured value, or lower, if the true double ratio is unity, is calculated to be less than 1%. The measurement is performed with the data recorded by the Compact Muon Solenoid (CMS) experiment during the first PbPb LHC run, at the end of 2010, and during the pp run of March 2011, both at $\sqrt{s_{\text{NN}}} = 2.76 \text{ TeV}$. The integrated luminosity used in this analysis corresponds to $7.28 \mu\text{b}^{-1}$ for PbPb and 225 nb^{-1} for pp collisions, the latter corresponding approximately to the equivalent nucleon-nucleon luminosity of the PbPb run. The excellent momentum resolution of the CMS detector results in well-resolved Υ peaks in the dimuon mass spectrum.

A detailed description of the CMS detector can be found in 4.7. Its central feature is a superconducting solenoid of 6 m internal diameter, providing a magnetic field of 3.8 T. Within the field volume are the silicon pixel and strip tracker, the crystal electromagnetic calorimeter, and the brass/scintillator hadron calorimeter. Muons are measured in gas-ionisation detectors embedded in the steel return yoke. In addition, CMS has extensive forward calorimetry, in particular two steel/quartz-fiber Cerenkov hadron forward (HF) calorimeters, which cover the pseudorapidity range $2.9 < |\eta| < 5.2$.

In this analysis, Υ mesons are identified through their dimuon decay. The silicon pixel and strip tracker measures charged-particle trajectories in the range $|\eta| < 2.5$. The tracker consists of 66M pixel and 10M strip detector channels, providing a vertex resolution of $\sim 15 \mu\text{m}$ in the transverse plane. Muons are detected in the $|\eta| < 2.4$ range, with detection planes based on three technologies: drift tubes, cathode strip chambers, and resistive plate chambers. Due to the strong magnetic field and the fine granularity of the silicon tracker, the muon transverse momentum measurement (p_{T}) based on information from the silicon tracker alone has a resolution between 1 and 2% for a typical muon in this analysis.

In both the PbPb and pp runs, the events are selected by the CMS two-level trigger. At the first, hardware level, two independent muon candidates are required in the muon detectors. No selection is made on momentum or pseudorapidity, but in the pp case more stringent quality requirements are imposed for each muon in order to reduce the higher trigger rate. In both cases, the software-based higher-level trigger accepts the lower-level decision without applying further criteria. From reconstructed $J/\psi \rightarrow \mu\mu$ decays, the single-muon trigger efficiencies are measured and found to be consistent between the PbPb, $(96.1 \pm 1.0)\%$, and the pp, $(95.5 \pm 0.6)\%$, data sets, for muons with $p_T > 4 \text{ GeV}/c$.

In the PbPb data, events are preselected offline if they contain a reconstructed primary vertex made of at least two tracks, and a coincidence in both HF calorimeters of energy deposits in at least three towers of 3 GeV each. These criteria reduce contributions from single-beam interactions (e.g. beam-gas and beam-halo collisions with the beam pipe), ultra-peripheral electromagnetic collisions, and cosmic-ray muons. A small fraction of the most peripheral PbPb collisions is not selected by these requirements, which accept $(97 \pm 3)\%$ of the hadronic inelastic cross section. For the pp run, a similar event filter is applied, relaxing the HF coincidence to one tower in each HF, with at least 3 GeV deposited. This filter removes only 1% of the pp events satisfying the dimuon trigger.

The muon offline reconstruction is seeded with $\simeq 99\%$ efficiency by tracks in the muon detectors, called standalone muons. These tracks are then matched to tracks reconstructed in the silicon tracker by means of an algorithm optimised for the heavy-ion environment [96, 97]. For muons from Υ decays the tracking efficiency is $\simeq 85\%$. This efficiency is lower than in pp, as in PbPb the track reconstruction is seeded by a greater number of pixel hits to reduce the large number of random combinations arising from the high multiplicity of each event. Combined fits of the muon and tracker tracks are used to obtain the results presented in this section. The heavy-ion dedicated reconstruction algorithm is applied to the pp data in order to avoid potential biases, arising from different tracking efficiencies of the two reconstruction algorithms, when comparing the two data sets.

Identical very loose selection criteria are applied to the muons in the pp and PbPb data. The transverse (longitudinal) distance from the event vertex is required to be less than 3 (15) cm. Tracks are only kept if they have 11 or more hits in the silicon tracker and the χ^2 per degree of freedom of the combined (tracker) track fit is lower than 20 (4). The two muon trajectories are fit with a common vertex constraint, and events are retained if the fit χ^2 probability is larger than 1%. This removes background arising primarily from displaced heavy quark semileptonic decays. As determined from Monte

Carlo simulation of the $\Upsilon(1S)$ signal, these selection criteria are found to reduce the efficiency by 3.9%, consistent with the signal loss observed in both pp and PbPb data. The available event sample limits to 20 GeV/c the dimuon transverse momentum range probed in this study.

In order to further reduce the background in the Υ mass region, only muons with a transverse momentum (p_T^μ) higher than 4 GeV/c are considered, resulting in a Υ acceptance of approximately 25% for the $|y^\Upsilon| < 2.4$ rapidity range. This requirement improves the significance of the $\Upsilon(1S)$ signal in PbPb data and is applied to both data sets. The acceptance of a Υ state depends on its mass, since the excited states give rise to higher-momenta muons. In consequence, requiring higher p_T^μ increases the acceptance for the excited states relative to the ground state. In the corresponding analysis performed with the higher-statistics (3.1 pb^{-1}) 7 TeV data [103], looser criteria were applied ($p_T^\mu > 3.5 \text{ GeV}/c$ and $|\eta^\mu| < 1.6$, or $p_T^\mu > 2.5 \text{ GeV}/c$ and $1.6 < |\eta^\mu| < 2.4$), where η^μ is the muon pseudorapidity. The stricter ($p_T^\mu > 4 \text{ GeV}/c$) requirements used here enhance the $\Upsilon(2S + 3S)/\Upsilon(1S)$ yield ratio by $\simeq 60\%$ in the p p data at 2.76 TeV. It was checked that, applying the same reconstruction algorithm and the same p_T^μ requirements, the $\Upsilon(2S + 3S)/\Upsilon(1S)$ yield ratio is consistent between the 2.76 and 7 TeV pp data sets. The dimuon invariant mass spectra with the selection criteria applied are shown in Fig. 4.10 for the pp and PbPb data sets. Within the 7–14 GeV/c^2 mass range, there are 561 (628) opposite-sign muon pairs in the pp (PbPb) data set. The three Υ peaks are clearly observed in the pp case, but the $\Upsilon(2S)$ and $\Upsilon(3S)$ are barely visible over the residual background in PbPb collisions.

An extended unbinned maximum likelihood fit to the two invariant mass distributions of Fig. ?? is performed to extract the yields, following the method described in [103]. The measured mass lineshape of each Υ state is parameterised by a “Crystal Ball” (CB) function, i.e. a Gaussian resolution function with the low-side tail replaced by a power law describing final state radiation (FSR). Since the three Υ resonances partially overlap in the measured dimuon mass, they are fit simultaneously. Therefore, the probability distribution function (PDF) describing the signal consists of three CB functions. In addition to the three $\Upsilon(nS)$ yields, the $\Upsilon(1S)$ mass is the only parameter left free, to accommodate a possible bias in the momentum scale calibration. The mass differences between the states are fixed to their world average values [98] and the mass resolution is forced to scale with the resonance mass. The $\Upsilon(1S)$ resolution is fixed to the value estimated in the simulation, 92 MeV/c^2 , which is compatible with the resolution obtained from both the PbPb and pp data. The low-side tail parameters are also fixed to the

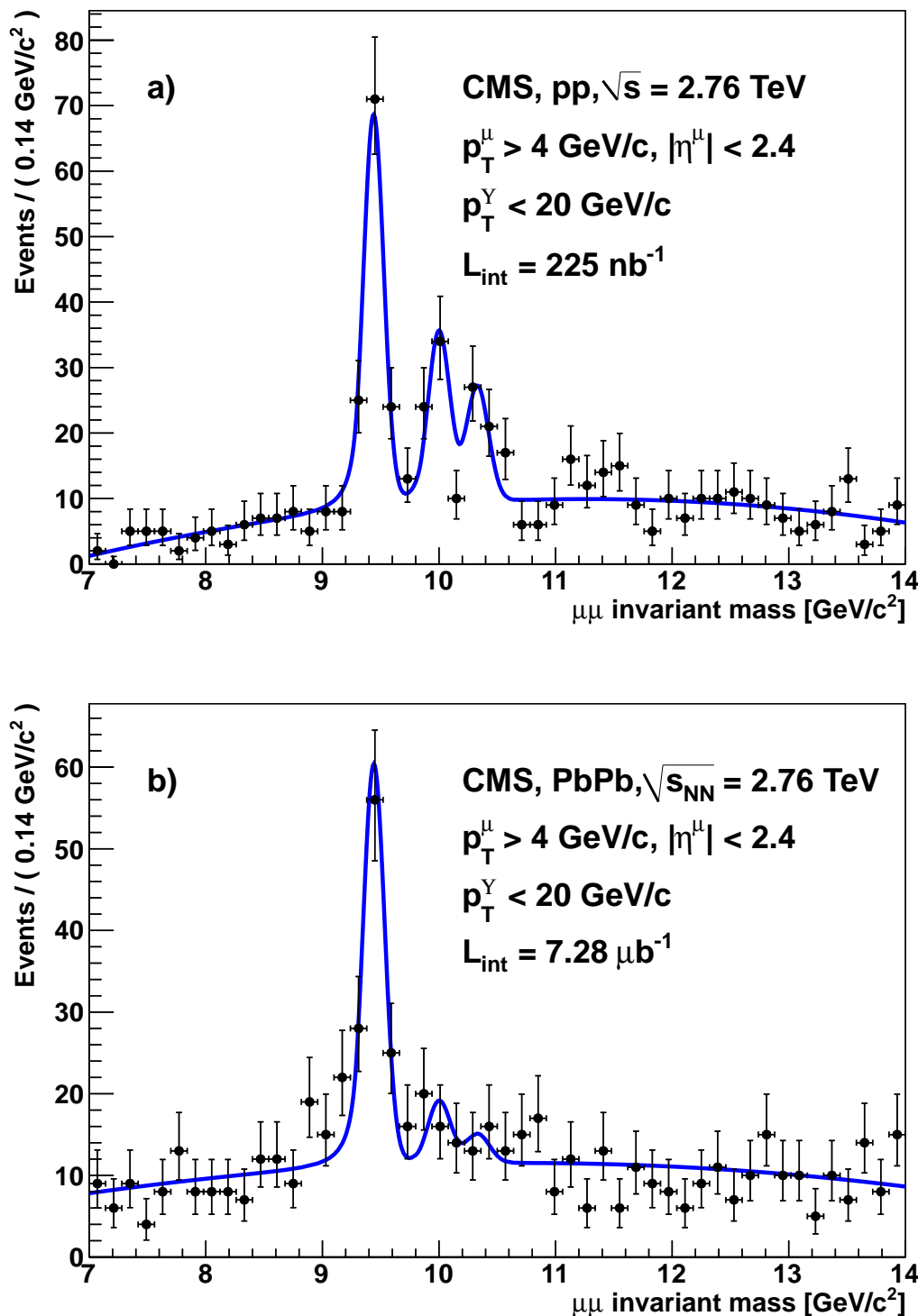


Figure 4.10.: Dimuon invariant-mass distributions from the p p (a) and PbPb (b) data at $\sqrt{s_{\text{NN}}} = 2.76$ TeV. The same reconstruction algorithm and analysis criteria are applied to both data sets, including a transverse momentum requirement on single muons of $p_T^\mu > 4$ GeV/c. The solid lines show the result of the fit described in the text.

values obtained via simulation. Finally, a second-order polynomial is chosen to describe the background in the 7–14 GeV/ c^2 mass-fit range. The quality of the unbinned fit is checked *a posteriori* by comparing the obtained lineshapes to the binned data of Fig. 4.10. The χ^2 probabilities are 74% and 77%, respectively for pp and PbPb.

The ratios of the observed yields of the $\Upsilon(2S)$ and $\Upsilon(3S)$ excited states to the $\Upsilon(1S)$ ground state in the pp and PbPb data are:

$$\Upsilon(2S + 3S)/\Upsilon(1S)|_{\text{pp}} = 0.78^{+0.16}_{-0.14} \pm 0.02, \quad (4.7)$$

$$\Upsilon(2S + 3S)/\Upsilon(1S)|_{\text{PbPb}} = 0.24^{+0.13}_{-0.12} \pm 0.02, \quad (4.8)$$

where the first uncertainty is statistical and the second is systematic.

The systematic uncertainties are computed by varying the lineshape in the following ways:

1. the CB-tail parameters are varied randomly according to their covariance matrix and within conservative values covering imperfect knowledge of the amount of detector material and FSR in the underlying process;
2. the resolution is varied by ± 5 MeV/ c^2 , which is a conservative variation given the current understanding of the detector performance and reasonable changes that can be anticipated in the Υ -resonance kinematics between pp and PbPb data;
3. the background shape is changed from quadratic to linear while the mass range of the fit is varied from 6–15 to 8–12 GeV/ c^2 ;

the observed root-mean-square of the results is taken as the systematic uncertainty. The quadrature sum of these three systematic uncertainties gives a relative uncertainty on the ratio of 10% (3%) on the PbPb (pp) data.

The ratio of the $\Upsilon(2S + 3S)/\Upsilon(1S)$ ratios in PbPb and pp benefits from an almost complete cancellation of possible acceptance and/or efficiency differences among the reconstructed resonances. A simultaneous fit to the pp and PbPb mass spectra gives the double ratio

$$\frac{\Upsilon(2S + 3S)/\Upsilon(1S)|_{\text{PbPb}}}{\Upsilon(2S + 3S)/\Upsilon(1S)|_{\text{pp}}} = 0.31^{+0.19}_{-0.15} \text{ (stat.)} \pm 0.03 \text{ (syst.)}, \quad (4.9)$$

where the systematic uncertainty (9%) arises from varying the lineshape as described above in the simultaneous fit, thus taking into account partial cancellations of systematic effects.

To evaluate possible imperfect cancellations of acceptance and efficiency effects in the double ratio, a full GEANT4 [94] detector simulation is performed. The effect of the higher PbPb underlying event activity is considered by embedding, at the level of detector signals, $\Upsilon(1S)$ and $\Upsilon(2S)$ decays simulated by PYTHIA 6.424 [89] in PbPb events simulated with HYDJET [95]. Track characteristics, such as the number of hits and the χ^2 of the track fit, have similar distributions in data and simulation. As mentioned above, the trigger efficiency is evaluated with data, by using single-muon-triggered data events, and reconstructing J/ψ signal with and without the dimuon trigger requirement. The same exercise is carried out with the simulation and it agrees with the efficiency measured in data at the 2% level. The track efficiency in the silicon detector is measured with standalone muons, applying all selection criteria. The efficiencies in data and simulation agree within the 4% statistical uncertainty of the efficiency determined from data. The difference in reconstruction and selection efficiencies between the Υ states is less than 5% and the variation with charged particle multiplicity is less than 10% from pp to central PbPb collisions, producing a maximum change of 0.5% on the double ratio. The good agreement between single-muon trigger efficiencies extracted from data for the pp and PbPb trigger requirements, applied to the $\Upsilon(1S)$ and $\Upsilon(2S)$ trigger efficiencies derived from simulation, leads to a negligible effect on the double ratio. The single-muon trigger efficiencies extracted from data agree within 1.5% for the pp and PbPb trigger requirements, and the $\Upsilon(1S)$ and $\Upsilon(2S)$ trigger efficiencies agree within 3%, according to simulation: the potential trigger bias on the double ratio is negligible. The magnitudes of the statistical and systematic uncertainties on the double ratio, respectively 55% and 9%, are significantly larger than the systematic uncertainties associated with possible imperfect cancellation of acceptance and efficiency effects. Therefore no additional uncertainty from these sources is applied. Finally, using an ensemble of one million pseudo-experiments, generated with the signal lineshape obtained from the pp data (Fig. 4.10a), the background lineshapes from both data sets, and a double ratio (Eq. 4.9) equal to unity within uncertainties, the probability of finding the measured value of 0.31 or below is estimated to be 0.9%. In other words, in the absence of a suppression due to physics mechanisms, the probability of a downward departure of the ratio from unity of this significance or greater is 0.9%, i.e. that corresponding to 2.4 sigma in a one-tailed integral of a Gaussian distribution. Studies in section 4.6 show that the $\Upsilon(1S)$ itself is suppressed by about 40% in minimum bias PbPb collisions at $\sqrt{s_{\text{NN}}} = 2.76$ TeV.

Since a large fraction of the $\Upsilon(1S)$ yield arises from decays of heavier bottomonium states [102], this $\Upsilon(1S)$ suppression could be indirectly caused by the suppression of the excited states.

Production yields of quarkonium states can also be modified, from pp to PbPb collisions, in the absence of QGP formation, by cold nuclear matter effects [71]. However, such effects should have a small impact on the Υ double ratio reported here. The nuclear modifications of the parton distribution functions (shadowing) should have an equivalent effect on the three Υ states, because their production involves very similar partons, cancelling in the ratio, at least to first order. The same should happen to any other initial-state nuclear effect. In principle, the larger and more loosely bound excited quarkonium states are more likely to be broken up by final-state interactions while traversing the nuclear matter, something extensively studied in the context of charmonium suppression at lower energies [104]. This “nuclear absorption” becomes weaker with increasing energy, and should be negligible at the LHC. At RHIC energies, the STAR experiment [?] has reported a $\Upsilon(1S + 2S + 3S)$ yield in dAu collisions of $0.78 \pm 0.28 \pm 0.20$ times the yield expected by scaling pp collisions, compatible with the absence of absorption. Furthermore, the double ratio presented here would only be sensitive to a *difference* between the nuclear dependencies of the three states and already at much lower energies the Fermilab E772 experiment observed [105], in proton-nucleus collisions, no such difference, within uncertainties, between the $\Upsilon(1S)$ and the sum $\Upsilon(2S + 3S)$.

4.8. Discussion

The $\Upsilon(1S)$ yield divided by T_{AA} as a function of p_T , rapidity, and centrality has been measured in PbPb collisions. No strong centrality dependence is observed within the uncertainties. The nuclear modification factor integrated over centrality is $R_{AA} = 0.63 \pm 0.11$ (stat.) ± 0.09 (syst.). This suppression is observed predominantly at low p_T . Using $p\bar{p}$ collisions at $\sqrt{s} = 1.8$ TeV, CDF measured the fraction of directly produced $\Upsilon(1S)$ as $(50.9 \pm 8.2$ (stat.) ± 9.0 (syst.))% for $\Upsilon(1S)$ with $p_T > 8$ GeV/ c [102]. Therefore, the $\Upsilon(1S)$ suppression presented in this paper could be indirectly caused by the suppression of excited Υ states. Comparison of the relative yields of Υ resonances has been performed in PbPb and pp collisions at the same centre-of-mass energy per nucleon pair of 2.76 TeV. The double ratio of the $\Upsilon(2S)$ and $\Upsilon(3S)$ excited states to the $\Upsilon(1S)$ ground state

in PbPb and pp collisions, $[\Upsilon(2S + 3S)/\Upsilon(1S)]_{\text{PbPb}}/[\Upsilon(2S + 3S)/\Upsilon(1S)]_{\text{pp}}$, is found to be $0.31^{+0.19}_{-0.15}$ (stat.) ± 0.03 (syst.), for muons of $p_T > 4 \text{ GeV}/c$ and $|\eta| < 2.4$. The probability to obtain the measured value, or lower, if the true double ratio is unity, has been calculated to be less than 1%.

Chapter 5.

Detail study of Υ suppression in Pb+Pb collisions using $150 \mu\text{b}^{-1}$ data with CMS detector at LHC.

5.1. Introduction

The LHC allows for the first detailed studies of the bottomonium family of states in ultra-relativistic heavy-ion collisions. Given the momentum resolution attained, and the capability of the trigger system, CMS is well positioned to lead these studies. The measurement of bottomonium production and suppression is presented, based on the dataset collected by the CMS experiment during the 2011 PbPb collision run at $\sqrt{s_{NN}} = 2.76\text{TeV}$.

If a deconfined medium is formed in high-energy heavy-ion collisions, one of its most striking expected characteristics is the suppression of quarkonium states [?]. This takes place as the force between the constituents of the quarkonium state, a heavy quark and its antiquark, is weakened by the color screening produced by the surrounding light quarks and gluons. The suppression is predicted to occur above a critical temperature of the medium, and sequentially, in the order of the $Q\bar{Q}$ binding energy. Since the $\Upsilon(1S)$ is the most tightly bound state among all quarkonia, it is expected to be the one with the highest dissociation temperature. Such a suppression pattern is expected to further depend on complications arising from additional phenomena sometimes referred to as *hot* and *cold* nuclear matter effects [71, 106]. The study of charmonium (J/ψ , ψ' , χ_c) and bottomonium ($\Upsilon(1S)$, $\Upsilon(2S)$, $\Upsilon(3S)$, χ_b) production at the unprecedented medium

created at the LHC is accordingly much awaited. In this chapter, the measurements of the production and suppression of the $\Upsilon(1S)$, $\Upsilon(2S)$, and $\Upsilon(3S)$ states are performed. The production of $\Upsilon(nS)$ states is studied by comparing their production rates in PbPb and pp collision data, taken at the same collision energy of $\sqrt{s_{NN}} = 2.76 \text{ TeV}$. In particular, the yield of the higher-mass states is measured relative to the ground state. In this way, we explore the double ratios – $\Upsilon(2S, 3S) vs \Upsilon(1S)$ and $\text{PbPb} vs \text{pp}$ – which allows a self-calibrating measurement. Several effects associated to selection, acceptance, and reconstruction mostly cancel, and only remaining factors need to be accounted for, as corrections to the fitted ratio of raw signal yields. Based on the dataset collected during the first LHC PbPb run, at $\sqrt{s_{NN}} = 2.76 \text{ TeV}$, in 2010, and in the special pp run at the same energy in early 2011, CMS has published first results on upsilon production and suppression in PbPb collisions. These included the first evidence for suppression of the excited Υ states relative to the ground state, at the 2.4σ level as discussed in chapter???. Suppression of the $\Upsilon(1S)$ state, relative to pp collisions at the same energy, has also been measured [107, 108]. These two measurements were found to be consistent with suppression of only the excited states, which result in reduced feeddown from excited to ground states. These main results may be summarized as follows:

$$\begin{aligned}\Upsilon(2S + 3S)/\Upsilon(1S)|_{\text{PbPb}} &= 0.24^{+0.13}_{-0.12} \pm 0.02, \\ \Upsilon(2S + 3S)/\Upsilon(1S)|_{\text{pp}} &= 0.78^{+0.16}_{-0.14} \pm 0.02, \\ (\chi \equiv) \frac{\Upsilon(2S + 3S)/\Upsilon(1S)|_{\text{PbPb}}}{\Upsilon(2S + 3S)/\Upsilon(1S)|_{\text{pp}}} &= 0.31^{+0.19}_{-0.15} \pm 0.03, \\ (R_{AA} \equiv) \frac{\Upsilon(1S)|_{\text{PbPb}; 0-20\%}}{\Upsilon(1S)|_{\text{pp}}} &= 0.681 \pm 0.143 \pm 0.119.\end{aligned}$$

In the 2011 PbPb run, CMS collected a dataset approximately 20 times larger than that gathered in 2010. These data will be scrutinized, in order to extract further novel and precision results, during the few years ensuing datataking. In what follows, the corresponding analysis of upsilon suppression is detailed.

5.2. Data Selection

The data analysis starts with the Onia2MuMu skim which contains all pairs of global muons with an invariant mass larger than $2 \text{ GeV}/c$. All charge combinations are considered and all possible combinations within an event are kept. The package that was used for the skimming can be found in CVS under CMSSW/HeavyFlavorAnalysis/Onia2MuMu.

Starting from this skim a TTree is filled with single muons and muon pairs that pass quality criteria to reject the background of fake muons while keeping the efficiency of selecting real muons high.

In order to select good quality muons, different variables were studied. This section describes how the cuts are defined and what is the final set of quality criteria that used in the analysis. These might not be very important for a ratio analysis but it is also a preparation for a more detailed analysis of the nuclear modification factor.

Muon candidates are selected if reconstructed as *global muons*. Muon arbitration requirements are applied, specifically muons must be both global and tracker muons (accessed via the standard methods `isGlobal()` and `isTracker()`). Muon candidates are accepted if belonging to the kinematic region given by

$$|\eta^\mu| < 2.4 \quad \text{and} \quad p_T^\mu > 4.0 \text{GeV}/c. \quad (5.1)$$

where the single muon p_T cut was determined with the optimization procedure described below. This region is within acceptance for muon reconstruction. The optimal muon p_T threshold for the analysis is investigated in Sec. 5.2.3.

5.2.1. Optimization procedure

The leading figure of merit employed in the optimization study is the $\Upsilon(1S)$ peak significance, \mathcal{S} , defined as

$$\mathcal{S} \equiv \frac{N_{\text{signal}}}{\sqrt{N_{\text{signal}} + N_{\text{background}}}}, \quad (5.2)$$

where N_{signal} and $N_{\text{background}}$ are the $\Upsilon(1S)$ signal and background yields, respectively, estimated in a $\pm 100 \text{MeV}/c^2$ signal window around the $\Upsilon(1S)$ peak. Each variable will be studied for dimuons falling in the Υ mass range $\in [7, 14] \text{GeV}/c^2$. The signal yields are obtained from the Monte Carlo sample. by counting the dimuons in the $[-0.1, 0.1] \text{GeV}/c^2$ signal window around the $\Upsilon(1S)$ peak. The background yields are estimated from the data in the signal window around the $\Upsilon(1S)$ peak. It is important to note that using the significance on data to check the effect of a cut on the signal and background could lead to a bias in the results if one would try to optimize the signal only looking at the data. This is why a careful attention was made to only use the significance as an indicator of

the impact of the background rejection. We always associated the significance value with the efficiency estimation based on the MC sample. The samples used include:

- realistic Υ embedded in HYDJET PbPb background: where the signal efficiency can be studied with the caveat that because one signal is embedded per minimum bias event, the signal over background ratio is greatly over-estimated;
- prompt reconstruction of the data: where the background rejection can be studied

5.2.2. Track and dimuon quality

The following quantities are studied:

- the number of valid hits within the pixels and the strips (inner tracker) a single muon track has, indicating how good the inner track part of the track is;
- the number of pixel layers, with valid hits, crossed by a single muon. There are 2-3% of muons with tracks with 0 pixel hit;
- the χ^2/ndf of the single muon inner track, which indicates the quality of the inner track fit;
- the χ^2/ndf of the single muon global track, which indicates the quality of the global fit;
- the number of muon valid hits
- the distance between the event vertex and the muon track in the transverse plane, D_{xy} , and the longitudinal plane, D_z , which indicates if the muon comes from a decay in flight or is a prompt muon, and removes cosmics;
- the probability of two tracks to belong to the same decay vertex.

In addition to the significance \mathcal{S} , the following factors are also estimated: (i)the efficiency of the signal using the MC sample, defined as the signal fraction measured after applying the cut, relative the number of signal events found before applying the cut; and (ii)the background rejection, defined as one minus the background fraction estimated after applying the cut, relative to the background yield estimated without the cut. These estimators are evaluated for each variable, applying all other cuts, as a function of the cut threshold value. This is an iterative process, where the standard thresholds of Ref. [?] are used as a first iteration step. The procedure is applied to several track quality criteria.

The aim is to confirm the goodness of the standard thresholds applied, and identify potential gains in significance that could be attained by adjusting the threshold of some of the inspected variables. In general, when only marginal significance improvements would be obtained, we opt to conservatively retain the initial standard cut thresholds; this is true in particular for those variables which could be affected by possible mismatches between data and simulation. Figures 5.1–5.8 show, for each variable, the variation of the significance \mathcal{S} , on the left. On the right hand side, the signal efficiency and background rejection, as a functions of the probed cut value, are also displayed. For all variables but the one being studied, the default values are applied. In general, the cut chosen is the one that keeps as much signal as possible on the MC with a relatively good significance. For all plots the background rejection behaves similarly (but symmetrically) to the efficiency. This suggests that the background is mostly made of real tracks and/or muons, and thus difficult to reduce. Figure 5.1 shows that, for the inner track number of valid hits, the significance starts dropping when more than 13 valid hits for the muon inner track is required on the data and the efficiency at 12. The cut chosen is `mu_innerTrack_Hits>10`.

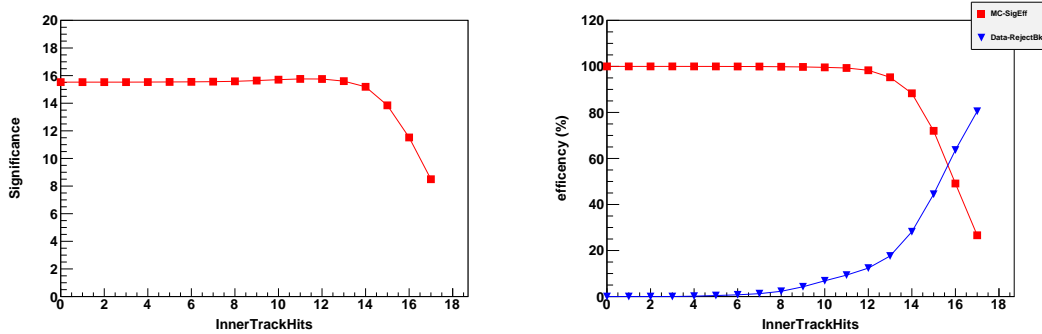


Figure 5.1.: Number of muon inner track valid cut study (default: > 10).

Figure 5.2 shows that for the number of pixel layers, with valid hits, crossed, the significance and the efficiency are flat for 1 or 2 but there is a slight efficiency drop with the requirement of 3 pixel layers to be fulfilled, as does the significance slightly. The cut chosen is `mu_pixelLayers>0`.

Figure 5.3 shows that for the inner track χ^2/ndf , the significance is mostly flat while the efficiency increases until about 2 and then stay maximal. The conservative cut picked is:

`mu_innerTrack_chi2NDOF<4`.

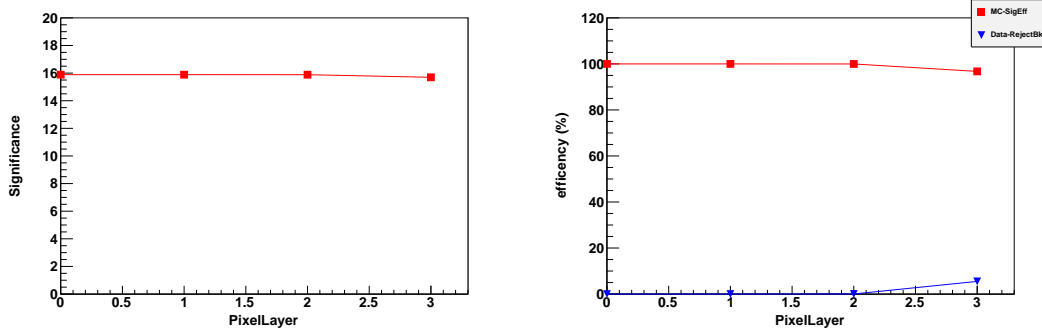


Figure 5.2.: Number of muon pixel layers cut study(default: > 0).

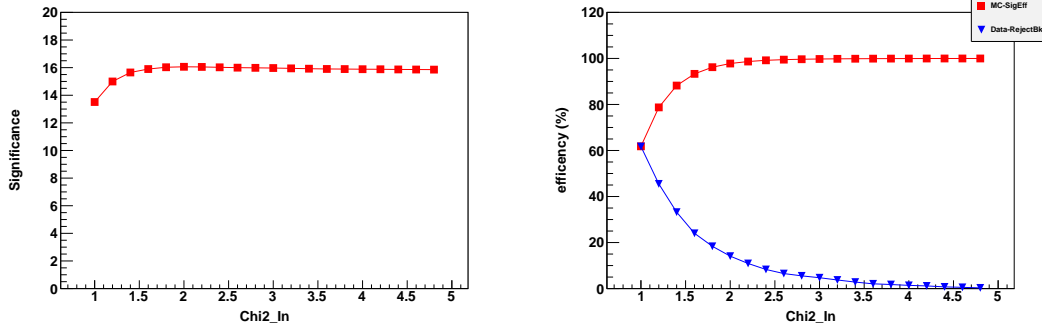


Figure 5.3.: Number of muon inner track χ^2/ndf cut study (default: < 4).

Figure 5.4 shows that for the global track χ^2/ndf , the significance increases up to above 4 and then is constant. The conservative cut picked is: mu_globalTrack_chi2NDOF<20.

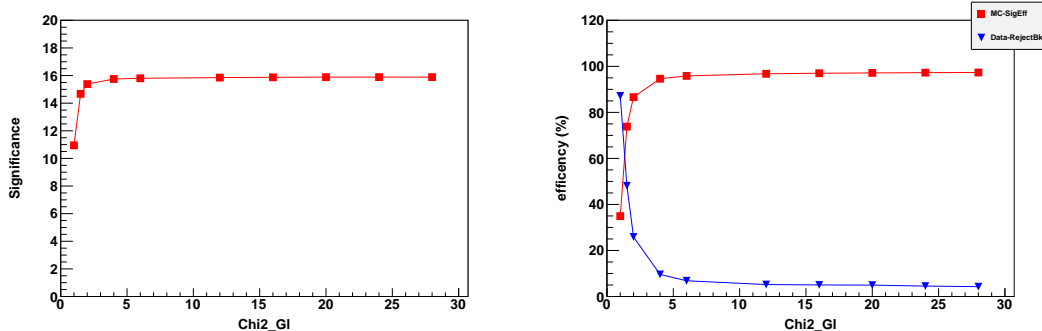


Figure 5.4.: Number of muon global track χ^2/ndf cut study (default: < 20).

Figures 5.6 and 5.7 shows the significance on data and the efficiency and background rejection on MC for different values of D_{xy} and D_z while applying all other cuts. The final cuts are chosen: mu_dxy<3.0 cm and mu_dz<15.0 cm.

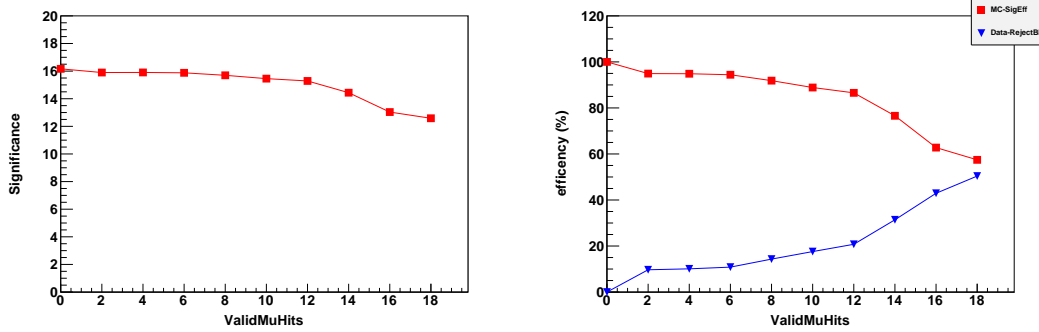


Figure 5.5.: Number of valid muon hits cut study (default: ≥ 0).

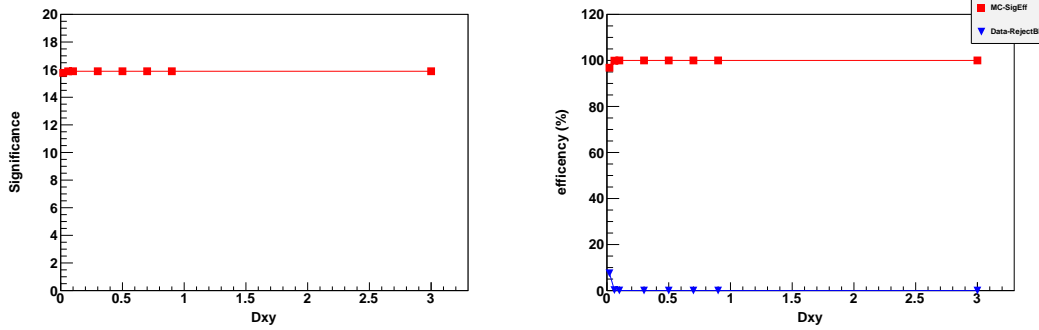


Figure 5.6.: D_{xy} cut study (default: < 3).

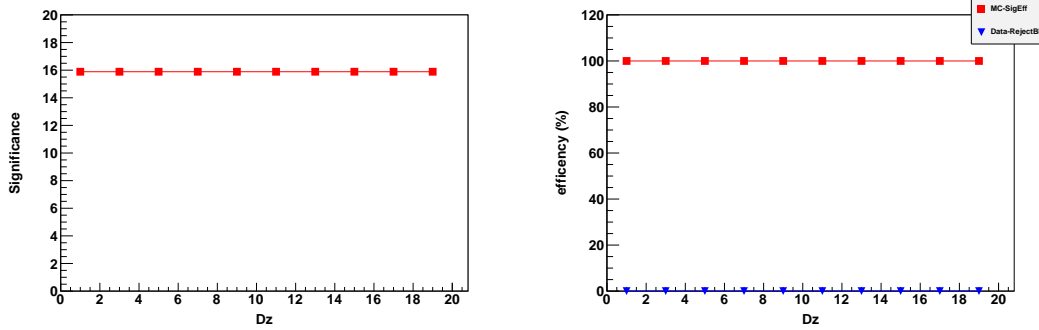


Figure 5.7.: D_z cut study (default: < 15).

Figures 5.8 show for the vertex probability study, the significance is constant as all other cuts are applied. A reasonable 5% cut for the vertex probability is chosen.

It is to be noted that the arbitration cut (the requirement of the muon to be both global and tracker muon) has already a very good efficiency, and thus is applied in the final set of quality criteria.

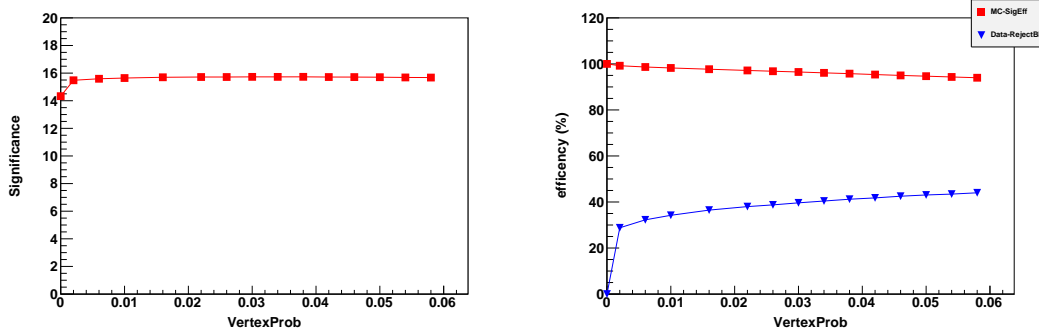


Figure 5.8.: Dimuon vertex probability cut study (default: $> 5\%$).

5.2.3. Kinematic threshold

The single muon p_T cut was chosen according to the described optimization procedure considering also the effect of the p_T cut on the shape of the background.

Statistical optimization

The optimization of the single muon p_T cut is here based on the $1S$ peak singificance, as in Eq. 5.2. Similarly to what was already described above, the signal is determined from MC counting the dimuons falling into the $\pm 100\text{MeV}/c^2$ mass window around the $\Upsilon(1S)$ peak normalized to the signal in data. The signal level in data is determined from the simultaneous fit of the $\Upsilon(nS)$ mass peaks and the background, where we take the integral of the $1S$ peak fit in the same mass window. The background is derived from the mass sidebands, counting the dimuons falling into two $1\text{ GeV}/c^2$ wide intervals placed symmetrically around the $\Upsilon(1S)$ peak. The number of counts then must be normalized to the size of the signal window to estimate the background below the peak.

The results of the calculation are shown in Fig. 5.9, for three different values of the signal mass window size. The points show a maximum at the single muon $p_T > 4.0\text{ GeV}/c$, independent of the size of the signal window chosen. This optimization method indicates the best choice of the cut value to be $4.0\text{ GeV}/c$.

It is important to note that this optimization procedure finds the single muon p_T cut giving the most significant $\Upsilon(1S)$ yield. As one of the main goals of this analysis is the measurement of the relative suppression of Υ excited states with respect to the ground state and pp reference, alternative figures of merit are further investigated. It should be further noted that systematic effects are not accounted for in the procedure.

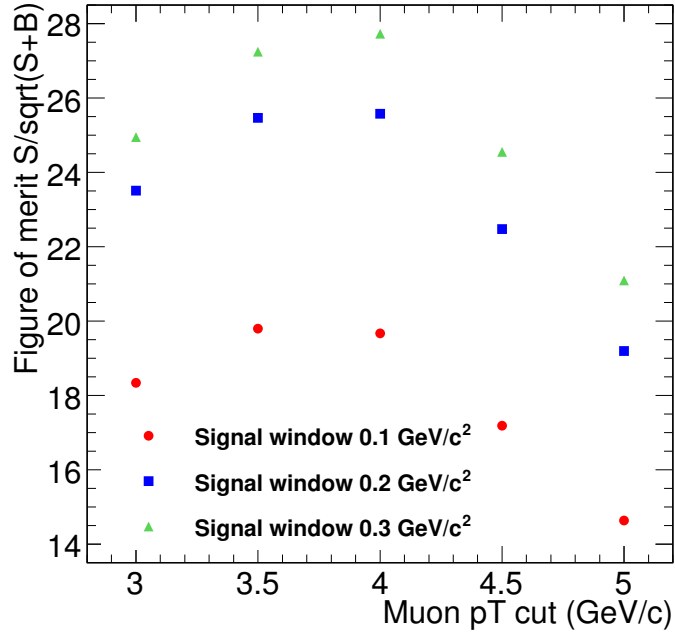


Figure 5.9.: Significance of $\Upsilon(1S)$ peak as a function of the single muon p_T cut

Background shape sculpting

In the selection of the single muon p_T cut, the dependence on the shape of the background should be also considered. These effects may be conveniently estimated by inspecting the invariant mass spectrum of the same-sign muon pairs. Figure 5.10 shows the same-sign muon-pairs mass spectra, in the vicinity of the $\Upsilon(nS)$ mass region, obtained with different p_T^μ cut thresholds. The $\Upsilon(nS)$ signal nominal masses are: $9.46 \text{ GeV}/c^2$ (1S), $10.02 \text{ GeV}/c^2$ (2S), $10.36 \text{ GeV}/c^2$ (3S). In all cases, a peaking background distribution is expected, within the nominal fitting range; the mass value where the maximum occurs increases with the increasing p_T cut.

In the previous analysis [107], the cut $p_T > 4\text{GeV}/c$ was chosen. In this case, the background displays a peak hight underneath the $\Upsilon(nS)$ signal mass region. This results in a potentially larger systematic uncertainty associated to the background shape.

In case of the $p_T > 3.5 \text{ GeV}/c$ cut, the peak in the background spectrum is located to the left of the Υ signal region. This should allow a better constraint by the fitter of the background shape under the signal peaks. This argument therefore favors the $3.5 \text{ GeV}/c$ cut.

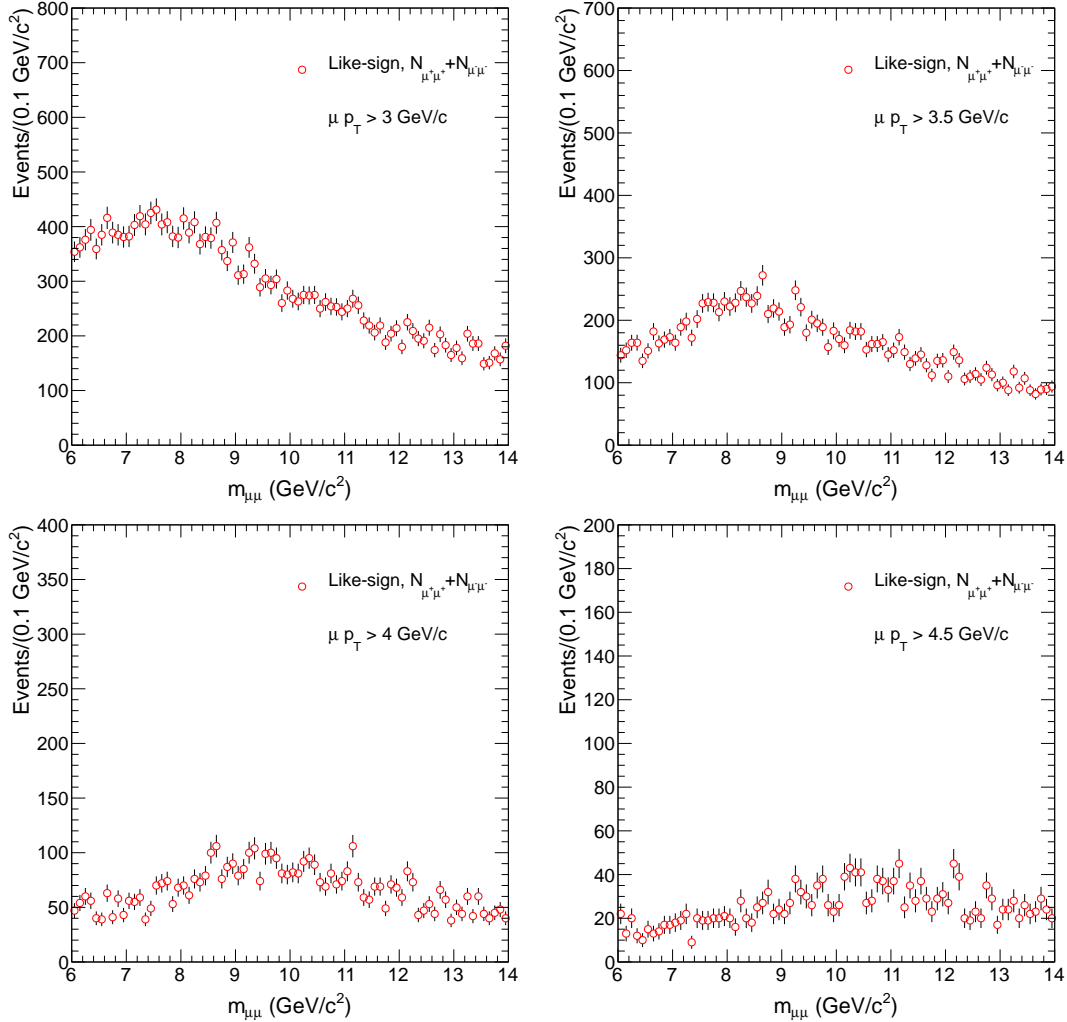


Figure 5.10.: Same-sign muon pairs invariant mass distribution with different muon p_T cuts, shown in the vicinity of the $\Upsilon(nS)$ mass region.

The p_T cut dependence of the combinatorial background shape was studied also in pp collisions at $\sqrt{s} = 7 \text{ TeV}$ in data and simulation [?]. A very similar trend is observed in pp collisions with much higher statistics. The kinematic cut removes a large portion of the background in the lower mass region and produces a step-like shape. For the case of the $p_T > 3.5 \text{ GeV}/c$ cut, this shape is located to the left of the Υ signals; in case of $p_T > 4 \text{ GeV}/c$ cut, it occurs instead well within the signal region, which leads to potential increases of the fit procedure uncertainties.

Alternative figures of merit

Alternative figures of merit were also investigated which aim at optimizing the precision of the ratio measurement (instead of the 1S peak significance).

The first alternative method attempts to minimize the uncertainty on the ratio $N(\Upsilon(2S) + \Upsilon(3S))/N(\Upsilon(1S))$, where the ratio is approximately estimated as $2B/(S+B)$. S is the signal counted from the MC $\Upsilon(1S)$ peak and B is the background in the signal window determined from the data sidebands assuming a linear mass shape. The $2S$ and $3S$ peaks are approximated by the background hypothesis, that is, assuming the background level overwhelms the signal, which is approximately the case. To normalize the background from data and signal from MC together, the 1S peak in data is fitted and the integral in the given signal window is used as normalization factor.

The uncertainty on the ratio to be minimized is $\frac{2B}{S+B} \sqrt{\frac{1}{2B} + \frac{1}{S+B}}$, as calculated with standard error propagation and using \sqrt{S} and \sqrt{B} as estimates for the uncertainties on S and B . The results of the calculation are shown in Fig. 5.11, for three different values of the signal mass window size. The points reach a minimum at single muon $p_T > 4 \text{ GeV}/c$ independent of the size of the signal window. This optimization method favors a p_T cut value at $4 \text{ GeV}/c$.

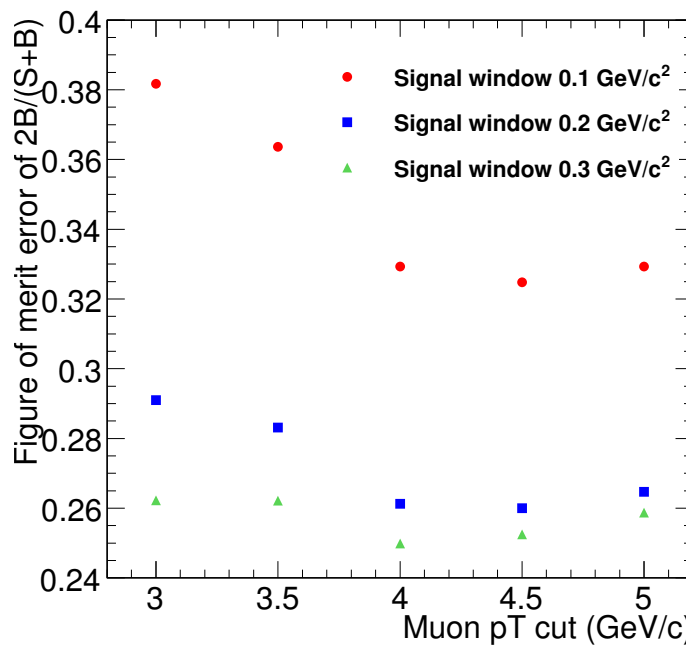


Figure 5.11.: Uncertainty on the $2B/(S+B)$ quantity as a function of the single muon p_T cut.

A third optimization method has also been explored, where we attempt to assess the expected sensitivity on the double ratio directly, by employing pseudo-experiments, generated according to fits performed to the data after each cut. The procedure is as follows. We fit the data sample and then generate 10000 toy MC pseudo-data according to parameters in the covariant matrix from the fitting. The double ratio of PbPb/ pp is generated at unity in the pseudo-data. The statistics of each sample is fixed to the amount of data we observe. These toys represent the outcome of many CMS experiments assuming nature had no upsilon excited state suppression. We plot the distribution of the ratio parameter, χ , measured in each toy experiment. We find the p -value (see Section ??) associated to a reference $\chi - 0.5$ value. We repeat the same steps for different selection cuts and identify the best cut the one resulting in the smallest p -value.

The plots for two different single muon transverse momentum thresholds, $p_T^\mu > 3.5\text{GeV}/c$ and $p_T^\mu > 4.0\text{GeV}/c$, are shown in Fig. ???. The reach of the two cuts is similar with the tighter cut yielding a smaller p -value. This is likely due to the signal to background ratio being better with the tighter cut. However, relevant systematic effects have not been included in the pseudo-experiments study.

$\Upsilon(1S)$ signal p_T

If we define the $\Upsilon(1S)$ signal region as (9.2, 9.8), the side-band region as (8, 8.5) and (12, 14), we can plot the signal events p_T distribution, side-band events p_T distribution, and side-band subtracted events p_T distribution, as shown in Fig. 5.12. The $\Upsilon(1S)$ signal mean p_T is $5.9\text{GeV}/c$ after side-band subtraction.

5.2.4. Summary of offline selection

In order to select good quality muons the effect of different cut thresholds on a variable set was studied. Table 5.1 shows the effect on the significance, as well as signal efficiency and background rejection, when applying all other cuts but the one studied. It further gives an indication of the correlation between the cuts. Once the nominal cut thresholds are applied, variations of a single cut have little impact on the significance.

In order to select muons in the acceptance and reject the background while keeping as much signal as possible a single muon p_T cut is introduced. The choice of the muon p_T cut value involves various considerations. The nominal cut is chosen to be $p_T > 4.0 \text{ GeV}/c$,

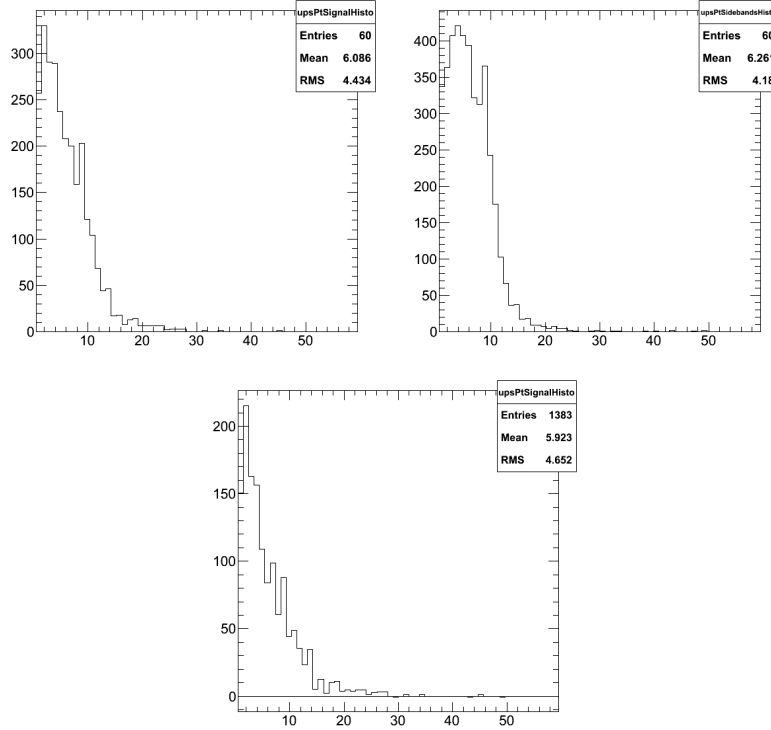

Figure 5.12.: $\Upsilon(1\text{S})$ p_T distributions

Table 5.1.: Estimated $\Upsilon(1\text{S})$ yield significance, signal efficiency (MC) and background rejection in % after applying all other cuts but the one listed.

Cut Variable	real data 1- ϵ_{Bkg} [%]	MC ϵ_{Bkg} [%]	Significance
InnerTrackHits > 10	51.0	85.0	14.5
PixeLayers > 0	54.1	84.6	14.6
InnerTrack χ^2/ndf < 4.	53.2	84.7	14.5
Dxy < 3. cm	54.1	84.6	14.6
Dz < 15. cm	54.1	84.6	14.6
GlobalTrack χ^2/ndf < 20	51.8	87.2	15.1
vProb > 0.05	20.2	89.5	13.7
TrackerMuonArbitrated = 1	52.7	84.9	14.5
All cuts	54.1	84.6	14.6

which was also used in the previous analysis iteration [107]. This is supported by the outcome of the statistical optimization procedure, employing different heuristic figures

of merit; in addition, the systematic effect due to the kinematic background may be controlled, as discussed in Sec. ???. The argument to support it is the significance study performed on the $\Upsilon(1S)$ peak that shows a maximum at $4.0 \text{ GeV}/c$. The second argument, perhaps even stronger than the first one, is the background shape variation due to the muon p_T cut.

Chapter 6.

Component of dimuon continuum

6.1. Introduction

Heavy-ion collisions study the interaction of matter at the extreme temperatures and densities where a Quark-Gluon Plasma (QGP), a phase of nuclear matter dominated by color degrees of freedom, is expected to form. Experimental efforts in this field began with the CERN SPS ($\sqrt{s_{NN}} \sim 16 - 19$ GeV) and evolved with data [110] from the first heavy-ion collider, the Relativistic Heavy-Ion Collider (RHIC) at Brookhaven National Laboratory ($\sqrt{s_{NN}} = 200$ GeV) in the last decade. The advent of Pb+Pb collisions at $\sqrt{s_{NN}} = 2.76$ TeV at the LHC has increased excitement in this field. One of the most striking QGP signals is quarkonium suppression [1]. Quarkonia are identified by their reconstructed mass peaks in the dilepton invariant mass distribution. Below ~ 12 GeV/c^2 , the dilepton distribution includes a number of resonance peaks: ρ , ω and ϕ at low masses and the ψ and Υ states at higher masses. At 91 GeV/c^2 , the $Z^0 \rightarrow l^+l^-$ peak appears. The continuum beneath these resonances is primarily composed of leptons from semileptonic decays of heavy flavor hadrons. These heavy flavor decays not only contribute to the resonance background but are important physics signals in their own right [111–116]. The continuum yields in Pb+Pb collisions compared to those in pp collisions can provide information about the medium properties. This makes it important to know the various contributions to the dilepton continuum in different kinematic regimes.

The first measurements of the dilepton spectra at the LHC have recently been reported [117–119]. The CMS experiment reported the first measurements of the Z^0 mass region in Pb+Pb collisions [117] as well as measurements of the full dimuon distribution, including quarkonia [118]. ATLAS has also reported J/ψ and Z^0 measurements in the dimuon

channel [119]. The second LHC Pb+Pb run, at much higher luminosity, has provided higher statistics measurements of the dilepton spectra over the full available phase space. With the measurement of dilepton spectrum in Pb+Pb collisions at the LHC, it is time to re-examine the continuum contributions to the dilepton mass spectrum. The production cross sections of $c\bar{c}$ and $b\bar{b}$ pairs at $\sqrt{s_{NN}} = 2.76$ TeV are calculated to next-to-leading order (NLO) and their correlated contributions to the dilepton continuum are subsequently obtained. We also include the effect of energy loss of charm and bottom quarks in the medium consistent with measurements of the suppression factor R_{AA} on the lepton spectra from semileptonic decays of charm and bottom [120, 121]. These contributions are compared to direct dilepton production from the Drell-Yan process and from thermal production in the medium. We then evaluate the relative importance of these contributions in the LHC detector acceptances.

While there have been previous studies of Pb+Pb collisions at 5.5 TeV [112, 114, 122], a re-examination is appropriate at the current, lower, center of mass energy and with the final detector acceptances. In addition, updated parameterizations of the parton distribution functions as well as estimates of the effect of energy loss on single particle spectra and determinations of the initial temperature from the charged particle multiplicity are now available and should lead to improved predictions. The experimental dilepton measurements presently concentrate on resonances. However, background-subtracted dilepton continuum measurements should soon be available with good statistics at 2.76 TeV in both pp and Pb+Pb collisions which could be used to infer properties of the medium produced in Pb+Pb collisions.

6.2. Dilepton production by hard processes

Dilepton production from semileptonic decays of $D\bar{D}$ (charm) and $B\bar{B}$ (bottom) meson pairs has been an area of active theoretical [112, 113, 115, 123, 124] and experimental [125] research. The large heavy quark mass allows their production to be calculated in perturbative QCD. We calculate the production cross sections for $c\bar{c}$ and $b\bar{b}$ pairs to NLO in pQCD [112, 113] using the CTEQ6M parton densities [126]. The central EPS09 parameter set [127] is used to calculate the modifications of the parton densities in Pb+Pb collisions. We include the theoretical uncertainty bands on charm and bottom production following the method of Ref. [128]. We use the same set of parameters as that of Ref. [128] with the exclusive NLO calculation of Ref. [129] to obtain the exclusive $Q\bar{Q}$ pair rates as

well as their decays to dileptons. We take $m_c = 1.5 \text{ GeV}/c^2$, $\mu_F/m_T = \mu_R/m_T = 1$ and $m_b = 4.75 \text{ GeV}/c^2$, $\mu_F/m_T = \mu_R/m_T = 1$ as the central values for charm and bottom production respectively. Here μ_F is the factorization scale, μ_R is the renormalization scale and $m_T = \sqrt{m^2 + p_T^2}$. The mass and scale variations are added in quadrature to obtain the uncertainty bands [128].

Figure 6.1 shows the uncertainty bands on the p_T and rapidity distributions of charm and bottom quarks in Pb+Pb collisions at $\sqrt{s_{NN}} = 2.76 \text{ TeV}$ with shadowing effects included. We only calculate the uncertainties in the production cross sections due to the mass and scale parameters and not those due to the EPS09 modifications or those of the parton densities. Both of these uncertainties are smaller than those due to the choice of mass and scale [130], particularly for $p_T \geq m$. The uncertainties on the heavy flavor production cross sections can be rather large, see Refs. [131, 132]. Thus the relative charm and bottom rates at 2.76 TeV may vary by a factor of two or more before dense matter effects such as energy loss are taken into account. While a recent reevaluation of the mass and scale parameters used to calculate charm production shows that the uncertainty on the charm production cross section can be reduced, it cannot be eliminated [130].

The differences in the quark p_T distributions are primarily at low p_T . For $p_T > 10 \text{ GeV}/c$, the uncertainty bands overlap almost completely with the upper limit on the bottom production band somewhat above the charm upper limit for $p_T > 20 \text{ GeV}/c$. The widths of the rapidity distributions are limited by the heavy quark mass. Thus the charm rapidity distribution is broader than that for bottom. The uncertainty bands are broader in rapidity than in p_T for charm and the bands for the two flavors are cleanly separated because the p_T -integrated rapidity distribution is dominated by low p_T where the charm cross section is clearly greater and the scale uncertainties are larger.

The production cross sections for heavy flavor and Drell-Yan dileptons at $\sqrt{s_{NN}} = 2.76 \text{ TeV}$ are shown in Table 6.1. The number of $Q\bar{Q}$ pairs in a minimum bias Pb+Pb event is obtained from the per nucleon cross section, σ_{PbPb} , by

$$N_{Q\bar{Q}} = \frac{A^2 \sigma_{\text{PbPb}}^{Q\bar{Q}}}{\sigma_{\text{PbPb}}^{\text{tot}}} . \quad (6.1)$$

At 2.76 TeV, the total Pb+Pb cross section, $\sigma_{\text{PbPb}}^{\text{tot}}$, is 7.65 b [133].

We assume that all the observed heavy flavor production in Pb+Pb collisions occurs during the initial nucleon-nucleon collisions. Thermal production of $Q\bar{Q}$ pairs is expected to be only a fraction of this initial production [112] unless the plasma is composed

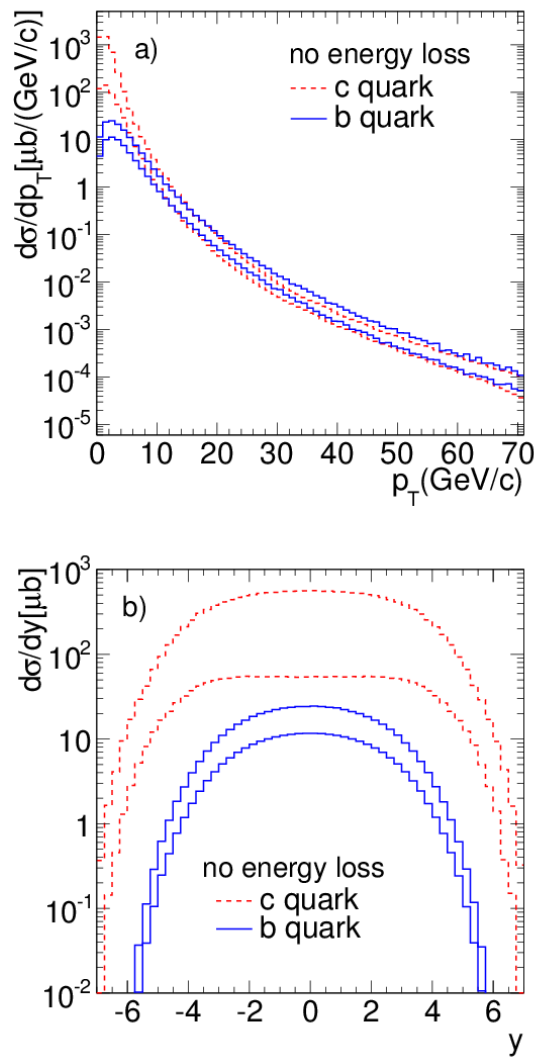


Figure 6.1.: (Color online) Theoretical uncertainty bands on inclusive single charm and bottom quark production cross sections per nucleon as functions of p_T (left) and rapidity (right) for $\sqrt{s_{NN}} = 2.76$ TeV. The uncertainties are calculated by varying the quark mass, renormalization scale μ_R and factorization scale μ_F . The calculations include modification of the initial parton distributions with the EPS09 central parameter set. No final state energy loss is included.

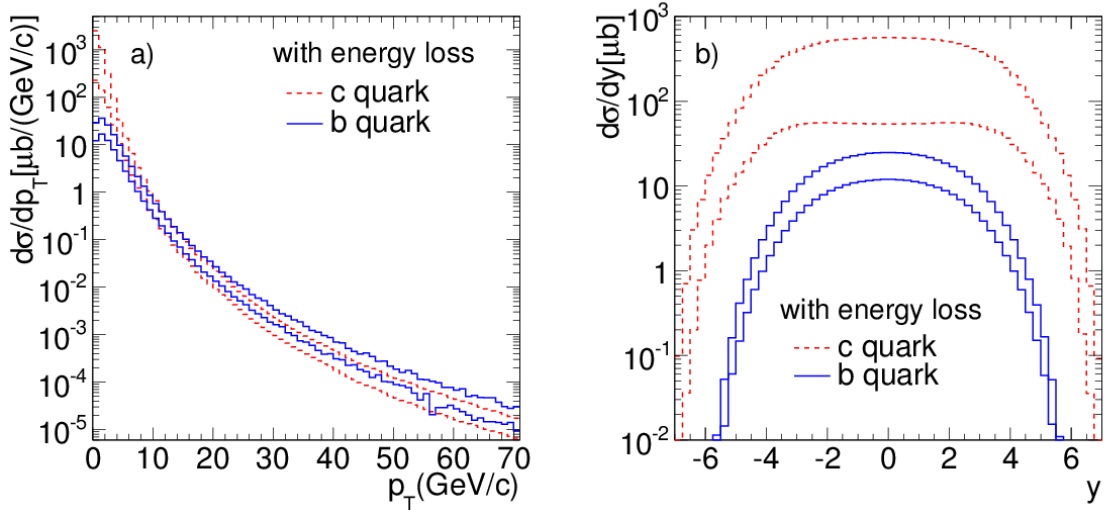


Figure 6.2.: (Color online) Theoretical uncertainty bands on inclusive single charm and bottom quark production cross sections per nucleon as functions of p_T (left) and rapidity (right) for $\sqrt{s_{NN}} = 2.76$ TeV. The uncertainties are calculated by varying the quark mass, renormalization scale μ_R and factorization scale μ_F . The calculations include modification of the initial parton distributions with the EPS09 central parameter set. Here we include final state energy loss assuming that the charm and bottom quark R_{AA} is the same, as discussed in the text.

of massive quasi-particles which would lower the effective threshold for heavy flavor production in the medium [134], enhancing production in this channel. However, such production would be at lower transverse momentum and with a narrower rapidity distribution than shown in Fig. 6.3.

Table 6.1.: Heavy flavor and Drell-Yan cross sections at $\sqrt{s_{NN}} = 2.76$ TeV. The cross sections are given per nucleon while $N_{Q\bar{Q}}$ and $N_{l^+l^-}$ are the number of $Q\bar{Q}$ and lepton pairs per Pb+Pb event. The uncertainties in the heavy flavor cross section are based on the Pb+Pb central values with the mass and scale uncertainties added in quadrature.

	$c\bar{c}$	$b\bar{b}$	DY	$1 \leq M \leq 100$ GeV
σ_{PbPb}	$1.76^{+2.32}_{-1.29}$ mb	$89.3^{+42.7}_{-27.2}$ μb	70.97 nb	
$N_{Q\bar{Q}}$	$9.95^{+13.10}_{-7.30}$	$0.50^{+0.25}_{-0.15}$	-	
$N_{\mu^+\mu^-}$	$0.106^{+0.238}_{-0.078}$	$0.0059^{+0.0029}_{-0.0017}$	0.0004	

The heavy quarks are decayed semileptonically and lepton pairs are formed from correlated $Q\bar{Q}$ pair decays. We do not consider uncorrelated $Q\bar{Q}$ contributions to the continuum since these should be eliminated by a like-sign subtraction. We assume that any uncorrelated dileptons from $c\bar{b}$ and $\bar{c}b$ decays are also removed by like-sign subtraction and that lepton pairs from a single chain decay, $B \rightarrow Dl_1X \rightarrow l_1l_2X'$, only contribute to the low mass continuum, see Ref. [114]. The number of lepton pairs is obtained from the number of $Q\bar{Q}$ pairs,

$$N_{\mu^+\mu^-} = N_{Q\bar{Q}}[B(Q \rightarrow lX)]^2 . \quad (6.2)$$

The values of $N_{Q\bar{Q}}$ and $N_{\mu^+\mu^-}$ are given in Table 6.1, along with their uncertainties.

Dilepton production by the Drell-Yan process has also been calculated to NLO in pQCD [135]. The cross section in the mass interval $1 < M < 100$ GeV, including EPS09 shadowing in Pb+Pb collisions, is given in Table 6.1. The integrated cross section is dominated by the lowest masses. The largest potential modification due to the presence of the nucleus is on the low mass rate, in the resonance region. At larger masses, this effect becomes competitive with the effects of the relative number of protons and neutrons in the nucleus compared to a pp collision (isospin effects) [136]. We have used PYTHIA [137] to generate the Drell-Yan p_T distribution and to place kinematic cuts on the individual leptons of the pair. The total rate has been normalized to the calculated NLO cross section. The pQCD uncertainties on the Drell-Yan rate, particularly above the resonance region, are not large. In general, they are smaller than the uncertainties due to the shadowing parameterization [136].

Finally, we include energy loss effects on the charm and bottom quarks. Since heavy quarks do not decay until after they have traversed the medium, their contribution to the final dilepton spectra will reflect its influence. Indications from inclusive non-photonic lepton spectra at RHIC [120], attributed to heavy flavor decays, suggest that the effects of energy loss are strong and persist up to high p_T . They also suggest that the magnitude of the loss is similar for that of light flavors, *i.e.* independent of the quark mass so that the effects are similar for charm and bottom. The source of this loss as well as its magnitude are still under investigation, see Ref. [138] and references therein.

To estimate the effects of energy loss on the dilepton continuum, we adjust the heavy quark fragmentation functions to give a value of R_{AA} for each flavor separately that is consistent with the measured prompt lepton R_{AA} in central Pb+Pb collisions at high p_T , $R_{AA} \sim 0.25 - 0.30$ [121], for both charm and bottom quarks. We then use these modified

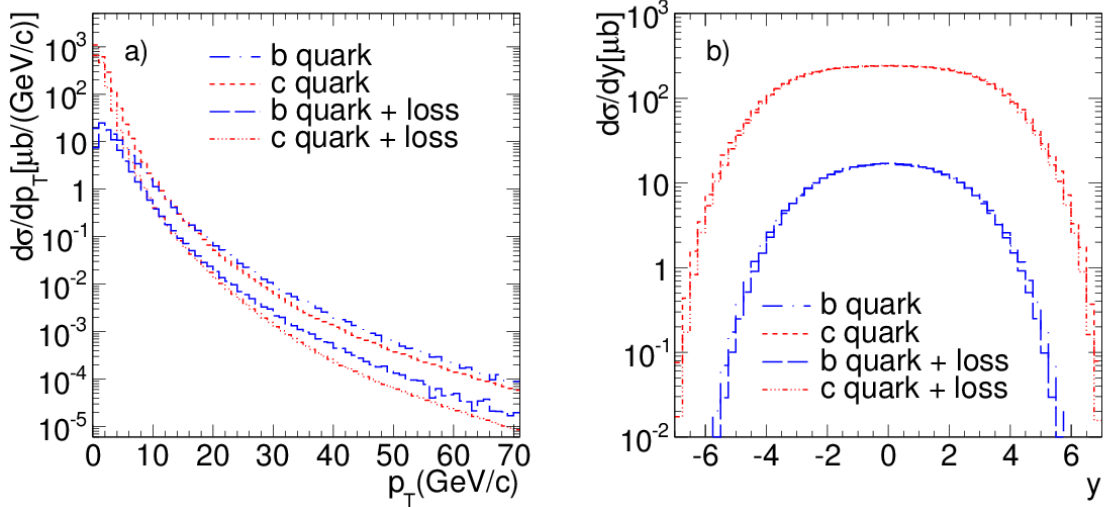


Figure 6.3.: (Color online) The inclusive single charm and bottom quark per nucleon cross sections as a function of p_T (left) and rapidity (right) both with and without energy loss in Pb+Pb collisions at $\sqrt{s_{NN}} = 2.76$ TeV. The cross sections, given per nucleon, include modification of the initial parton distributions via the central EPS09 shadowing parameterization.

fragmentation functions to calculate the medium-modified dilepton distributions from heavy flavor decays.

Including energy loss does not change the total cross section since it moves the quarks to lower momentum without removing them from the system. Thus the p_T -integrated rapidity distributions are also unaffected, see Fig. 6.2, which presents the single inclusive heavy flavor production uncertainty bands after energy loss. The charm and bottom quark p_T distributions still exhibit the same general behavior: the slopes are parallel to those without energy loss at high p_T but show a pile up of low p_T quarks after loss is included. After taking energy loss into account, the point where the bottom quark distribution begins to dominate is shifted to lower p_T , ~ 10 GeV/ c instead of ~ 20 GeV/ c when the widths of the bands are accounted for.

The relative strength of charm and bottom energy loss in medium is not yet settled. Although bottom quarks are expected to lose less energy than charm quarks, the data from RHIC and LHC exhibit important differences [139, 140]. If we assume that bottom quarks lose less energy than charm, then the bottom and charm quark uncertainty bands in Fig. 6.2 will separate at high p_T with the bottom quark band above that of the charm.

Figure 6.3 compares the central values of the uncertainty bands with and without energy loss directly. We note that the difference in the heavy flavor p_T distributions due to energy loss is larger than the uncertainty bands with and without energy loss. The rapidity distributions do not show any significant effect due to energy loss since the results are shown integrated over all p_T . Since the total cross sections are unchanged without any acceptance cuts, there is an effect only at far forward rapidity.

6.3. Thermal dilepton production

The contribution of thermal dileptons is calculated assuming that a QGP is formed in local thermal equilibrium at some initial temperature T_i and initial time τ_i which cools hydrodynamically through a 1D Bjorken expansion [141]. Assuming a first-order phase transition, when the QGP cools to the critical temperature T_c at time τ_c , the temperature of the system is held fixed until hadronization is completed at time τ_h . Afterwards, the hadron gas cools to the freeze-out temperature T_f at time τ_f [142].

The thermal dilepton emission rate due to $q\bar{q} \rightarrow l^-l^+$ is [142, 143]

$$\begin{aligned} \frac{dN}{d^4x d^2p_T dy dM^2} &= \frac{3}{(2\pi)^5} M^2 \sigma(M^2) F \exp(-E/T) \\ &= \frac{\alpha^2}{8\pi^4} F \exp(-E/T) . \end{aligned} \quad (6.3)$$

Here M , p_T and y are the mass, transverse momentum, and rapidity of the lepton pair while $d^4x = \tau d\tau \eta \pi R_A^2$ where η is the rapidity of the fluid with temperature T and $R_A = r_0 A^{1/3}$. The mass-dependent cross section, $\sigma(M^2) = F 4\pi \alpha^2 / 3M^2$ includes a factor F that depends on the phase of the matter. In a two-flavor QGP, $F_{\text{QGP}} = \sum e_q^2 = 5/9$, while, in the hadronic phase, form factors representing the resonance region [144] are used. We concentrate on masses above the resonance region. In the mixed phase,

$$F = (1 - h(\tau)) F_{\text{QGP}} + h(\tau) F_{\text{had}} , \quad (6.4)$$

where $h(\tau)$ is the hadron fraction of the mixed phase.

The dilepton p_T distribution is

$$\frac{dN}{d^4x dy dM dp_T} = \frac{\alpha^2}{4\pi^4} F M p_T \exp\left(-\frac{\sqrt{M^2 + p_T^2} \cosh(y - \eta)}{T}\right) \quad (6.5)$$

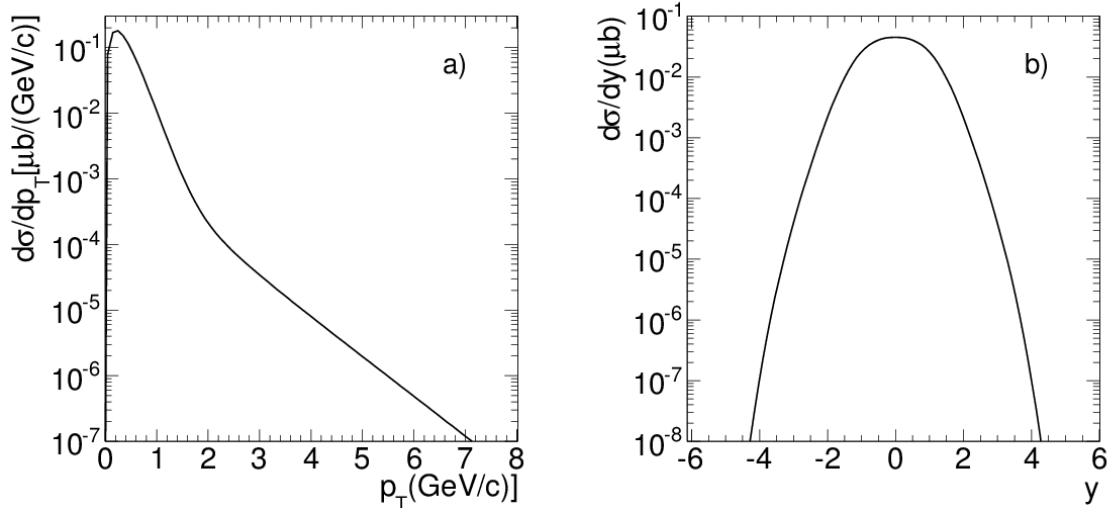


Figure 6.4.: The thermal dilepton cross section as a function of p_T (left) and rapidity (right) in Pb+Pb collisions at $\sqrt{s_{NN}} = 2.76$ TeV.

and the dilepton invariant mass distribution, integrated over p_T , is

$$\frac{dN}{d^4xdydm} = \frac{\alpha^2}{2\pi^3} F M^3 \left(\frac{1}{x^2} + \frac{1}{x} \right) \exp(-x), \quad (6.6)$$

where

$$x = \frac{M \cosh(y - \eta)}{T}. \quad (6.7)$$

The initial time is assumed to be $\tau_i = 0.1$ fm/ c . The initial temperature T_i is obtained from the total multiplicity distribution,

$$\frac{dN}{dy} = \tau_i T_i^3 4a_q \pi R_A^2 / 3.6, \quad (6.8)$$

where $dN/dy = 1.5 dN_{\text{ch}}/dy$. The charged particle multiplicity, $dN_{\text{ch}}/dy = 1600$, was measured in Pb+Pb collisions at 2.76 TeV [145]. Using this value with $a_q = 37\pi^2/90$ gives $T_i = 636$ MeV. The temperature decreases in the QGP as

$$T(\tau) = T_i \left(\frac{\tau_i}{\tau} \right)^{1/3} \quad (6.9)$$

for $\tau_i < \tau < \tau_c$. The temperature in mixed phase is $T = T_c = 160$ MeV. The mixed phase ends at $\tau_h = (a_q/a_h)\tau_c$ where $a_h = 3\pi^2/90$ for a pion gas. The hadronic fraction of

the mixed phase, $h(\tau)$, is

$$h(\tau) = \frac{a_q}{a_q - a_h} \left(\frac{\tau - \tau_c}{\tau} \right). \quad (6.10)$$

The temperature in hadron phase between $\tau_h < \tau < \tau_f$, is

$$T(\tau) = T_c \left(\frac{\tau_h}{\tau} \right)^{1/3}. \quad (6.11)$$

The thermal dilepton rate given in Eqs. (6.5) and (6.6) is converted to a cross section by dividing the rate by the minimum bias nuclear overlap, T_{PbPb} . Figure 6.4(a) and (b), shows the differential cross sections for thermal dilepton production as a function of p_T and rapidity. The p_T distribution, integrated over pair mass, shows two slopes, a steep decrease when the minimum pair transverse mass, M_T , is on the order of the temperature and a long tail when $M_T \gg T$. The rapidity distribution is significantly narrower than those resulting from the initial hard scatterings shown in Fig. 6.3.

This simple application of a one-dimensional Bjorken expansion through a first-order phase transition significantly overestimates the lifetime of the hot system. Thus, the results shown in Fig. 6.4 should be regarded as an upper limit on the thermal contribution.

To obtain the pair mass distributions including single lepton cuts, single leptons are generated by a Monte Carlo based on the pair M , p_T and y distributions using energy-momentum conservation.

6.4. Results and discussion

In Fig. 6.5, we show the theoretical uncertainty bands on the dilepton invariant mass distributions from semileptonic charm and bottom decays. The uncertainty bands for the decay dileptons are calculated identically to those of the charm and bottom quark distributions shown in Sec. 6.2. The dilepton uncertainty bands are broader than those for the single inclusive heavy flavors and, here, the dilepton band from charm decays is wider than for bottom. This is the case both without, Fig. 6.5(a), and with, Fig. 6.5(b), energy loss. While we show only the central values of these distributions in the remainder of this section, it is important to keep in mind the significant mass and scale uncertainties in heavy flavor production, considerably larger than those on high mass Drell-Yan production.

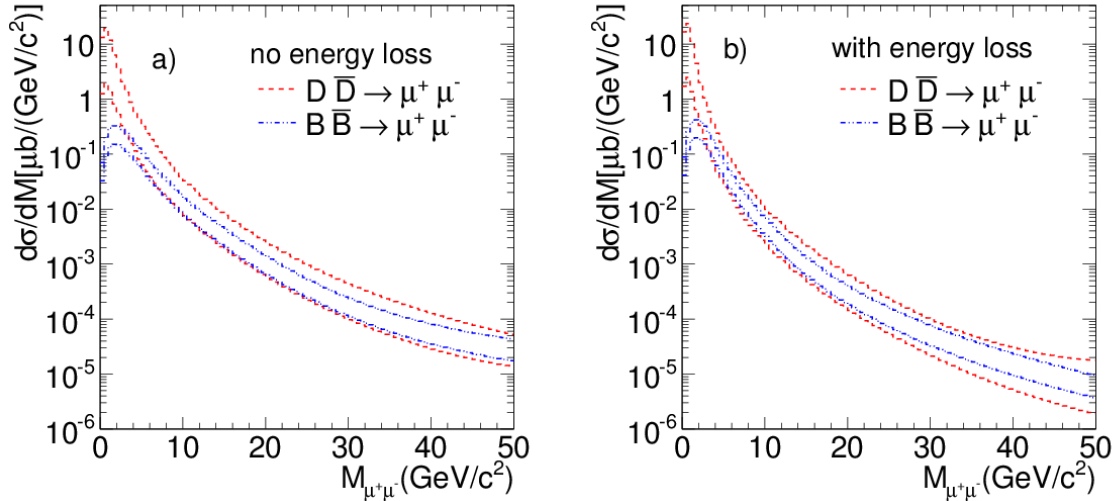


Figure 6.5.: (Color online) Theoretical uncertainty bands for the dilepton invariant mass distributions from semileptonic charm (red, short-dashed) and bottom (blue, dot-dot-dashed) decays. The uncertainties are calculated the same way as in Sect. 6.2.

Figure 6.6 shows the dimuon invariant mass distributions from each of the four sources considered: semileptonic decays of correlated $Q\bar{Q}$ pairs and direct production of Drell-Yan and thermal dileptons in Pb+Pb collisions at $\sqrt{s_{NN}} = 2.76$ TeV. Figure 6.6(a) shows the heavy flavor mass distributions without any final-state energy loss while energy loss is included in the heavy flavor distributions on Fig. 6.6(b). Only the central values of the heavy flavor contributions are shown. The Drell-Yan and thermal dilepton distributions are unchanged. No kinematic cuts are included. Without cuts, dileptons from $D\bar{D}$ decays dominate over the entire mass range due to the large $c\bar{c}$ production cross section. Bottom pair decays are the next largest contribution followed by Drell-Yan production. At masses below $3 \text{ GeV}/c^2$, the Drell-Yan and thermal dilepton contributions are competitive. Otherwise, the thermal contribution is negligible. Including energy loss steepens the slope of the heavy flavor mass distributions and also moves the $D\bar{D}$ decay distributions closer to the $B\bar{B}$ decay distributions. In the remainder of this section, we will show only results with final-state heavy flavor energy loss included.

We now examine these distributions in the kinematic regimes appropriate for the LHC detectors. CMS [146] and ATLAS [147] have excellent muon detectors with similar coverage in the central rapidity region, $|\eta^\mu| \leq 2.4$. However, due to the large magnetic fields, only muons above a rather high minimum p_T , $p_T > 3.0 \text{ GeV}/c$, make it into the muon detectors. ALICE [148] has muon acceptance on one side of the forward rapidity

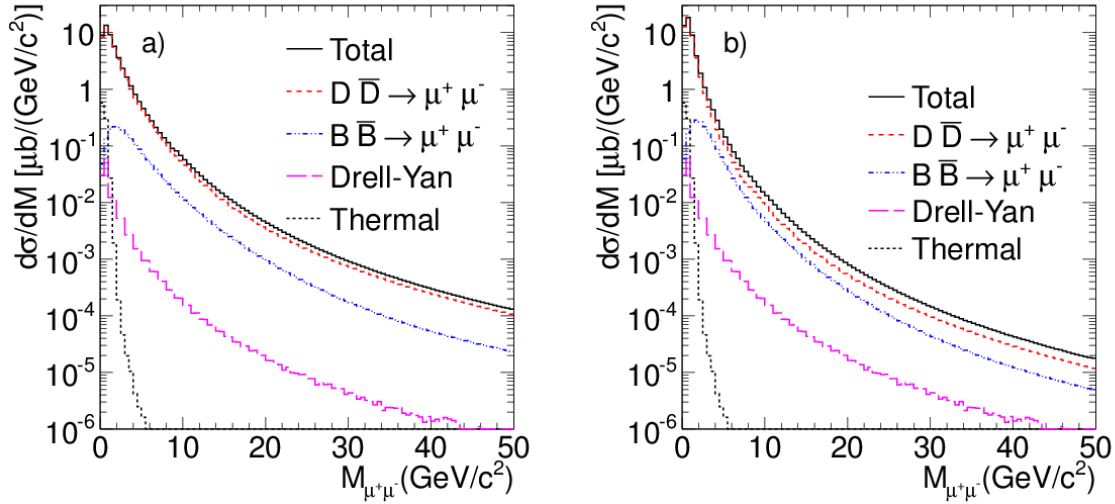


Figure 6.6.: (Color online) The invariant mass distributions for the four contributions to the dilepton spectra discussed here: semileptonic charm (red, short-dashed) and bottom (blue, dot-dot-dashed) decays, Drell-Yan (magenta, long-dashed) and thermal (black, dotted) dileptons along with the sum (black, solid) in Pb+Pb collisions per nucleon pair at $\sqrt{s_{NN}} = 2.76$ TeV. Left pannel shows distributions without any final state energy loss, right pannel is after including heavy quark energy loss in the medium. The per nucleon cross sections are given. No phase space or kinematic cuts are introduced.

region, $2.5 \leq \eta^\mu \leq 4.0$. At central rapidities, $|\eta^\mu| \leq 1.0$, ALICE has an electron detector. Some previous studies of Pb+Pb collisions at 5.5 TeV, using leading order calculations of heavy quark production and assuming significantly higher initial temperatures than employed here, suggested that thermal dileptons could be extracted from the QGP [122]. Thus they reached different conclusions about the relative contributions of thermal and heavy flavor dileptons to the continuum.

Figure 6.7 shows the dimuon invariant mass distribution for single muons in the range $|\eta^\mu| \leq 2.4$, together with several muon p_T cuts. Figure 6.7(a) has no muon p_T cut, only the η cut. Comparison with Fig. 6.6 shows that the thermal dilepton contribution is almost unaffected since its rapidity distribution is sufficiently narrow to fit within the CMS rapidity acceptance. Since the Drell-Yan rapidity distribution narrows with increasing mass, only the low mass region is affected by the rather broad rapidity cut of $|\eta^\mu| \leq 2.4$. Because the charm rapidity range is broader than that of bottom production, the dileptons from charm decays are most affected by the rapidity cut. For $M_{\mu^+\mu^-} > 5$ GeV/ c^2 , the charm dilepton yield has dropped below that of bottom.

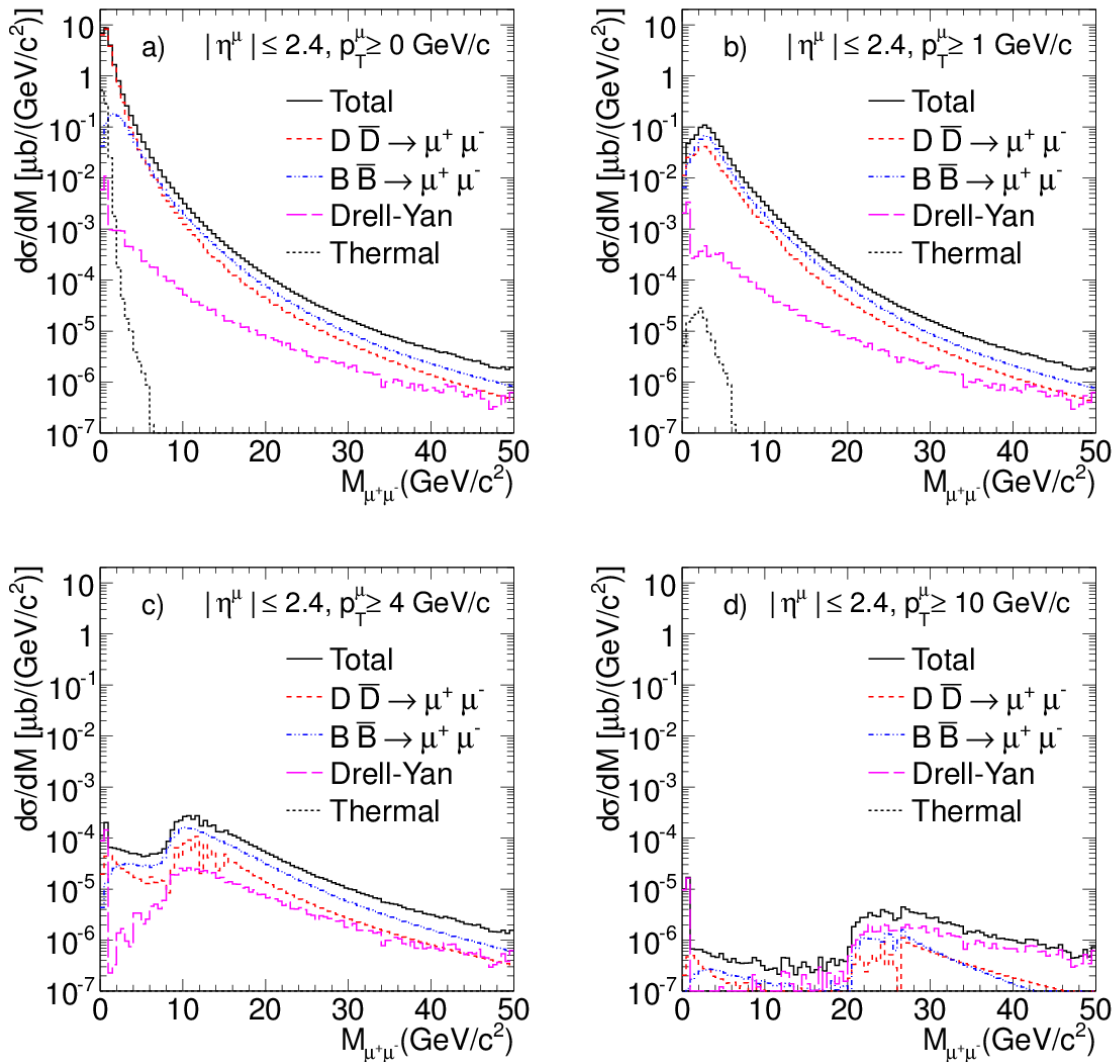


Figure 6.7.: (Color online) The same as Fig. 6.6 but now with single muon rapidity cuts of $|\eta^0| \leq 2.4$. A minimum single lepton transverse momentum cut of $p_T^\mu \geq 0$ (a), 1 (b), 4 (c) and 10 (d) GeV/c is also shown.

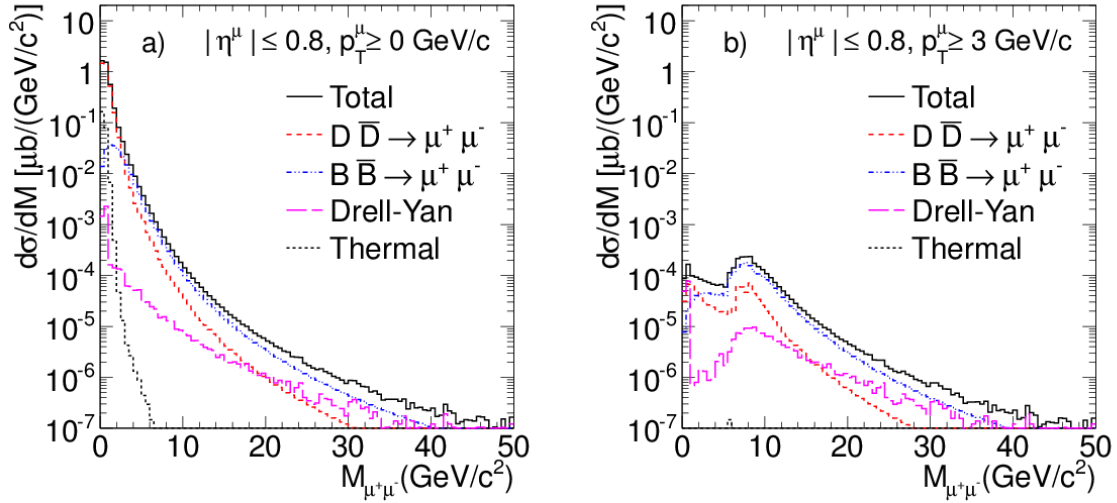


Figure 6.8.: (Color online) The same as Fig. 6.6 but now with single muon rapidity cuts of $|\eta^\mu| \leq 0.8$. A minimum single lepton transverse momentum cut of $p_T^\mu \geq 0$ (a) and 3 (b) GeV/c is also shown.

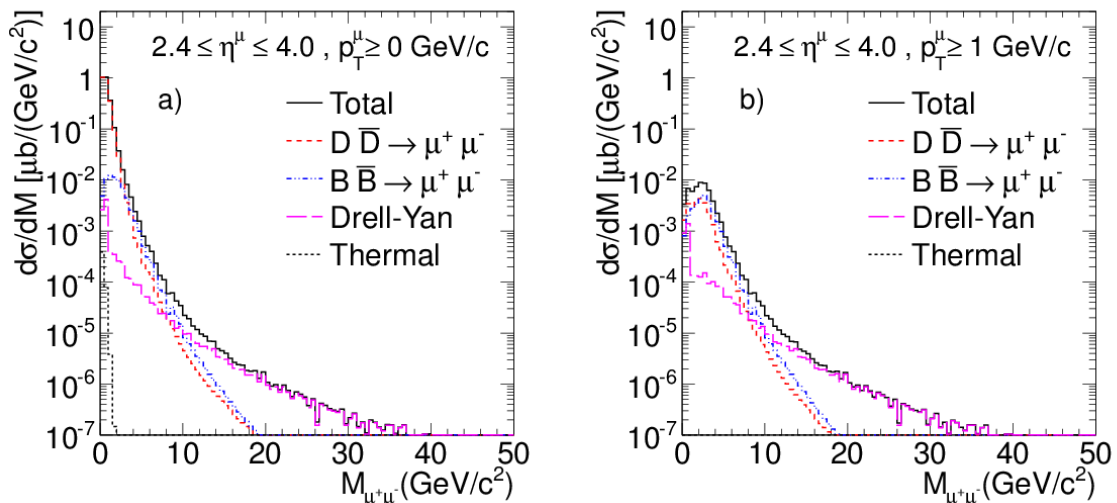


Figure 6.9.: (Color online) The same as Fig. 6.6 but now with single muon rapidity cuts of $2.4 \leq |\eta^\mu| \leq 4$. A minimum single lepton transverse momentum cut of $p_T^\mu \geq 0$ (a) and 1 (b) GeV/c is also shown.

Adding a cut on single lepton p_T disproportionately affects the low mass part of the continuum. As the minimum lepton p_T is increased from 1 GeV/ c to 10 GeV/ c in Figs. 6.7(b)-6.7(d), an ever-deepening dip appears in the dilepton mass distribution for $M_{\mu^+\mu^-} < 2p_T^\mu$. Even a relatively low p_T cut essentially eliminates the thermal dilepton contribution since these leptons have a rather soft p_T distribution. Since the charm and bottom quark p_T distributions have the same slope for $p_T > 7$ GeV/ c , their decays are affected the same way by the lepton p_T cut. Finally, the single lepton cut of $p_T^\mu > 10$ GeV/ c , published with the CMS Z^0 measurement [117], based on approximately 50 million events, had a very low continuum background. This is in agreement with the result in Fig. 6.7(d) which shows that, with energy loss included, the Drell-Yan process is now the dominant contribution to the continuum.

Figure 6.8 shows the dimuon mass distribution in the narrower central rapidity interval, $|\eta^\mu| \leq 0.8$, equivalent to the muon acceptance in the CMS barrel region and similar to the ALICE electron acceptance, $|\eta^e| \leq 1.0$. Figure 6.8(a) shows the dimuon distribution before any p_T cut. In this case, the mass distribution is more steeply falling in all cases except for thermal dilepton production because of its narrow rapidity distribution. Since the heavy flavor hadrons decay isotropically to leptons, the rapidity distribution for lepton pairs is rather broad with a width that is not strongly dependent on the pair mass. Thus the narrower rapidity acceptance reduces the high mass yields substantially relative to Fig. 6.7, even before any single lepton p_T cuts. Adding a single lepton transverse momentum cut of $p_T^\mu > 3$ GeV/ c , Fig. 6.8(b), suppresses the low mass part of the distribution. However, the mass distribution is essentially unaffected by the p_T^μ cuts for $M_{\mu^+\mu^-} > 8$ GeV/ c^2 .

Figure 6.9 shows the dimuon mass distributions in the forward region, $2.5 \leq \eta^\mu \leq 4.0$, relevant for the ALICE muon arm. In this case, after energy loss, the Drell-Yan cross section rises above the heavy flavor decay rate for $M_{\mu^+\mu^-} > 10$ GeV/ c^2 . The heavy flavor production kinematics favors central production, with a rather steep decrease in the rapidity distribution as the kinematic limit is approached. There is no such constraint on the resulting lepton pairs. Because the decay of the individual heavy quark is isotropic in its rest frame, the lepton rapidity distribution has a larger plateau region, extending to more forward rapidity, than the parent quark. However, restricting the cut to one side of midrapidity eliminates many large gap pairs that might survive with a broad central rapidity acceptance such as in Fig. 6.7. Very little remains of the thermal dilepton contribution in the forward region due to its narrow rapidity distribution.

6.5. CONCLUSIONS

In summary, we calculate open charm and bottom production and determine their contributions to the dilepton continuum in Pb+Pb collisions at $\sqrt{s_{NN}} = 2.76$ TeV with and without including heavy quark energy loss. These rates are then compared with Drell-Yan and thermal dilepton production. The contributions of all these sources are obtained in kinematic regions relevant for the LHC detectors.

Since most detectors accept only high p_T single leptons, thermal dileptons would be difficult to measure. Heavy flavours are the dominant source of dileptons in most kinematic regimes, even after energy loss. At forward rapidity, the Drell-Yan contribution begins to dominate for $M > 10 \text{ GeV}/c^2$. The effects of energy loss on the decay dileptons alters their acceptance, particularly for high lepton p_T cuts. In most of the kinematic regions considered, the $b\bar{b}$ decay contributions become larger than those of $c\bar{c}$ for lepton pair masses greater than $7 \text{ GeV}/c^2$.

From the approximately 50 M events collected by CMS in the first year of Pb+Pb collisions, we conclude that there will be few continuum contributions above $40 \text{ GeV}/c^2$, evident from the high mass dimuon distribution published by the CMS [117], in agreement with the result shown in Fig. 6.7(d). The second Pb+Pb run in 2011 has 20 times more events which will help quantify the heavy flavour contribution after uncorrelated pairs are eliminated by background subtraction techniques. Their yields relative to pp collisions at the same energy can be used as a high statistics probe of the medium properties in Pb+Pb collisions.

Appendix A.

appendices

A.1. Extra Studies

Padding? What do you mean?

A.2. rr

See, maths in titles automatically goes bold where it should (and check the table of contents: it *isn't* bold there!) Check the source: nothing needs to be specified to make this work. Thanks to Donald Arsenau for the teeny hack that makes this work.

Bibliography

- [1] T. Matsui and H. Satz, Phys. Lett. B 178, **416** (1986).
- [2] NA50, M. C. Abreu et al., Phys. Lett. B 477, **28** (2000).
- [3] Z. Lin and C. Ko, Physics Letters B 503, **104** (2001).
- [4] Robert Oerter. The Theory Of Almost Everything: The Standard Model, The Unsung Triumph Of Modern Physics. Plume, 2006.
- [5] D. J. Gross and F. Wilczek. “Asymptotically Free Gauge Theories. 1” Phys. Rev. D 8, **3633**, (1973).
- [6] H. D. Politzer. “Reliable Perturbative Results for Strong Interactions” Phys. Rev. Lett. 30, **1346**, (1973).
- [7] D. J. Gross and F. Wilczek. “Ultraviolet Behavior of Non-Abelian Gauge Theories” Phys. Rev. Lett. 30, **1343**, (1973).
- [8] H. D. Politzer. “Asymptotic Freedom: An Approach to Strong Interactions” Phys. Rept. 14, **129**, (1974).
- [9] R. P. Feynman. “Quantum Electrodynamics”. W. A. Benjamin, Inc., New York, (1961).
- [10] S. S. Schweber. “QED and the men who made it: Dyson, Feynman, Schwinger, and Tomonaga”. Princeton University Press, Princeton, N.J., (1994).
- [11] Ruth Povh, Scholz and Zetsche. “Particles and Nuclei: An Introduction to the Physical Concepts”. Springer, (1993).
- [12] R. Hagedorn, Nuovo Cim. Suppl., 3, **147** (1965).
- [13] C. Wong, Introduction to High-Energy Heavy-Ion Collisions (World Scientific, Singapore, 1994).

- [14] R. Vogt, Ultrarelativistic Heavy Ion Collisions (Elsevier, 2007).
- [15] F. Karsch, Lect. Notes Phys., 583, **209** (2002), arXiv:hep-lat/0106019.
- [16] J. L. Nagle, Eur. Phys. J. C, 49, **275** (2007), arXiv:nucl-th/0608070.
- [17] B. Muller and J. L. Nagle, Annu. Rev. Nucl. Part. Sci., 56, **93** (2006), arXiv:nucl-th/0602029.
- [18] K. Adcox et al., Nucl. Phys. A, 757, **184** (2005), arXiv:nucl-ex/0410003.
- [19] J. E. Augustin et al. Phys. Rev. Lett. 33 **1406**, (1974).
- [20] B. Aubert et al. Phys. Rev. Lett. 98 **211802**, (2007), arXiv:hep-ex/0207042.
- [21] S. L. Glashow, J. Iliopoulos and L. Maiani, Phys. Rev. D 2 **1285**, (1970).
- [22] Yao et al. J. Phys. G, **33**, (2006).
- [23] S. W. Herb et al., Phys. Rev. Lett. 39 **252**, (1977).
- [24] F. Abe et al., Phys. Rev. Lett. 79 **572**, (1997).
- [25] J. Baines eta al., Heavy quarks (Working Group 3): Summary report,arXiv:hep-ph/0601164.
- [26] R. Vogt, J. Phys.G 31 **S773**, (2005), arXiv:hep-ph/0412303.
- [27] R. Vogt, Int. J. Mod. Phys. E 12 **211**, (2003), arXiv:hep-ph/0111271.
- [28] E. L. Berger and D. L. Jones, Phys. Rev. D23 **1521**, (1981).
- [29] M. Cacciari and M. Kramer, Phys. Rev. Lett. 76 **4128**, (1996), arXiv:hep-ph/9601276.
- [30] E. Braaten and S. Fleming, Phys. Rev. Lett. 74 **3327**, (1995), arXiv: hep-ph/9411365.
- [31] P. L. Cho and A. K. Leibovich, Phys. Rev. D 53 **150**, (1996), arXiv:hep-ph/9505329.
- [32] P. L. Cho and A. K. Leibovich, Phys. Rev. D 53 **6203**, (1996), arXiv:hep-ph/9511315.
- [33] H. Fritzsch, Phys. Lett. B 67 **217**, (1977).
- [34] J. F. Amundson, O. J. P. Eboli, E. M. Gregores and F. Halzen, Phys. Lett. B 372

- 127**, (1996), arXiv:hep-ph/9512248.
- [35] J. F. Amundson, O. J. P. Eboli, E. M. Gregores and F. Halzen, Phys. Lett. B 390 **323**, (1997), arXiv:hep-ph/9605292.
- [36] F. Abe et al, Phys. Rev. Lett. 79 **572**, (1997).
- [37] F. Abe et al, Phys. Rev. Lett. 79 **578**, (1997).
- [38] D. Acosta et al. Phys. Rev. Lett. 88 **161802**, (2002).
- [39] A. A. Affolder Phys. Rev. Lett. 85 **2886**, (2000), arXiv:hep-ex/0004027.
- [40] R. L. Thews. arXiv: hep-ph/9409209.
- [41] D. Kharzeev and R. L. Thews. Phys. Rev. C, 60(4) **041901**, 1999.
- [42] Helmut Satz. J. Phys. G32 **R25**, (2006). arXiv: hep-ph/0512217.
- [43] Frithjof Karsch. Eur. Phys. J., C43 **3543**, 2005. arXiv: hep-lat/0502014.
- [44] Matthias Doring, Kay Hubner, Olaf Kaczmarek, and Frithjof Karsch Phys. Rev., D75 **054504**, 2007. arXiv: hep-lat/0702009.
- [45] A. Jakovac, P. Petreczky, K. Petrov, and A. Velytsky. Phys. Rev. D75 **014506**, 2007. arXiv: hep-lat/0611017.
- [46] C. Baglin et al. Phys. Rev. Lett. 33 **1406**,(1974).
- [47] C. Baglin et al., Phys. Lett. B 255 **459**(1976).
- [48] B. Alessandro et al., Eur. Phys. J. C 39 **335**, (2005),arXiv:nucl-ex/0612013.
- [49] M. C. Abreu et al., Phys. Lett. B 530 **43**, (2002).
- [50] D. Kharzeev, C. Lourenco, M. Nardi and H. Satz, Z. Phys. C 74 **307**,(1997), arXiv:hep-ph/9612217.
- [51] E. Scomparin, arXiv:nuclex/0703030.
- [52] S. S. Adler et al., Phys. Rev. Lett. 96 **012304**, (2006),arXiv:nucl-ex/0507032.
- [53] P. Pillot et al. AIP Conf. Proc., 806 **279285**, (2006).
- [54] T. Gunji, J. Phys. G 34 **S749**, (2007), arXiv:nucl-ex/0703004.
- [55] M. Strickland, D. Bazow Nucl.Phys. A **879** (2012), arXiv:nucl-ph/1112.2761.

- [56] A. Kesich J.Phys.Conf.Ser. **389** (2012) 012025, arXiv::nucl-ex/1207.7166.
- [57] R. Reed J. Phys. G **38**, 124185 (2011), arXiv::nucl-ex/1109.3891.
- [58] H. Schopper and R.D. Heuer. LEP - The Lord of the Collider Rings at CERN 1980-2000: The Making, Operation and Legacy of the World's Largest Scientific Instrument. Springer, 2009.
- [59] The CMS magnet project: Technical Design Report. Technical Design Report CMS. CERN, Geneva, 1997.
- [60] The CMS experiment at the CERN LHC. JINST, page 0803:S08004, 2008.
- [61] The CMS Collaboration. CMS TriDAS project: Technical Design Report; 1, the trigger systems. Technical Design Report CMS.
- [62] Sergio Cittolin, Attila Rcz, and Paris Sphicas. CMS trigger and data-acquisition project: Technical Design Report. Technical Design Report CMS. CERN, Geneva, 2002.
- [63] G.L. Bayatyan et al, CERN-LHCC-2005-023, CMS-TDR-007 (2005).
- [64] F. Karsch and E. Laermann, “Thermodynamics and in-medium hadron properties from lattice QCD”, in Quark-Gluon Plasma III, R. C. Hwa and X.-N. Wang, eds. World Scientific Publishing Co. Pte. Ltd., 2004. arXiv:hep-lat/0305025.
- [65] E. V. Shuryak, “Theory of Hadronic Plasma”, Sov. Phys. JETP **47** (1978) 212.
- [66] BRAHMS Collaboration, “Quark-gluon plasma and color glass condensate at RHIC? The perspective from the BRAHMS experiment”, Nucl. Phys. A **757** (2005) 1,doi:10.1016/j.nuclphysa.2005.02.130, arXiv:nucl-ex/0410020
- [67] PHOBOS Collaboration, “The PHOBOS perspective on discoveries at RHIC”, Nucl. Phys. A **757** (2005) 28, doi:10.1016/j.nuclphysa.2005.03.084,arXiv:nucl-ex/0410022.
- [68] PHENIX Collaboration, “Formation of dense partonic matter in relativistic nucleus-nucleus collisions at RHIC: Experimental evaluation by the PHENIX Collaboration”, Nucl. Phys. A **757** (2005) 184,doi:10.1016/j.nuclphysa.2005.03.086, arXiv:nucl-ex/0410003.
- [69] STAR Collaboration, “Experimental and theoretical challenges in the search for the quark-gluon plasma: The STAR Collaboration’s critical assessment of the evidence from RHIC collisions”, Nucl. Phys. A **757** (2005)

- 102,doi:10.1016/j.nuclphysa.2005.03.085, arXiv:nucl-ex/0501009.
- [70] A. and P. Petreczky, “Color screening melts quarkonium”, Phys. Rev. Lett. **99** (2007) 211602, doi:10.1103/PhysRevLett.99.211602, arXiv:0706.2183.
- [71] R. Vogt, “Cold Nuclear Matter Effects on J/ψ and Υ Production at energies available at the CERN Large Hadron Collider (LHC)”, Phys. Rev. C **81** (2010) 044903, doi:10.1103/PhysRevC.81.044903, arXiv:1003.3497.
- [72] X. Zhao and R. Rapp, “Medium modifications and production of charmonia at LHC”, Nucl. Phys. A **859** (2011) 114, doi:10.1016/j.nuclphysa.2011.05.001, arXiv:1102.2194.
- [73] X. Zhao and R. Rapp, “Charmonium in medium: From correlators to experiment”, Phys. Rev. C **82** (2010) 064905, doi:10.1103/PhysRevC.82.064905, arXiv:1008.5328.
- [74] A. Andronic et al., “Statistical hadronization of heavy quarks in ultra-relativistic nucleus-nucleus collisions”, Nucl. Phys. A **789** (2007) 334,doi:10.1016/j.nuclphysa.2007.02.013, arXiv:nucl-th/0611023.
- [75] A. Capella et al., “Charmonium dissociation and recombination at RHIC and LHC”, Eur. Phys. J. C **58** (2008) 437, doi:10.1140/epjc/s10052-008-0772-6,arXiv:0712.4331.
- [76] R. L. Thews and M. L. Mangano, “Momentum spectra of charmonium produced in a quark-gluon plasma”, Phys. Rev. C **73** (2006) 014904,doi:10.1103/PhysRevC.73.014904, arXiv:nucl-th/0505055.
- [77] L. Yan, P. Zhuang, and N. Xu, “ J/ψ production in quark-gluon plasma”, Phys. Rev. Lett. **97** (2006) 232301, doi:10.1103/PhysRevLett.97.232301, arXiv:nucl-th/0608010.
- [78] L. Grandchamp et al., “Bottomonium production at $\sqrt{s_{NN}} = 200$ GeV and $\sqrt{s_{NN}} = 5.5$ TeV”,Phys. Rev. C **73** (2006) 064906, doi:10.1103/PhysRevC.73.064906, arXiv:hep-ph/0507314.
- [79] NA38 Collaboration, “ ψ' and J/ψ production in pW, pU and SU interactions at 200 GeV/nucleon”, Phys. Lett. B **345** (1995) 617, doi:10.1016/0370-2693(94)01614-I.
- [80] NA50 Collaboration, “A new measurement of J/ψ suppression in PbPb collisions at 158 GeV per nucleon”, Eur. Phys. J. C **39** (2005) 335,doi:10.1140/epjc/s2004-02107-9, arXiv:hep-ex/0412036.

- [81] NA50 Collaboration, “ ψ' production in PbPb collisions at 158 GeV/nucleon”, Eur. Phys. J. C **49** (2007) 559, doi:10.1140/epjc/s10052-006-0153-y, arXiv:nucl-ex/0612013.
- [82] NA60 Collaboration, “ J/ψ production in InIn collisions at 158 GeV/nucleon”, Phys. Rev. Lett. **99** (2007) 132302, doi:10.1103/PhysRevLett.99.132302.
- [83] PHENIX Collaboration, “ J/ψ production versus centrality, transverse momentum, and rapidity in AuAu collisions at $\sqrt{s_{NN}} = 200$ GeV”, Phys. Rev. Lett. **98** (2007) 232301, doi:10.1103/PhysRevLett.98.232301, arXiv:nucl-ex/0611020.
- [84] STAR Collaboration, “ Υ cross section in pp collisions at $\sqrt{s_{NN}} = 200$ GeV”, Phys. Rev. D **82** (2010) 012004, doi:10.1103/PhysRevD.82.012004, arXiv:1001.2745.
- [85] CMS Collaboration, “The CMS experiment at the CERN LHC”, JINST **3** (2008) S08004, doi:10.1088/1748-0221/3/08/S08004.
- [86] CMS Collaboration, “Observation and studies of jet quenching in PbPb collisions at $\sqrt{s_{NN}} = 2.76$ TeV”, Phys. Rev. C **84** (2011) 024906, doi:10.1103/PhysRevC.84.024906, arXiv:1102.1957.
- [87] CMS Collaboration, “Dependence on pseudorapidity and centrality of charged hadron production in PbPb collisions at $\sqrt{s_{NN}} = 2.76$ TeV”, JHEP **08** (2011) 141, doi:10.1007/JHEP08(2011)141, arXiv:1107.4800.
- [88] M. L. Miller et al., “Glauber modeling in high-energy nuclear collisions”, Ann. Rev. Nucl. Part. Sci. **57** (2007) 205, doi:10.1146/annurev.nucl.57.090506.123020, arXiv:nucl-ex/0701025.
- [89] T. Sjostrand, S. Mrenna, and P. Z. Skands, “PYTHIA 6.4 physics and manual”, JHEP **05** (2006) 026, doi:10.1088/1126-6708/2006/05/026, arXiv:hep-ph/0603175.
- [90] M. Bargiotti and V. Vagnoni, “Heavy quarkonia sector in PYTHIA 6.324: Tuning, validation and perspectives at LHCb”, LHCb Note LHCb-2007-042, (2007).
- [91] CDF Collaboration, “Measurement of the J/ψ meson and b-hadron production cross sections in pp collisions at $\sqrt{s_{NN}} = 1960$ GeV”, Phys. Rev. D **71** (2005) 032001, doi:10.1103/PhysRevD.71.032001, arXiv:hep-ex/0412071.
- [92] D. J. Lange, “The EvtGen particle decay simulation package”, Nucl. Instrum. Meth. A **462** (2001) 152, doi:10.1016/S0168-9002(01)00089-4.

- [93] E. Barberio and Z. Was, “PHOTOS - A universal Monte Carlo for QED radiative corrections: version 2.0”, *Comput. Phys. Commun.* **79** (1994) 291, doi:10.1016/0010-4655(94)90074-4.
- [94] GEANT Collaboration, “GEANT4 - A simulation toolkit”, *Nucl. Instrum. Meth. A* **506** (2003) 250, doi:10.1016/S0168-9002(03)01368-8.
- [95] I. P. Lokhtin and A. M. Snigirev, “A model of jet quenching in ultrarelativistic heavy ion collisions and high- p_T hadron spectra at RHIC”, *Eur. Phys. J. C* **45** (2006) 211, doi:10.1140/epjc/s2005-02426-3, arXiv:hep-ph/0506189.
- [96] CMS Collaboration, “CMS physics technical design report: Addendum on high density QCD with heavy ions”, *J. Phys. G* **34** (2007) 2307, doi:10.1088/0954-3899/34/11/008.
- [97] C. Roland (on behalf of the CMS Collaboration), “Track reconstruction in heavy ion collisions with the CMS silicon tracker”, *Nucl. Instrum. Meth. A* **566** (2006) 123, doi:10.1016/j.nima.2006.05.023.
- [98] Particle Data Group Collaboration, “Review of particle physics”, *J. Phys. G* **37** (2010) 075021, doi:10.1088/0954-3899/37/7A/075021.
- [99] CMS Collaboration, “Indications of suppression of excited Υ states in PbPb collisions at $\sqrt{s_{NN}} = 2.76$ TeV”, *Phys. Rev. Lett.* **107** (2011) 052302, doi:10.1103/PhysRevLett.107.052302, arXiv:1105.4894.
- [100] CMS Collaboration, “Prompt and non-prompt J/ψ production in pp collisions at $\sqrt{s_{NN}} = 7$ TeV”, *Eur. Phys. J. C* **71** (2011) 1575, doi:10.1140/epjc/s10052-011-1575-8, arXiv:1011.4193.
- [101] P. Faccioli and J. Seixas, “Observation of χ_c and χ_b nuclear suppression via dilepton polarization measurements”, arXiv:1203.2033.
- [102] CDF Collaboration, “Production of $\Upsilon(1S)$ mesons from χ_b decays in $p\bar{p}$ collisions at $\sqrt{s} = 1.8$ TeV”, *Phys. Rev. Lett.* **84** (2000) 2094, doi:10.1103/PhysRevLett.84.2094, arXiv:hep-ex/9910025.
- [103] CMS Collaboration, “Upsilon production cross section in pp collisions at $s = 7$ TeV”, (2011). arXiv:1012.5545. published in *Phys. Rev. D*.
- [104] C. Lourenco, R. Vogt, and H. K. Woehri, “Energy dependence of J/ψ absorption in proton-nucleus collisions”, *JHEP* 02 **014** (2009), arXiv:0901.3054. doi:10.1088/1126-

6708/2009/02/014.

- [105] D. M. Alde et al., “Nuclear dependence of the production of Upsilon resonances at 800-GeV”, Phys. Rev. Lett. **66** (1991) 2285. doi:10.1103/PhysRevLett.66.2285.
- [106] N. Brambilla et al., “Heavy quarkonium: progress, puzzles, and opportunities”, Eur. Phys. J. C **71** (2011) 1534, doi:10.1140/epjc/s10052-010-1534-9, arXiv:1010.5827.
- [107] CMS Collaboration, “Indications of suppression of excited Υ states in PbPb collisions at $\sqrt{s_{NN}} = 2.76$ TeV”, Phys.Rev.Lett. **107** (2011) 052302, doi:10.1103/PhysRevLett.107.052302, arXiv:1105.4894.
- [108] CMS Collaboration, “Bottomonium production measured in PbPb and pp collisions by CMS”, J.Phys.G:Nucl.Part.Phys. **38** (2011) 124071, doi:10.1088/0954-3899/38/12/124071.
- [109] Brianti, G. Phys. Rept. **403-404** (2004)
- [110] I. Arsene *et al.* (BRAHMS Collaboration), Nucl. Phys. A **757**, 1 (2005); B. B. Back *et al.* (PHOBOS Collaboration), Nucl. Phys. A **757**, 28 (2005); J. Adams *et al.* (STAR Collaboration), Nucl. Phys. A **757**, 10 (2005); K. Adcox *et al.* (PHENIX Collaboration), Nucl. Phys. A **757**, 184 (2005).
- [111] N. Armesto *et al.*, J. Phys. G **35**, 054001 (2008).
- [112] S. Gavin, P. L. McGaughey, P. V. Ruuskanen, and R. Vogt, Phys. Rev. C **54**, 2606 (1996).
- [113] Z. Lin, R. Vogt and X. N. Wang, Phys. Rev. C **57**, 899 (1998).
- [114] Z. Lin and R. Vogt, Nucl. Phys. B **544**, 339 (1999).
- [115] E. Shuryak, Phys. Rev. C **55**, 961 (1997).
- [116] U. Jamil and D. K. Srivastava, J. Phys. G **37**, 085106 (2010).
- [117] S. Chatrchyan *et al.* (CMS Collaboration), Phys. Rev. Lett. **106**, 212301 (2011)
- [118] S. Chatrchyan *et al.* CMS collaboration, arXiv:1201.5069v1 [nucl-ex]; CMS-HIN-10-006.
- [119] G. Aad *et al.* (ATLAS Collaboration), arXiv:1012.5419 [hep-ex] (2010).
- [120] A. Adare *et al.* (PHENIX Collaboration), Phys. Rev. C **84**, 044905 (2011).

- [121] A. Dainese *et al.* (ALICE Collaboration), J. Phys. G **38**, 124032 (2011).
- [122] K. Gallmeister, B. Kampfer, and O. P. Pavlenko, Phys. Rev. C **57**, 3276 (1998).
- [123] D. Fein, Z. Huang, P. Valerio and I. Sarcevic, Phys. Rev. C **56**, 1637 (1997).
- [124] M. G. Mustafa, D. Pal and D. K. Srivastava, Phys. Rev. C **57**, 889 (1998).
- [125] H. Agakishiev *et al.* (STAR Collaboration), Phys. Rev. D **83**, 052006 (2011) [arXiv:1102.2611 [nucl-ex]]; A. Adare *et al.* (PHENIX Collaboration), Phys. Rev. Lett. **97**, 252002 (2006) [hep-ex/0609010].
- [126] J. Pumplin, D. R. Stump, J. Huston, H. L. Lai, P. M. Nadolsky and W. K. Tung, JHEP **0207**, 012 (2002) [arXiv:hep-ph/0201195]; D. Stump, J. Huston, J. Pumplin, W. K. Tung, H. L. Lai, S. Kuhlmann and J. F. Owens, JHEP **0310**, 046 (2003) [arXiv:hep-ph/0303013].
- [127] K. J. Eskola, H. Paukkunen and C. A. Salgado, JHEP **0904**, 065 (2009) [arXiv:0902.4154 [hep-ph]].
- [128] M. Cacciari, P. Nason and R. Vogt, Phys. Rev. Lett. **95**, 122001 (2005).
- [129] M. L. Mangano, P. Nason, and G. Ridolfi, Nucl. Phys. B **373**, 295 (1992).
- [130] R. Nelson, R. Vogt and A. D. Frawley, submitted to Phys. Rev. C; R. Vogt, R. E. Nelson and A. D. Frawley, arXiv:1207.6812 [hep-ph].
- [131] R. Vogt, Eur. Phys. J. Special Topics **155**, 213 (2008).
- [132] R. Vogt, Eur. Phys. J. C **61**, 793 (2009).
- [133] S. Chatrchyan *et. al.* (CMS Collaboration), Phys. Rev. C **84**, 024906 (2011).
- [134] P. Lévai and R. Vogt, Phys. Rev. C **56**, 2707 (1997).
- [135] R. Hamberg, W.L. van Neerven and T. Matsuura, Nucl. Phys. **B359**, 343 (1991).
- [136] A. Accardi *et al.*, arXiv:hep-ph/0308248.
- [137] T. Sjöstrand, S. Mrenna and P. Skands, JHEP **05**, 026 (2006) [arXiv:hep-ph/0603175].
- [138] A. D. Frawley, T. Ullrich and R. Vogt, Phys. Rept. **462**, 125 (2008) [arXiv:0806.1013 [nucl-ex]].

- [139] T. Sakaguchi *et al.* (PHENIX Collaboration), in proceedings of Quark Matter 2012.
- [140] C. Mironov *et al.* (CMS Collaboration), in proceedings of Quark Matter 2012.
- [141] J. D. Bjorken, Phys. Rev. D **27**, 140 (1983).
- [142] K. Kajantie, M. Kataja, L. McLerran, and P. V. Ruuskanen, Phys. Rev. D **34**, 811 (1986).
- [143] R. Vogt, B. V. Jacak, P. L. McGaughey, P. V. Ruuskanen, Phys. Rev. D **49**, 3345 (1994).
- [144] C. Gale and P. Lichard, Phys. Rev. D **49**, 3338 (1994);
C. Song, C.M. Ko, and C. Gale, *ibid* **50** R 1827 (1994).
- [145] S. Chatrchyan *et al.* (CMS Collaboration), arXiv:1107.4800 [nucl-ex] (2011).
- [146] S. Chatrchyan *et al.* (CMS Collaboration), JINST **3**, S08004 (2008).
- [147] ATLAS Collaboration, JINST **3**, S08003 (2008).
- [148] ALICE Collaboration, Technical Proposal, CERN/LHCC/95-71; The ALICE Collaboration, JINST **3**, S08002 (2008).
- [149] Andy Buckley The heptesis L^AT_EX class

List of Figures

1.1.	Standard Model leptons and bosons	4
1.3.	QCD Phase diagram	7
1.4.	QCD Phase diagram	8
1.5.	HeavyIon Collisions	11
2.1.	J/ψ family	14
2.2.	Υ family	14
2.3.	J/ψ and Υ cross sections	16
2.4.	QuarkoniaAtTc	19
2.5.	JPsiAtSPSCrossSection	22
2.6.	JPsiNA38	23
2.7.	JPsiNA50	24
2.8.	PsiNA50NA60	24
2.9.	JPsiRHICPhenix	25
2.10.	JPsiRHICPhenix2	26
3.1.	CERN accelerator complex	30
3.2.	LHC ring	31
3.3.	CMS Detector figure	34
3.4.	CMS Detector Slice figure	35

3.5. CMS Magnet artistic view	37
3.6. CMS Tracker 3D drawing	37
3.7. CMS ECAL	39
3.8. CMS HCAL	40
3.9. CMS Muon system	40
4.1. Centrality distribution of the minimum-bias sample (solid black line) overlaid with the double-muon triggered sample (hashed red) in bins of 2.5%	47
4.2. Reconstruction efficiency of global muons in the (η^μ, p_T^μ) space, illustrating the lower limits (white lines) of what is considered a detectable single muon for the analysis.	49
4.3. Invariant-mass spectrum of $\mu^+\mu^-$ pairs (black circles) with $p_T < 20\text{GeV}/c$ and $ y < 2.4$, for muons above $4\text{GeV}/c$, integrated over centrality (left) and for the 0–10% centrality bin (right).	51
4.4. Dimuon acceptance as a function of p_T (left) and $ y $ (right) for J/ψ (red squares) and $\Upsilon(1S)$ (green diamonds). Also shown in the right panel is the acceptance for J/ψ with $p_T > 6.5\text{GeV}/c$ (open black squares). The error bars represent the statistical uncertainties only.	53
4.5. Combined trigger, reconstruction, and selection efficiencies as a function of quarkonium p_T and $ y $, and event centrality, for each signal: red squares and orange stars for prompt and non-prompt J/ψ , respectively, and green diamonds for $\Upsilon(1S)$. For better visibility, the prompt J/ψ points are shifted by $\Delta p_T = 0.5\text{GeV}/c$, $\Delta y = 0.05$, and $\Delta N_{\text{part}} = 2$. Statistical (systematic) uncertainties are shown as bars (boxes). The systematic uncertainties are the quadratic sum of the uncertainty on the kinematic distributions and the MC validation uncertainty.	55
4.6. The pp dimuon invariant-mass distribution in the range $p_T < 20\text{GeV}/c$ for $ y < 2.4$ and the result of the fit to the Υ resonances.	56

4.7. Left: $\Upsilon(1S)$ yield divided by T_{AA} in PbPb collisions (green diamonds) as a function of p_T . The result is compared to the cross section measured in pp collisions (black crosses). The global scale uncertainties on the PbPb data due to T_{AA} (5.7%) and the pp integrated luminosity (6.0%) are not shown. Right: nuclear modification factor R_{AA} of $\Upsilon(1S)$ as a function of p_T . A global uncertainty of 8.3%, from T_{AA} and the integrated luminosity of the pp data sample, is shown as a grey box at $R_{AA} = 1$. Points are plotted at their measured average p_T . Statistical (systematic) uncertainties are shown as bars (boxes). Horizontal bars indicate the bin width.	60
4.8. Left: $\Upsilon(1S)$ yield divided by T_{AA} in PbPb collisions (green diamonds) as a function of rapidity. The result is compared to the cross section measured in pp collisions (black crosses). The global scale uncertainties on the PbPb data due to T_{AA} (5.7%) and the pp integrated luminosity (6.0%) are not shown. Right: nuclear modification factor R_{AA} of $\Upsilon(1S)$ as a function of rapidity. A global uncertainty of 8.3%, from T_{AA} and the integrated luminosity of the pp data sample, is shown as a grey box at $R_{AA} = 1$. Points are plotted at their measured average $ y $. Statistical (systematic) uncertainties are shown as bars (boxes). Horizontal bars indicate the bin width.	61
4.9. Left: $\Upsilon(1S)$ yield divided by T_{AA} (green diamonds) as a function of N_{part} compared to the $\Upsilon(1S)$ cross section measured in pp (black cross). Right: nuclear modification factor R_{AA} of $\Upsilon(1S)$ as a function of N_{part} . A global uncertainty of 6%, from the integrated luminosity of the pp data sample, is shown as a grey box at $R_{AA} = 1$. Statistical (systematic) uncertainties are shown as bars (boxes).	61
4.10. Dimuon invariant-mass distributions from the $p\ p$ (a) and PbPb (b) data at $\sqrt{s_{\text{NN}}} = 2.76$ TeV. The same reconstruction algorithm and analysis criteria are applied to both data sets, including a transverse momentum requirement on single muons of $p_T^\mu > 4$ GeV/ c . The solid lines show the result of the fit described in the text.	65
5.1. Number of muon inner track valid cut study (default: > 10).	74
5.2. Number of muon pixel layers cut study (default: > 0).	75
5.3. Number of muon inner track χ^2/ndf cut study (default: < 4).	75

5.4. Number of muon global track χ^2/ndf cut study (default: < 20)	75
5.5. Number of valid muon hits cut study (default: ≥ 0)	76
5.6. D_{xy} cut study (default: < 3)	76
5.7. D_z cut study (default: < 15)	76
5.8. Dimuon vertex probability cut study (default: $> 5\%$)	77
5.9. Significance of $\Upsilon(1S)$ peak as a function of the single muon p_T cut	78
5.10. Same-sign muon pairs invariant mass distribution with different muon p_T cuts, shown in the vicinity of the $\Upsilon(nS)$ mass region.	79
5.11. Uncertainty on the $2B/(S + B)$ quantity as a function of the single muon p_T cut.	80
5.12. $\Upsilon(1S)$ p_T distributions	82
 6.1. (Color online) Theoretical uncertainty bands on inclusive single charm and bottom quark production cross sections per nucleon as functions of p_T (left) and rapidity (right) for $\sqrt{s_{NN}} = 2.76$ TeV. The uncertainties are calculated by varying the quark mass, renormalization scale μ_R and factorization scale μ_F . The calculations include modification of the initial parton distributions with the EPS09 central parameter set. No final state energy loss is included.	87
6.2. (Color online) Theoretical uncertainty bands on inclusive single charm and bottom quark production cross sections per nucleon as functions of p_T (left) and rapidity (right) for $\sqrt{s_{NN}} = 2.76$ TeV. The uncertainties are calculated by varying the quark mass, renormalization scale μ_R and factorization scale μ_F . The calculations include modification of the initial parton distributions with the EPS09 central parameter set. Here we include final state energy loss assuming that the charm and bottom quark R_{AA} is the same, as discussed in the text.	88

6.3. (Color online) The inclusive single charm and bottom quark per nucleon cross sections as a function of p_T (left) and rapidity (right) both with and without energy loss in Pb+Pb collisions at $\sqrt{s_{NN}} = 2.76$ TeV. The cross sections, given per nucleon, include modification of the initial parton distributions via the central EPS09 shadowing parameterization.	90
6.4. The thermal dilepton cross section as a function of p_T (left) and rapidity (right) in Pb+Pb collisions at $\sqrt{s_{NN}} = 2.76$ TeV.	92
6.5. (Color online) Theoretical uncertainty bands for the dilepton invariant mass distributions from semileptonic charm (red, short-dashed) and bottom (blue, dot-dot-dashed) decays. The uncertainties are calculated the same way as in Sect. 6.2.	94
6.6. (Color online) The invariant mass distributions for the four contributions to the dilepton spectra discussed here: semileptonic charm (red, short-dashed) and bottom (blue, dot-dot-dashed) decays, Drell-Yan (magenta, long-dashed) and thermal (black, dotted) dileptons along with the sum (black, solid) in Pb+Pb collisions per nucleon pair at $\sqrt{s_{NN}} = 2.76$ TeV. Left pannel shows distributions without any final state energy loss, right pannel is after including heavy quark energy loss in the medium. The per nucleon cross sections are given. No phase space or kinematic cuts are introduced.	95
6.7. (Color online) The same as Fig. 6.6 but now with single muon rapidity cuts of $ \eta^\mu \leq 2.4$. A minimum single lepton transverse momentum cut of $p_T^\mu \geq 0$ (a), 1 (b), 4 (c) and 10 (d) GeV/ c is also shown.	96
6.8. (Color online) The same as Fig. 6.6 but now with single muon rapidity cuts of $ \eta^\mu \leq 0.8$. A minimum single lepton transverse momentum cut of $p_T^\mu \geq 0$ (a) and 3 (b) GeV/ c is also shown.	97
6.9. (Color online) The same as Fig. 6.6 but now with single muon rapidity cuts of $2.4 \leq \eta^\mu \leq 4$. A minimum single lepton transverse momentum cut of $p_T^\mu \geq 0$ (a) and 1 (b) GeV/ c is also shown.	97

List of Tables

2.1.	QuarkoniaProperties	20
4.1.	Average and root-mean-square (RMS) values of the number of participating nucleons (N_{part}) and of the nuclear overlap function (T_{AA}) for the centrality bins used in this analysis[86].	47
4.2.	Point-to-point systematic uncertainties on the prompt J/ψ , non-prompt J/ψ , and $\Upsilon(1S)$ yields measured in PbPb collisions.	58
4.3.	Point-to-point systematic uncertainties on the prompt J/ψ , non-prompt J/ψ , and $\Upsilon(1S)$ yields measured in pp collisions.	59
5.1.	Estimated $\Upsilon(1S)$ yield significance, signal efficiency (MC) and background rejection in % after applying all other cuts but the one listed.	82